Available online at www.sciencedirect.com
SCIENCE DIRECT®
Physics Reports 384 (2003) 1–84
PHYSICS REPORTS
www.elsevier.com/locate/physrep

The p-process of stellar nucleosynthesis: astrophysics and nuclear physics status

M. Arnould*, S. Goriely

Campus de la Plaine, Institut d'Astronomie et d'Astrophysique, Universite Libre de Bruxelles, CP226, 1050 Brussels, Belgium

Accepted 4 June 2003
editor: M.P. Kamionkowski

Abstract

The p-process of stellar nucleosynthesis is aimed at explaining the production of the stable neutron-deficient nuclides heavier than iron that are observed up to now in the solar system exclusively. Various scenarios have been proposed to account for the bulk p-nuclide content of the solar system, as well as for deviations ('anomalies') with respect to the bulk p-isotope composition of some elements discovered in primitive meteorites. The astrophysics of these models is reviewed, and the involved nuclear physics is discussed, including a brief account of recent experimental efforts. Already published results are complemented with new ones. A specific attention is paid to the very rare odd–odd nuclides ^{138}La and ^{180}Ta^{m}, as well as to the puzzling case of the light Mo and Ru isotopes. Astrophysics and nuclear physics prospects of improvements in the p-process modeling are presented.

PACS: 24.60.−k; 26.30.+k; 26.45.+h; 96.10.+i

Keywords: Solar system: composition; Stellar nucleosynthesis: p-process; Nuclear reactions; Statistical model

Contents

* Corresponding author.
E-mail address: marcel_arnould@astro.ulb.ac.be (M. Arnould).

0370-1573/03/$ - see front matter © 2003 Elsevier B.V. All rights reserved.
doi:10.1016/S0370-1573(03)00242-4

1. Introduction

The observational foundation of the theory of nucleosynthesis rests largely upon the determination of elemental and isotopic abundances in the broadest possible variety of cosmic objects, as well as upon the study of the most complete set of available observables that help characterizing the

objects. This knowledge relies almost entirely on the detailed study of the light (possibly at various wavelengths) originating from a large diversity of emitting locations: our Galaxy (non-exploding or exploding stars of various types, the interstellar medium), external galaxies, and perhaps even the early Universe. The studies of the electromagnetic radiation are complemented with the careful analysis of the minute amount of matter of the Universe accessible to humankind. This matter is comprised for its very largest part in various types of solar system solids. The rest is in the form of (extra-)galactic cosmic rays.

The myriad of observations of the aforementioned types leads in particular to a more and more complete, and at the same time increasingly complex, picture of the abundances in a variety of constituents of the Universe with different locations and ages. This concerns in particular the heavy elements we are dealing with in this review, these elements being defined here as those having charge numbers in excess of the value $Z = 26$ corresponding to iron. Despite the spectacular progress made in astronomical abundance observations, the solar system continues to provide a body of abundance data whose quantity, quality and coherence remain unmatched. This concerns especially isotopic compositions, which are the prime fingerprints of astrophysical nuclear processes. This is even more so for the heavy elements, the stable isotopes of which cannot be separated even by the most performant stellar spectroscopic techniques available today.

From the early days of the development of the theory of nucleosynthesis (e.g. [1]), the main observational foundation of which was the solar system composition, especially in the heavy element domain, it has proved operationally most rewarding to introduce three categories of heavy nuclides referred to as s-, p-, and r-nuclides. This splitting is not a mere game. It corresponds instead to the 'topology' of the chart of the nuclides, which exhibits three categories of stable heavy nuclides: those located at the bottom of the valley of nuclear stability, called the s-nuclides, and those situated on the neutron-deficient or neutron-rich side of the valley, named the p- or r-nuclides, respectively. Three different mechanisms are called for to account for the production of these three types of stable nuclides. They are naturally referred to as the s-, r-, and p-processes.

We are concerned here with a review of the p-process (the reader is referred to e.g. [2] for limited comments on the s- and r-processes, [3] for a more extended review on the r- and s-processes, and [4] for a more specialized overview of the s-process in low- and intermediate-mass stars). The first remarkable feature of this process is the scarcity of the efforts devoted to its understanding. In fact, after about 50 years of nuclear astrophysics research, the number of articles devoted to it still remains inferior to the 35 nuclides traditionally classified as p-nuclides. In view of this situation, we like to refer to the 'nuclear astrophysics p-nuts' when talking about the p-nuclides.

In the following, we will not be concerned with non-thermonuclear models of the p-process, like those invoking spallation reactions in the interstellar medium (ISM) [5,6], or photonuclear reactions triggered by non-thermalized photons [7]. These models indeed suffer from either too low efficiencies, or from constraints that limit their astrophysical plausibility. In the thermonuclear framework, the neutron-deficiency of the p-nuclides clearly forbids their production in neutron capture chains of the s- or r-types. In contrast, and as first proposed by [1], they could well be synthesized from the destruction of pre-existing s- or r-nuclides by different combinations of (p,γ) captures, (γ,n), (γ,p) or (γ,α) reactions. Some β-decays, electron captures or (n,γ) reactions can possibly complete the nuclear flow. These reactions may lead directly to the production of a p-nuclide. In most cases, however, they are synthesized through an unstable progenitor that transforms into the stable p-isobar

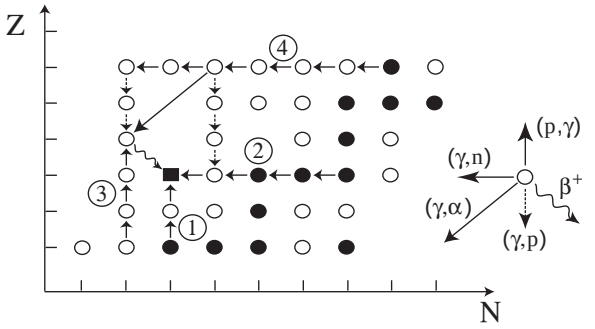

Fig. 1. Schematic representation of some simple possible nuclear routes through which seed s- or r-nuclides (black dots) can be transformed into a p-nuclide (black square). Unstable nuclei are represented by open dots. Routes (1) and (2) are made of a succession of (p,γ) and (γ,n) reactions leading directly to the p-nuclide. Slightly more complicated chains involve (p,γ) reactions followed by β-decays (Route (3)), or a combination of (γ,n) and (γ,p) or (γ,α) and β-decays (Route (4)). More complicated flow patterns involving combinations of the represented ones can also be envisioned. The p-nuclide destruction channels are not represented.

through a (chain of) β-decay(s). Fig. 1 displays in a very schematic way some possible nuclear routes through which seed s-(r-)nuclides can be transformed into p-nuclides.

The relative importance of the various ways to make p-nuclides from more neutron-rich seeds depends critically on temperature. This relates largely to the properties of the photodisintegration rates, as it will be made apparent in Section 3. In fact, values typically in excess of about 1.5×10^9 K are required for the photodisintegrations to take place on time scales commensurable with stellar evolutionary ones. It is also mandatory for these reactions to freeze-out before a too strong photoerosion of the heavy nuclides, which would leave iron peak nuclei as the main end products. In practice, this forces temperatures not to exceed about 3.5×10^9 K during a short enough time only, this limitation becoming more explicit in the following. These three constraints (abundant enough seed nuclei, high enough temperatures, short enough time scales for the hot phases) are obviously complemented by the necessity of considering proton-rich layers if (p,γ) captures are indeed envisioned.

It has been considered by [1] that the aforementioned constraints could be best satisfied in the H-rich envelopes of Type II supernova explosions, which represent the end stage of the evolution of massive stars (supernovae are in fact classified as Type II when they show H-lines in their spectra at maximum light; see [8,9] for the classification scheme of supernovae). This scenario has been put to its limits by [10]. At the end of the 1960s already, it was realized that the required high temperatures are very unlikely to be reached in the envelopes of massive star explosions. This is why [11,12] suggested to locate the p-process in the deep O–Ne-rich layers of massive stars either in their pre-supernova or supernova phases. The most actively pursued avenue of research on the p-process concerns without any doubt Type II supernova explosions. The possible role of other massive stars has also been explored. This concerns more specifically those exploding as pair-creation supernovae. It has also been proposed that the p-process could develop in the C-rich zones of Chandrasekhar-mass white dwarfs exploding as Type Ia supernovae following the accretion of some amount of matter from a companion (in contrast to Type II supernovae, Type I explosions do not show H-lines in their

spectra near maximum light; see [8,9] for more details). Alternatively, exploding sub-Chandrasekhar mass white dwarfs on which He-rich material has accumulated have also started to be explored.

This review is concerned with the latest developments of the p-process studies in the various sites mentioned above. It is structured in the following way. Section 2 presents some generalities on the observed abundances of the heavy nuclides in the solar system. The emphasis is put on the bulk solar p-nuclide abundances, as well as on isotopic anomalies (with respect to the bulk) involving p-nuclides that are identified in certain meteorites. Section 3 is devoted to a short presentation of the experimental and theoretical advances in the nuclear physics of relevance to the p-process. Sections 4–6 specialize in the synthesis of the p-nuclides by massive stars exploding as Type II supernovae. Most of the discussion focusses on one-dimensional non-rotating stars. The possible extention to two-dimensional simulations is just briefly sketched. This analysis is complemented with considerations on the p-process accompanying Type II supernovae, which are by far the most thoroughly studied p-nuclide production sites. Some comments on the main characteristics of the associated p-process nuclear flows are followed with some yield predictions as a function of stellar mass. These predictions used in conjunction with an Initial Mass Function are confronted with the solar system abundance data. The real build-up of a model for the evolution of the p-nuclide content of the Galaxy would of course require a detailed study of the dependence of the p-process yields on metallicity. A preliminary step in this direction is provided by calculations based on a model for SN1987A, the metallicity of which is about 1/3 of the solar one. The impact on the predicted p-nuclide yields of uncertainties in the $^{12}C(\alpha,\gamma)^{16}O$ rate and in the other rates involved in the p-process modeling is analyzed, as well as the abundance variations implied by a change in the total kinetic energy associated with the supernova explosion. Section 6 addresses the specific questions of the synthesis of the light Mo and Ru isotopes, the underproduction of which is endemic to all p-process calculations based on 'realistic' Type II explosion models, as well as on other scenarios. A special attention is also focussed on the interesting case of the production of the rare odd–odd nuclides ^{138}La and ^{180}Ta. Some possible solutions are sketched. Section 7 deals with an exploration of the p-nuclide synthesis in non-rotating very massive stars exploding as pair creation supernovae. The possible contribution of Type I supernovae to the p-nuclide solar system content is by far less well studied than the one of Type II explosions. Some results are presented in Section 8 for Type Ia, Ib/c and sub-Chandrasekhar white dwarf explosions. Some remarkable isotopic anomalies attributed to the p-process introduced in Section 2 are discussed in Section 9. Among the most puzzling ones is the so-called Xe-L. Two others are attributed to the decay of the radionuclides $^{92}Nb^{g}$ and ^{146}Sm. A brief summary of the most vexing problems the p-process still poses and prospects for the future are found in Section 10.

2. Observed abundances of the heavy nuclides in the solar system

2.1. The bulk solar-system composition

A milestone in the solar-system studies of astrophysical relevance was the realization that, in spite of large differences between the elemental compositions of constituent members, it was possible to derive a meaningful set of abundances likely representative for the composition with which the solar system formed some 4.6 Gy ago. Such an elemental abundance distribution is displayed in Fig. 2.

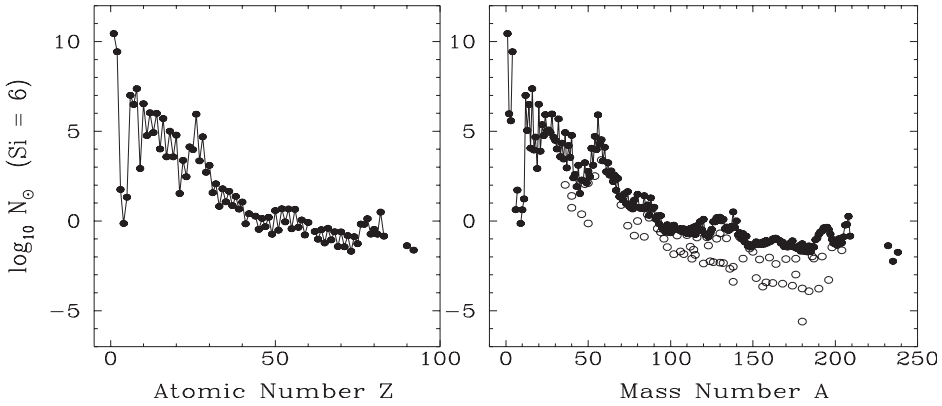

Fig. 2. Bulk elemental (left panel) and nuclear (right panel) compositions of the galactic material from which the solar system formed about 4.6 Gy ago [13]. The abundances are normalized to 10^6 Si atoms. The elemental abundances are largely based on the analysis of meteorites of the CI1 carbonaceous chondrite type. The nuclear composition is derived from those elemental abundances with the use of the terrestrial isotopic composition of the elements, except for H and the noble gases. For a given A, the most abundant isobar is shown by a dot, and less abundant ones, if any, by open circles (from [2]).

It is largely based on abundance analyses in a special class of rare meteorites, the CI1 carbonaceous chondrites, which are considered as the least-altered samples of primitive solar matter presently available [13,14]. Solar spectroscopic data, which now come in quite good agreement with the CI1 data for a large variety of elements, have to be used for the volatile elements H, He, C, N, O and Ne, whereas interpolations guided by theoretical considerations are still required in some cases (Ar, Kr, Xe, Hg).

Starting from the composition displayed in Fig. 2, it is possible to account for the differences between the *elemental* compositions of the various solar-system solid constituents in terms of a large variety of secondary physico-chemical and geological processes. In contrast these secondary processes seem to have played only a minor role as far as the isotopic composition is concerned, save some specific cases. This fact manifests itself through the extremely high homogeneity of the bulk isotopic composition of most elements within the solar system. For this, terrestrial materials have been classically adopted as the primary standard for the isotopic composition characteristic of the primitive solar nebula. However, the choice of the most representative isotopic composition of H and the noble gases raises certain specific problems.

We do not dwell here into a discussion of the details of the abundance distribution of Fig. 2. We just note for the purpose of this review that the high 'iron peak' centred around ^{56}Fe is followed by a broad peak in the $A \approx 80$–90 mass region, whereas double peaks show up at $A = 130$–138 and 195–208. These peaks are superimposed on a curve which is decreasing rapidly with increasing mass number A. It has been realized very early that these peaks provide a clear demonstration that a tight correlation exists between solar-system abundances and nuclear neutron shell closures.

As mentioned previously, it is very useful to split the heavy nuclide abundance distribution into three separate curves giving the image of the solar system content of the p-, s- and r-nuclides. This splitting is displayed in Fig. 3. In its details, the procedure of decomposition is not as obvious as it might be thought from the very definition of the different types of nuclides, and is to some extent

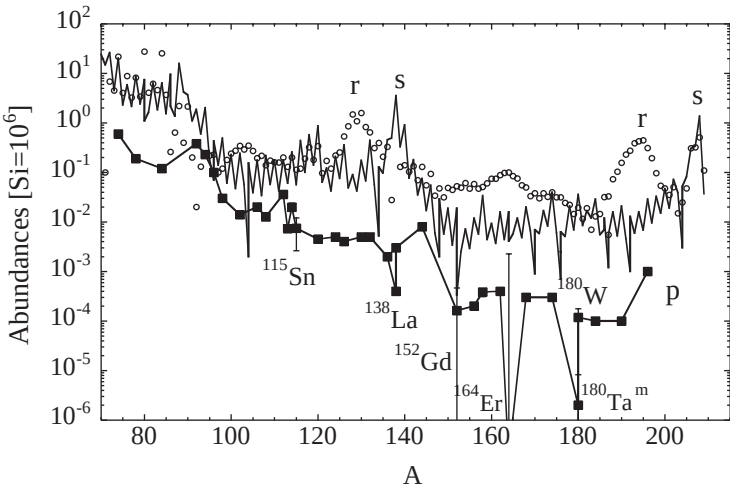

Fig. 3. Decomposition of the solar abundances of heavy nuclides into s-process (solid line), r-process (open circles) and p-process (squares) contributions. The uncertainties on the abundances of some nuclides due to a possible s-process contamination are represented by vertical bars (from [16]).

dependent on the models for the synthesis of the heavy nuclides. These models predict in particular that the stable nuclides located on the neutron-rich(deficient) side of the valley of nuclear stability are produced, to a first good approximation, by the r-(p-)process only. Fig. 4 provides a schematic view of the flows resulting from the action of the nuclear transmutations making up the r- and p-processes. They identify the most abundantly produced nuclides during these mechanisms, which are all more or less highly β-unstable. When these transmutations cease for one reason or another, the neutron-rich(deficient) nuclides involved in the flows cascade to the stable neutron-rich(deficient) nuclides. They are naturally called 'r(p-)-only' nuclides, and their abundances are deduced directly from the data displayed in Fig. 2. The situation is more intricate for the nuclides situated at the bottom of the valley of nuclear stability. Some of them are produced solely by the s-process, the typical flow of which is located very close to the bottom of nuclear stability, as illustrated in Fig. 4. They are referred to as 's-only' nuclides, and are encountered only when a stable r-isobar exists, which 'shields' the s-isobar from the r-process. As a result, only even-Z heavy elements possess a s-only isotope. A simple phenomenological model of the s-process (not reviewed here) is used to fit at best the abundances of all the s-only nuclides. Once the parameters of this model have been selected in such a way, it is used to predict the s-process contributions to the other s-nuclides. The subtraction of these s-process contributions from the observed solar abundances leaves for each isotope a residual abundance that represents the contribution to it of the r-process (if neutron-rich) or p-process (if neutron-deficient). These nuclides of mixed origins are called 'sr' or 'sp' nuclides.

Fig. 3 shows that about half of the heavy nuclei in the solar material come from the s-process, and the other half from the r-process, whereas the p-process is responsible for the production of about 0.01 to 0.001 of the abundances of the s- and r-isobars. It also appears that some elements have their abundances dominated by a s- or r-nuclide. They are naturally referred to as s- or r-elements. Clearly, p-elements do not exist. If this statement remains valid in other locations than in the solar

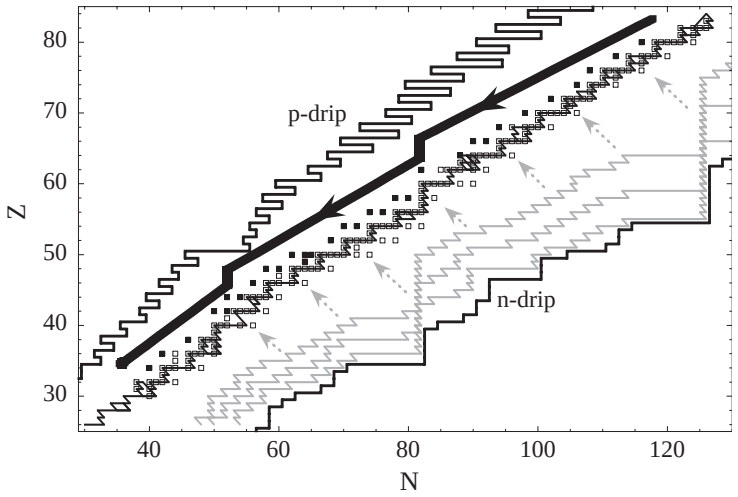

Fig. 4. Location in the (N, Z)-plane of the stable isotopes of the elements between Fe and Bi. The p-isotopes are represented by black squares, while both the s-, r-, sr- or sp-isotopes are identified with open squares (this unique representation for these four categories of nuclides is sufficient for the purpose of this review). The p-nuclides are the progeny of unstable neutron-deficient isobars located on the arrowy down-streaming p-process flow (thick black line; for more details on the p-process flow, see Section 5.1 and Fig. 30). The r-process contribution to the r-only and sr-nuclides is provided by the decay (represented by arrows) of the neutron-rich nuclides located on the up-streaming r-process flow (three such flows are represented by grayish lines). The up-streaming s-process flow (thin black line) is confined at the bottom of the valley of nuclear stability and brings the s-process contribution to the s-only and sr-nuclides. The proton and neutron drip lines correspond to the locations of zero proton and neutron separation energies (see Section 3).

system, stellar spectroscopy can provide information on the s- or r-abundances outside of the solar system, while only solar system data are available for the p-process. Even if the dominance of the s- or r-processes on a given element remains true in all astrophysical locations, a wealth of observations demonstrate departures from the solar system s- or r-element abundances. Such departures exist in the solar system itself in the form of 'isotopic anomalies' (Section 2.2), or in stars with different ages, galactic locations, or evolutionary stages. The abundance data displayed in Figs. 2 and 3 do not have any 'universal' character.

From the short description of the splitting strategy between s-, r- and p-nuclides, it is easily understandable that uncertainties affect the relative s- and r-(p-)process contributions to the solar system abundances of the sr(p)-nuclides. These uncertainties arise from various sources, including the measured abundances themselves, as well as those affecting the highly simplified phenomenological s-process models used in the splitting procedure. These uncertainties and their impact on some nuclear astrophysics questions are studied in detail by [16]. Fig. 3 does not display the uncertainties in the s- or r-nuclide abundances. Most of those in the p-nuclides are considered to be small enough not to affect any of the conclusions of the p-process models to be discussed below, and are not represented either. Only some specific nuclides are affected by more significant uncertainties characterized by the vertical error bars drawn in Fig. 3. They relate directly to the possible production by neutron captures of ^{152}Gd and ^{164}Er, which may well have a dominant s-process character. This process might also be responsible for part of the solar abundances of ^{115}Sn [16,17], ^{180}Ta (Section 6.3) and ^{180}W.

Table 1
List of the species commonly classified as p-nuclides, with their solar system abundances relative to 10^6 Si atoms proposed by two compilations [13,15]

Nucleus	Anders and Grevesse [13]	Error (%)	Palme and Beer [15]	Error (%)
^{74}Se	0.55	6.4	0.6	5
^{78}Kr	0.153	18	0.19	—
^{84}Sr	0.132	8.1	0.12	5
^{92}Mo	0.378	5.5	0.38	5
^{94}Mo	0.236	5.5	0.23	5
^{96}Ru	0.103	5.4	0.1	10
^{98}Ru	0.035	5.4	0.03	10
^{102}Pd	0.0142	6.6	0.014	10
^{106}Cd	0.0201	6.5	0.02	10
^{108}Cd	0.0143	6.5	0.014	10
^{113}In	0.0079	6.4	0.008	10
^{112}Sn	0.0372	9.4	0.036	10
^{114}Sn	0.0252	9.4	0.024	10
^{115}Sn	0.0129	9.4	0.013	10
^{120}Te	0.0043	10	0.0045	10
^{124}Xe	0.00571	20	0.005	—
^{126}Xe	0.00509	20	0.004	—
^{130}Ba	0.00476	6.3	0.005	5
^{132}Ba	0.00453	6.3	0.005	5
^{138}La	0.000409	2	0.0004	5
^{136}Ce	0.00216	1.7	0.002	5
^{138}Ce	0.00284	1.7	0.003	5
^{144}Sm	0.008	1.3	0.008	5
^{152}Gd	0.00066	1.4	0.001	5
^{156}Dy	0.000221	1.4	0.0002	5
^{158}Dy	0.000378	1.4	0.0004	5
^{162}Er	0.000351	1.3	0.0004	5
^{164}Er	0.00404	1.3	0.0042	5
^{168}Yb	0.000322	1.6	0.0003	5
^{174}Hf	0.000249	1.9	0.0003	5
^{180}Ta	2.48e-06	1.8	2.00e-06	10
^{180}W	0.000173	5.1	0.0002	7
^{184}Os	0.000122	6.3	0.0001	5
^{190}Pt	0.00017	7.4	0.0001	10
^{196}Hg	0.00048	12	0.001	20

p-nuclides are derived from the elemental abundances measured, whenever possible, in chondritic meteorites of the CI1 type, and from terrestrial isotopic compositions. The noble gas abundances are obtained from the analysis of the solar wind. The reported uncertainties concern the elemental abundances only.

Table 1 lists the 35 species classically referred to as p-nuclides, including the five species mentioned above, along with their abundances proposed by two different compilations [13,15]. The reported uncertainties do not include possible s-process contaminations; they concern in fact the elemental abundances only. It is seen that the differences between the two data sources are not significant.

2.2. Isotopic anomalies in the solar composition

The solar-system composition has raised further astrophysical interest and excitement with the discovery that a minute fraction of the solar-system material has an isotopic composition which differs from that of the bulk. Such 'isotopic anomalies' are observed in quite a large suite of elements ranging from C to Nd (including the rare gases), and are now known to be carried by high-temperature inclusions of primitive meteorites, as well as by various types of meteoritic grains. The inclusions are formed from solar-system material out of equilibrium with the rest of the solar nebula. The grains are considered to be of circumstellar origin and have survived the process of incorporation into the solar system.

These anomalies contradict the canonical model of an homogeneous and gaseous protosolar nebula, and provide new clues to many astrophysical problems, like the physics and chemistry of interstellar dust grains, the formation and growth of grains in the vicinity of objects with active nucleosynthesis, the circumstances under which stars (and in particular solar-system-type structures) can form, as well as the early history of the Sun (in the so-called 'T-Tauri' phase) and of the solar-system solid bodies. Last but not least, they raise the question of their nucleosynthesis origin and offer the exciting perspective of complementing the spectroscopic data for chemically peculiar stars in the confrontation between abundance observations and nucleosynthesis models for a very limited number of stellar sources, even possibly a single one. This situation is in marked contrast with the one encountered when trying to understand the bulk solar-system composition, which results from the mixture of a large variety of nucleosynthesis events, and consequently requires the modeling of the chemical evolution of the Galaxy.

Several anomalies concern the p-nuclides. Broadly speaking, they can be divided into three categories. The first one involves anomalies attributable to the decay of radionuclides manufactured by the p-process, and whose lifetimes may be long enough ($\tau \gtrsim 10^5$ yr) for having been in live form in the early solar system before their eventual in-situ decay in meteoritic solids. The best documented cases of this kind concern ^{92}Nb and ^{146}Sm to be discussed in Sections 9.2 and 9.3.

The second category of isotopic anomalies affecting p-nuclides relates largely to presolar diamonds found in meteorites (e.g. [21] for a general account of the topic of meteoritic presolar grains). They have been identified as the carriers of a very special type of Xenon referred to as Xe-HL, which is characterized by correlated excesses of the r- (i.e. Heavy) and p- (i.e. Light) isotopes of Xe. The case of this puzzling anomaly is discussed in Section 9.1.

The third category involves anomalies discovered in specific meteoritic inclusions, and more recently in bulk meteoritic samples. As far as inclusions are concerned, two special FUN Ca–Al-rich ones referred to as C-1 and EK1-4-1 identified in the meteorite Allende[1] exhibit a variety of abundance patterns of the stable isotopes of Sr, Ba and Sm that differ more or less markedly from the solar mix of p-, s- and r-nuclides (Fig. 3). More specifically, and as illustrated in Figs. 5 and 6, it is found that the two inclusions are characterized by an excess (with respect to the s-component), a deficit or a normal p-component of, respectively, Sm (^{144}Sm), Sr (^{84}Sr) or Ba (^{130}Ba and ^{132}Ba) [18]. Excesses in the r-isotopes of Ba and Sm are also found, but in EK1-4-1 exclusively.

[1] The Ca–Al-rich inclusions are presumably the first solids to have formed in the solar system in view of their high condensation temperatures. C-1 and EK1-4-1 are of the special FUN (for Fractionation and Unknown Nuclear effects) class, the very origin of which is still puzzling.

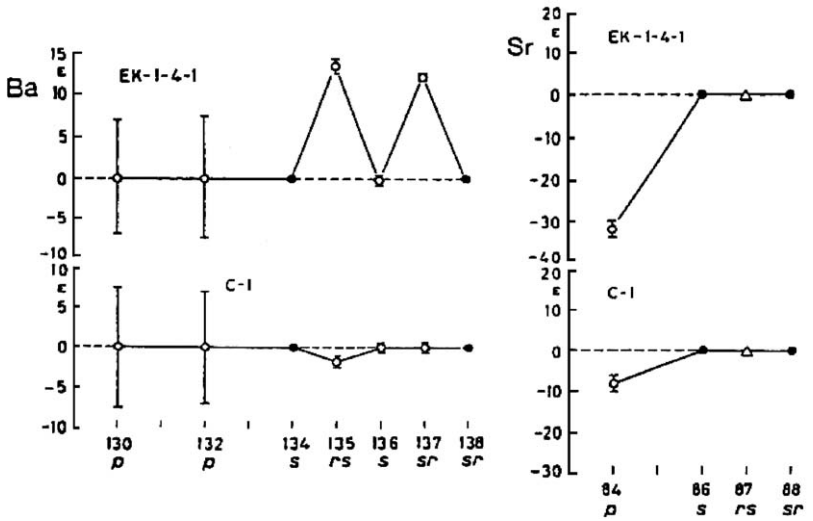

Fig. 5. Isotopic anomalies for the elements Sr and Ba observed in the Allende FUN inclusions C-1 and EK1-4-1 (from [18]), and for Mo in the Allende Ca–Al-rich inclusion A44A (from [19]). The anomaly of isotope i is expressed as $\varepsilon = 10^4 \times [(N_i/N_{\rm norm})_{\rm FUN}/(N_i/N_{\rm norm})_{\rm stand} - 1]$, where N_i is the abundance of i either in the considered inclusions (subscript FUN), or in the ('solar') sample adopted as the isotopically normal standard (subscript stand). The isotope(s) used for normalization is(are) made only or predominantly by the s-process and has(have) an abundance $N_{\rm norm}$. Positive(negative) ε values represent excesses(deficits) with respect to the s-isotopes used for normalization.

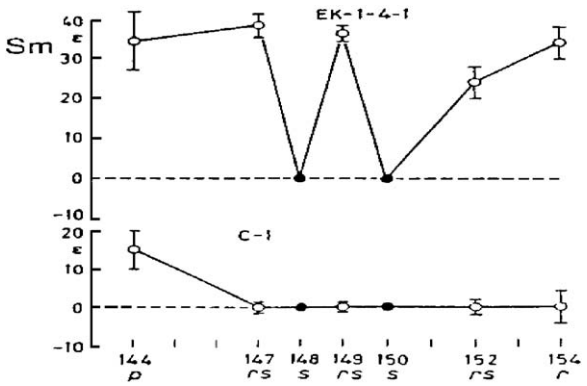

Fig. 6. Same as Fig. 5, but for the Sm isotopic composition.

Recently, Mo isotopic anomalies have also been observed in the Allende Ca–Al-rich inclusion A44A [19]. This element is of special p-process significance in view of the relatively high solar-system abundances of its two p-isotopes ^{92}Mo and ^{94}Mo (Fig. 3). Fig. 7 shows that ^{94}Mo has a normal abundance with respect to ^{96}Mo and ^{98}Mo in this inclusion (no data are reported for ^{92}Mo), while there is an indication of an excess of the r-isotope ^{100}Mo, as well as, to a lesser extent, of the sr-nuclide ^{97}Mo. The A44A p-isotope normality is at variance with recent measurements of the Mo isotopic composition in *bulk* samples of meteorites of different types (Figs. 8 and 9). Restricting to

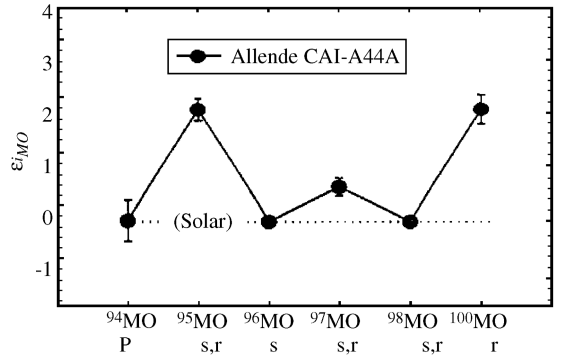

Fig. 7. Same as Fig. 5, but for Mo in the Allende Ca–Al-rich inclusion A44A (from [19]).

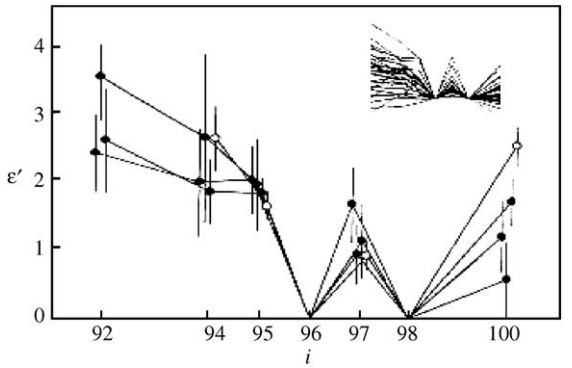

Fig. 8. Anomalous Mo isotopic patterns observed in the bulk of the carbonaceous chondrite Allende, as well as of various meteorites of the iron, mesosiderite and pallasite types (top right insert, where the upper curves correspond to Allende). The ε scale is defined as in Fig. 5, and the normalizing isotope is ^{96}Mo (from [20]).

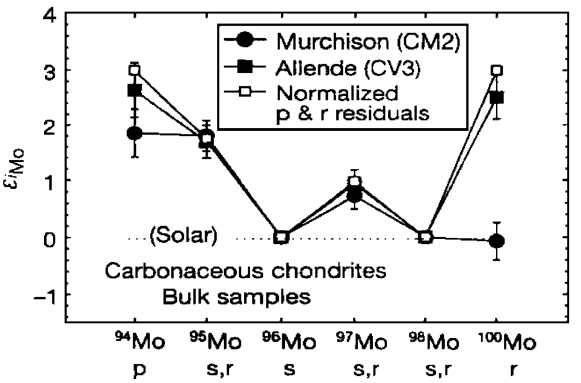

Fig. 9. Same as Fig. 8, but for bulk samples of the carbonaceous chondrites Murchison and Allende analyzed by [19]. The Allende data largely agree with those of [20].

the carbonaceous chondrites, Allende exhibits a special 'Mo–W' pattern characterized by excesses in both the p- and r-isotopes. The p-isotope excess persists in the Murchison bulk sample, but no r-excess is present. As in A44A, ^{97}Mo is found to be overabundant in the bulk samples of both Allende and Murchison. At this point, the question of the very nature of the carriers of the anomalous Mo, and in particular of the p-isotope excesses found in bulk meteoritic samples remains to be answered. Another problem concerns the positive ^{97}Mo anomaly. It naturally raises the prospect of a contribution to this nuclide of the in-situ decay of live ^{97}Tc ($t_{1/2} = 4.0 \times 10^6$ yr) in the early solar system. This interpretation is not favoured, however, by [20]. Other observations [22] leave the door open to this possibility, but do not demonstrate it. As the aforementioned ^{92}Nb and ^{146}Sm, ^{97}Tc, as well as ^{98}Tc ($t_{1/2} = 4.2 \times 10^6$ yr), can be made in the p-process [12,23,24]. As predicted by [25], it could be synthesized in the s-process as well. This would of course blur any possible connection between the p-process and the solar-system in-situ decay of a radionuclide other than ^{92}Nb or ^{146}Sm.

3. The nuclear physics of relevance to the p-process

As already mentioned in Section 1, the p-process is essentially made of photodisintegrations of the (γ,n), (γ,p) or (γ,α) types, possibly complemented with captures of neutrons, protons or α-particles at centre-of-mass energies typically far below 1 MeV or the Coulomb barrier in the case of charged particles. Weak-interaction transformations (β-decays, $e^{\pm}$-captures or (anti)neutrino captures) may also play a role in specific conditions and for particular cases (see e.g. Section 6.2). The reliable modeling of the p-process flows necessitates the consideration of an extended network of some 20 000 reactions linking about 2000 nuclei in the $A \leqslant 210$ mass range.

A flow which is typical of the p-process developing in Type II supernovae is represented schematically in Fig. 10, and helps identifying the nuclear needs for the modeling of the p-process. This flow is seen to be located in a neutron-deficient region of the chart of the nuclides. It may happen that this flow follows precursor transformations which can in particular drive part of the material into the neutron-rich region. This is most vividly illustrated by the p-process accompanying the explosion of sub-Chandrasekhar mass white dwarfs (Section 8.3 and Fig. 49).

The flow depicted in Fig. 10 is located in a region of the nuclidic chart where most masses are known experimentally. Some details about the laboratory situation are provided in Section 3.3.2. Concomitant progress has been made in the experimental knowledge of β^+-decay or electron-capture rates. It has to be noticed, however, that these laboratory lifetimes may have to be corrected for continuum electron captures which could develop in the stellar conditions relevant to the p-process, as well as for the contribution to the β-decays of excited states of the parent nuclei which can be populated in the relevant astrophysical situations (e.g. [2] for generalities about stellar weak interaction processes). The state of affairs is by far less satisfactory concerning the laboratory knowledge of the rates of the nuclear reactions involved in the p-process networks. We review below the experimental situation regarding reactions that involve neutrons (Section 3.1) or charged particles (Section 3.2). The scarcity of the relevant information makes it mandatory to rely heavily on rate predictions. The situation in this respect is presented in Section 3.3.

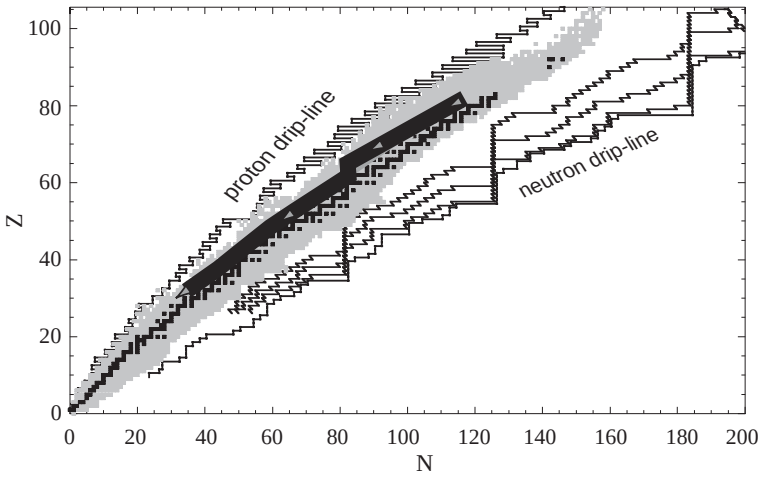

Fig. 10. A schematic Type II supernova p-process nuclear flow (thick line; see also Fig. 4). It has the remarkable property of streaming down in mass in a region of neutron-deficient nuclides for which experimental masses and β-decay probabilities have been measured [26] (black squares for nuclei at the bottom of the valley of nuclear stability, gray squares elsewhere). This contrasts dramatically with the situation encountered in the r-process, typical flows of which are represented by thin solid lines. They are almost entirely located in regions for which masses and β-decay rates are essentially unknown experimentally, the only exceptions to this rule being encountered for some nuclei near neutron closed shells. The proton and neutron drip lines (locations of zero proton or neutron separation energies) are predicted by the HFBCS mass table of [27].

3.1. Captures of neutrons and photoreactions: experimental situation

Most of the rate measurements of relevance to the p-process concern radiative captures by *stable* targets, which of course covers not more than a minute fraction of the needs for p-process calculations. They also concern the target ground state only, so that a correction factor has to be applied to the laboratory data in order to account for the possible contribution of the target excited states to the stellar capture rates (Section 3.3). This large body of experimental data [28] plays an important role in the validation of the various nuclear ingredients entering theoretical predictions (see Section 3.3). They can also be used to estimate reverse photonuclear rates needed for the p-process modeling through the application of the reciprocity theorem, after due inclusion of the possible contribution to the (n,γ) rates of target excited states.

Many (γ,n) cross sections have also been measured directly at energies around the giant dipole resonance (GDR) [29,30]. They are not of direct astrophysical relevance, however, as the energies of interest for the p-process lie close to the photodisintegration threshold, as seen in Fig. 11. Recent experiments have provided direct measurements of some (γ,n) reactions at these low energies. They are worth a brief summary.

One of these techniques is based on real photons produced in bremsstrahlung experiments by stopping electrons in a radiator material. These photons are characterized by a continuous energy distribution that rapidly decreases towards the endpoint energy corresponding to the incident electron energy. As illustrated in Fig. 11, a superposition of such bremsstrahlung spectra with different endpoint energies provides a γ-ray distribution n_γ that can approximate very satisfactorily a black-body Planck spectrum at a given temperature T [31]. This Planck spectrum is itself remarkably close to

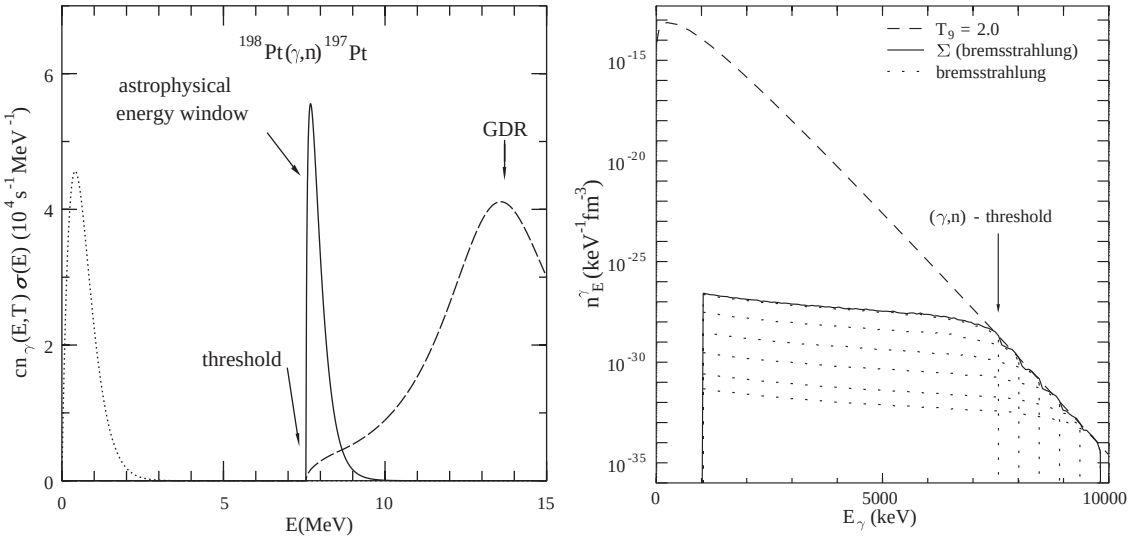

Fig. 11. Left panel: Graphical display of the integrand function of Eq. (1) for the ^{198}Pt(γ,n)^{197}Pt reaction. The Planck spectrum n_γ at a temperature $T = 2 \times 10^9$ K is shown, as well as the $\sigma_{(\gamma,n)}(E)$ cross section from energies slightly higher than the GDR down to threshold $E_{\rm thr}$. Near this energy, the photoneutron cross section is *assumed* to be given by $\sigma_{(\gamma,n)}(E) = \sigma_0 \sqrt{(E - E_{\rm thr})/E_{\rm thr}}$, σ_0 being determined by the bremstrahlung experiment. The energy window of astrophysical interest has typically a width of less than 1 MeV located around the effective energy $E_{\rm eff} \approx E_{\rm thr} + kT/2$, and is thus very close to threshold for conditions relevant to the p-process; Right panel: Approximation of the Planck spectrum at $T = 2.5 \times 10^9$ K in the approximate 5–10 MeV energy range by a superposition $\Phi = \sum_{i=1}^{6} a_i(T = 2.5 \times 10^9)\Phi_{\rm brems}(E_{0,i})$ of 6 bremsstrahlung spectra $\Phi_{\rm brems}$ with different endpoint energies $E_{0,i}$ (from [31]).

the γ-ray distribution at a location at that temperature in stellar interiors (e.g. [32]). In such conditions, and assuming a target nucleus in its ground state, the stellar rate at temperature T of the (γ, j) photodisintegration is expressed from n_γ as

$$\lambda_{(\gamma,j)}(T) = \int_0^\infty c n_\gamma(E,T)\sigma_{(\gamma,j)}(E)\,{\rm d}E \ , \tag{1}$$

where c is the speed of light, and $\sigma_{(\gamma,j)}(E)$ the photodisintegration cross section at energy E.

Another method relies on the use of a real photon beam in the MeV region produced by head-on collisions of laser photons on relativistic electrons [33–35]. This technique, referred to as the 'laser inverse compton (LIC)' γ-ray source [36], produces quasi-monochromatic γ-rays of 1–40 MeV. The LIC technique has some important advantages over the bremsstrahlung one. On the one hand, the produced γ-rays have a higher quasi-monochromaticity, and are much more peaked in the energy window of astrophysical interest (see Fig. 11). On the other hand, the LIC approach provides absolute cross section measurements, while the bremsstrahlung technique requires an assumption to be made on the energy dependence of the photodisintegration cross section near threshold ([31] adopt $\sigma_{(\gamma,n)}(E) \propto \sqrt{(E - E_{\rm thr})/E_{\rm thr}}$, where $E_{\rm thr}$ is the threshold energy; see Fig. 11).

The bremsstrahlung and LIC techniques have been used up to now to measure the rates of some (γ,n) reactions [31,33–35]. In particular, the latter experimental approach has been applied to the ^{181}Ta(γ,n)^{180}Ta of special interest in the p-process modeling (Section 6.3). It has even provided an information on the relative production by this reaction of the ground and isomeric states of ^{180}Ta.

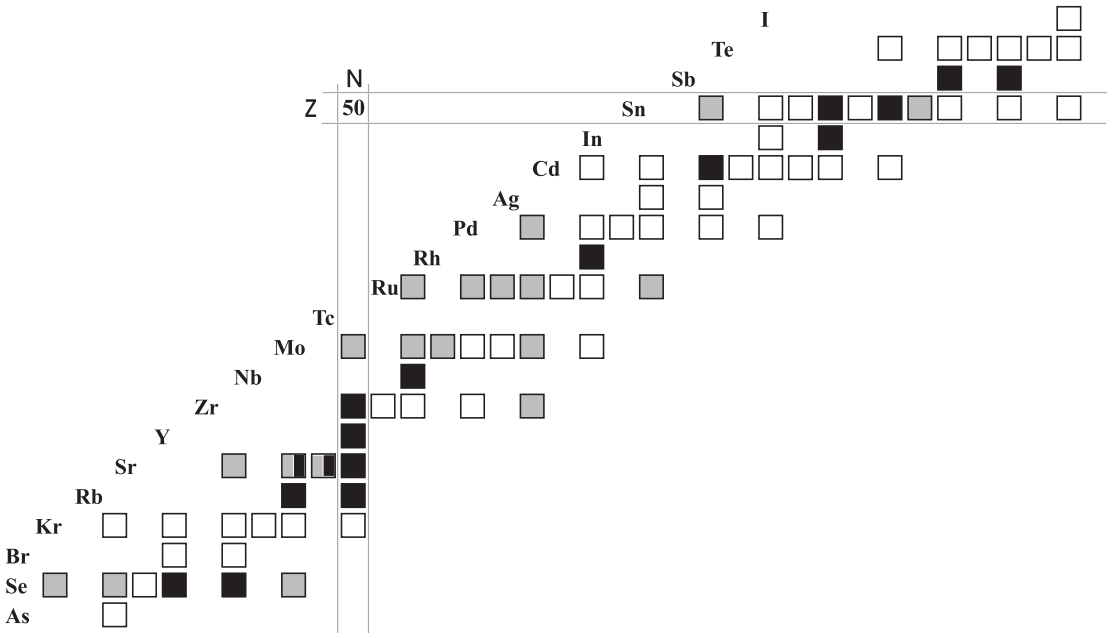

Fig. 12. Synopsis (as of June 2002) of the targets heavier than iron on which (p,γ) reaction cross sections have been measured at low enough energies to be of astrophysical interest. The grey squares represent cases studied through activation techniques making use of natural targets, so that data for all isotopes can be obtained from one measurement. Enriched targets used for in-beam experiments are drawn as black squares. Both techniques have been used for ^{86}Sr and ^{87}Sr. The experimental data are from the following references: ^{74}Se, ^{76}Se, ^{82}Se (^{nat}Se): [37]; ^{78}Se (enriched): [38]; ^{80}Se (enriched): [38]; ^{85}Rb, ^{87}Rb (^{nat}Rb): [38]; ^{84}Sr, ^{86}Sr, ^{87}Sr (^{nat}Sr): [39]; ^{87}Sr (enriched): [38]; ^{88}Sr (enriched): [40]; ^{89}Y: [38]; ^{90}Zr (enriched): [41]; ^{96}Zr: [42]; ^{93}Nb: [43]; ^{92}Mo, ^{94}Mo, ^{95}Mo, ^{98}Mo (^{nat}Mo): [44]; ^{96}Ru, ^{98}Ru, ^{99}Ru, ^{100}Ru, ^{104}Ru (^{nat}Ru): [45]; ^{103}Rh: [38]; ^{102}Pd (enriched): [46]; ^{110}Cd (enriched): [38]; ^{113}In, ^{115}In (^{nat}In): [38]; ^{112}Sn (enriched): [42]; ^{116}Sn (enriched): [38]; ^{118}Sn (enriched): [38]; ^{119}Sn (enriched): [42]; ^{121}Sb, ^{123}Sb (^{nat}Sb): [38] (from S. Harissopulos, private communication).

The feasibility of the measurement of the rate of ^{180}Ta(γ,n)^{179}Ta, which is a necessary complement to the already measured one on ^{181}Ta, as well as of the rates of ^{139}La(γ,n)^{138}La and ^{138}La(γ,n)^{137}La of direct relevance to the synthesis of the rare odd–odd p-nuclide ^{138}La (Section 6.2) is currently under investigation (H. Utsunomiya, private communication).

3.2. Captures of charged particles: experimental situation

Experimental data are even scarcer for charged-particle induced reactions of p-process interest than for reactions involving neutrons. This situation is largely due to the smallness of the related reaction cross sections at the sub-Coulomb energies of astrophysical interest. Fig. 12 presents a synopsis of the targets heavier than iron on which (p,γ) reaction cross sections have been measured by now at low enough energies to be of astrophysical relevance. These experiments make use of two techniques, the activation method and in-beam measurements. As seen in Fig. 12, data are available only for stable targets up to about Sn (the $Z = 50$ shell closure). Some of them are presented and confronted with

model predictions in Section 3.3. An extension of the experimental efforts towards $Z > 50$ targets would be most valuable in order to better constrain and improve global reaction models (Section 3.3). These will have to provide for a very long time to come the remaining thousands of (p,γ) reaction rates that enter, through the reciprocity theorem (Eq. (5)), the evaluation of the reverse (γ,p) of key importance in the p-process networks. Theory has also to supply an estimate of the contribution to the reaction mechanism of the target excited states.

Data on (α,γ) reactions that are needed to derive the rates of the inverse photodisintegrations are even fewer than in the proton case. At this point, the only reactions that have been studied experimentally at sub-Coulomb energies and on targets heavier than iron are ^{70}Ge(α,γ)^{74}Se [47], ^{96}Ru(α,γ)^{100}Pd [48], ^{112}Sn(α,γ)^{116}Te [49] and ^{144}Sm(α,γ)^{148}Gd [50], the latter reaction being of special astrophysical interest (see Section 9.3). These measurements are important in the modeling of the α-particle–nucleus optical potentials at low energies (Sections 3.3.4 and 3.4). In this respect, reactions of the (α,n), (n,α) or (α,p) types are also of interest. Cases studied at sub-Coulomb energies can be found in [48,51,52].

3.3. Theoretical evaluation of reaction rates

In spite of an important effort devoted in the last decades to measurements of reaction cross sections for astrophysical purposes in general (e.g. [2]), and more recently for p-process studies in particular, major difficulties related to the specific conditions prevailing in the astrophysical plasmas remain, as already underlined at several occasions previously. In particular, charged-particle induced reactions at stellar energies (far below the Coulomb barrier) have extremely small cross sections that raise major experimental difficulties. In addition, a huge number (thousands) of reactions of relevance to the p-process involve unstable or even exotic nuclides (of the neutron-deficient as well as neutron-rich types in some sites, as illustrated in Section 8.3). Clearly, many of these reaction rate experiments will remain unfeasible for a long time to come. Theory has thus to supply the necessary data, which also represents a major challenge. Even if, as said before, some relief comes from the fact that most of the masses of the nuclei involved in the p-process have been measured, so that the reaction energetics is put on safe grounds, many nuclear properties entering directly the rate calculations remain to be predicted, as briefly reviewed below. Concomitantly, as already mentioned above, specific stellar plasma effects come into play, like the contribution of target excited levels to the reaction mechanisms which develops as temperatures increase, and can become significant in p-process conditions. Weak interaction transformations occurring in laboratory conditions are also affected by stellar plasma effects, and even new processes can develop (e.g. [2]).

3.3.1. Reaction rate calculations: general framework

Nucleon or α-particle captures relevant to the p-process involve heavy targets. If the density of levels of the compound systems formed as a result of these captures is high enough, it is known that a statistical model for the reactions can be used. This is indeed the case if the heavy targets are far enough from the proton drip line to ensure that the excitation energies of the compound systems are high enough. This constraint is certainly met to a large extent for typical p-process nuclear flows, as schematized in Fig. 10 (it is also seen there that the situation may be quite different for the r-process). All existing p-process calculations rely in fact on a statistical model of the Hauser–Feshbach (HF) type [53,54]. In this framework, the reaction $I^{\mu} + j \rightarrow L + k$ of capture of a nucleon

or α-particle j on target I in its state μ leaving the residual nucleus L and particle or photon k has a cross section at centre-of-mass energy E given by

$$\sigma_{jk}^{\mu}(E) = \pi \lambda\!\!\!^{-2}_{j} \frac{1}{(2J_I^{\mu}+1)(2J_j+1)} \sum_{J^{\pi}} (2J+1) \frac{T_j^{\mu}(J^{\pi}) T_k(J^{\pi})}{T_{\rm tot}(J^{\pi})} \ , \tag{2}$$

where J_I and J_j are the target and projectile spins, and $T_j(J^{\pi})$ is the transmission coefficient measuring the probability for forming the compound nucleus (i.e. the compound system assumed in the HF model to have reached a state of thermodynamic equilibrium) in its state J^{π} obtained from all possible combinations of the orbital and channel spins. Similarly, $T_k(J^{\pi}) = \sum_{\nu} T_k^{\nu}(J^{\pi})$ is the transmission coefficient for the decay of the compound nuclear state into the pair $L+k$, all states ν of L which can be populated in the reaction being taken into account. $T_{\rm tot}(J^{\pi}) = \sum_{i,\lambda} T_i^{\lambda}(J^{\pi})$ corresponds to the total transmission coefficient for the decay of the compound state J^{π} into any combination i of nucleus and particle which can be formed from all its possible decay modes λ (including $I+j$ and $L+k$). It has to be noted that Eq. (2) is valid only if the formation and decay of the compound nucleus are totally independent. This so-called Bohr hypothesis may not be fully satisfied, particularly in cases where a few strongly and many weakly absorbing channels are mixed. As an example, Eq. (2) is known to be invalid when applied to the elastic channel, since in that case the transmission coefficients for the entrance and exit channels are identical, and hence correlated. This causes an elastic enhancement. To account for these deviations, width fluctuation corrections can be introduced in the HF formalism by different approximate expressions [55,56].

Each transmission coefficient is estimated from the sum over all levels with experimentally known energy, spin and parity. At excitation energies for which the required data are not available, this sum transforms into an integral over a nuclear level density, so that

$$T_k(J^{\pi}) = \sum_{\nu=0}^{\omega} T_k^{\nu}(J^{\pi}) + \int_{\varepsilon^{\omega}}^{\varepsilon^{max}} \int_{J^{\nu},\pi^{\nu}} T_k^{\nu}(\varepsilon^{\nu},J^{\pi}) \rho(\varepsilon^{\nu},J^{\nu},\pi^{\nu}) \, {\rm d}\varepsilon^{\nu} \, {\rm d}\pi^{\nu} \, {\rm d}J^{\nu} \ , \tag{3}$$

where ε^{ω} is the energy of the highest experimentally known bound excited state ω of L (or more precisely the state up to which the knowledge of the energy spectrum is considered to be reasonably complete), and $\rho(\varepsilon^{\nu},J^{\nu},\pi^{\nu})$ is the density per unit energy interval of L states with spin J^{ν} and parity π^{ν} at the excitation energy ε^{ν}. Similar formulae apply to the other transmission coefficients in Eq. (2).

A thermodynamic equilibrium holds locally to a very good approximation in stellar interiors (e.g. [32]). Consequently, the energies of both the targets and projectiles, as well as their relative energies E, obey Maxwell–Boltzmann distributions corresponding to the temperature T at that location. In such conditions, the rate of $I^{\mu}+j \rightarrow L+k$ per pair of particles in the entrance channel and at T is obtained by integrating the cross section given by Eq. (2) over a Maxwell–Boltzmann distribution of energies E at the given temperature. In addition, in hot astrophysical plasmas, a target nucleus exists in its ground as well as excited states. In a thermodynamic equilibrium situation, the relative populations of the various levels of nucleus I^{μ} with excitation energies ε_I^{μ} ($\mu = 0$ for the ground state) obey a Maxwell–Boltzmann distribution. The effective stellar rate of $I+j \rightarrow L+k$ per pair of particles in the entrance channel at temperature T taking due account of the contributions of the

various target excited states is finally expressed in a classical notation as

$$N_A\langle\sigma v\rangle^*_{jk}(T) = \left(\frac{8}{\pi m}\right)^{1/2} \frac{N_A}{(kT)^{3/2}G(T)} \int_0^\infty \sum_\mu \frac{(2J_I^\mu+1)}{(2J_I^0+1)}\,\sigma^\mu_{jk}(E)E\exp\left(-\frac{E+\varepsilon_I^\mu}{kT}\right)\mathrm{d}E\ , \qquad (4)$$

where k is the Boltzmann constant, m the reduced mass of the I^0+j system, N_A the Avogadro number, and $G(T)=\sum_\mu(2J_I^\mu+1)/(2J_I^0+1)\exp(-\varepsilon_I^\mu/kT)$ the temperature-dependent normalized partition function. Reverse reactions can also be estimated making use of the reciprocity theorem [54]. In particular, the stellar photodissociation rates are classically derived from the reverse radiative capture rates by

$$\lambda^*_{(\gamma,j)}(T) = \frac{(2J_I+1)(2J_j+1)}{(2J_L+1)}\,\frac{G_I(T)}{G_L(T)}\left(\frac{A_IA_j}{A_L}\right)^{3/2}\left(\frac{kT}{2\pi\hbar^2N_A}\right)^{3/2} N_A\langle\sigma v\rangle^*_{(j,\gamma)}\mathrm{e}^{-Q_{j\gamma}/kT}\ , \qquad (5)$$

where $Q_{j\gamma}$ is the Q-value of the $I^0(j,\gamma)L^0$ capture. Note that, in stellar conditions, the reaction rates for targets in thermal equilibrium obey reciprocity since the forward and reverse channels are symmetrical, in contrast to the situation which would be encountered for targets in their ground states only [54]. The total stellar photodissociation rate can also be determined directly from

$$\lambda^*_{(\gamma,j)}(T) = \frac{\sum_\mu(2J^\mu+1)\lambda^\mu_{(\gamma,j)}(T)\exp(-\varepsilon^\mu/kT)}{\sum_\mu(2J^\mu+1)\exp(-\varepsilon^\mu/kT)}\ , \qquad (6)$$

where the photodissociation rate $\lambda^\mu_{(\gamma,j)}$ of state μ with excitation energy ε^μ is given by Eq. (1).

The uncertainties involved in any HF cross section calculation are not related to the model of formation and de-excitation of the compound nucleus itself (except through the width fluctuation correction), but rather to the evaluation of the nuclear quantities necessary for the calculation of the transmission coefficients entering Eqs. (2)–(4). Clearly, the knowledge of the ground state properties (masses, deformations, matter densities) of the target and residual nuclei is indispensable. When not available experimentally (a quite unusual situation, however, for the masses of the nuclei involved in the p-process; see Fig. 10), this information has to be obtained from nuclear mass models. The excited state properties have also to be known. Experimental data may be scarce above some excitation energy, and especially so for nuclei located far from the valley of nuclear stability. This is why frequent resort to a level density prescription is mandatory. The transmission coefficients for particle emission are calculated by solving the Schrödinger equation with the appropriate optical potential for the particle–nucleus interaction. Finally, the photon transmission function is calculated assuming the dominance of dipole $E1$ transitions (the $M1$ transitions are usually included as well, but do not contribute significantly. They will not be discussed further here). Reaction theory relates the γ-transmission coefficient for excited states to the ground state photoabsorption assuming the GDR to be built on each excited state. These resonances are classically estimated within a Lorentzian representation, at least for medium- and heavy-mass nuclei. Experimental photoabsorption data confirm the simple semi-classical prediction of a Lorentzian shape at energies around the resonance energy. However, this description is less satisfactory at lower energies, and especially near the reaction threshold (see Sections 3.3.5 and 3.4).

Ideally, these various necessary ingredients (properties of cold and hot nuclei, nuclear level densities, optical potentials, γ-ray strength functions) should have to be derived from *global*, *universal*

and *microscopic* models. The large number of nuclides involved in the modeling of some nucleosynthesis mechanisms, and in particular of the p-process (a few thousand nuclei in this case) demands the use of global models. On the other hand, a universal description of all nuclear properties within a unique framework for all nuclei involved in a nuclear network ensures the essential coherence of the predictions of all unknown data. Finally, a microscopic description provided by a physically sound theory based on first principles ensures extrapolations away from experimentally known energy or mass regions that are likely to be more reliable than predictions derived from more or less parametrized approaches of various types and levels of sophistication. These include, between the extreme approaches provided by local macroscopic approaches and global microscopic ones, models referred to as classical, semi-classical, macroscopic–microscopic (e.g. classical with microscopic corrections), or semi-microscopic (e.g. microscopic with phenomenological corrections).

Over the last decades, much progress has been made in the development of global microscopic models. However, they are almost never used for practical applications because of their poorer agreement with experimental data (especially large data sets) than the less microscopic approaches listed above. This situation is of course the direct consequence of the freedom offered by the latter models to tune properly a more or less large number of free parameters. This ability of the non-microscopic models to account for experimental data with a relatively high accuracy has clearly the major drawback of a loss of reliability when one is forced to extrapolate to experimental terra incognita. For applications, in particular of astrophysics nature, where nuclei far from stability are involved, the use of microscopic models has clearly to be preferred. This is even more so as new generations of such models are started to be developed which can compete with more phenomenological highly-parametrized models in the reproduction of experimental data [57,58].

3.3.2. Ground state properties

Atomic masses are obviously key quantities entering all chapters of nuclear astrophysics, and in particular the calculations of the rates of nuclear reactions or weak interaction transformations. Recently, impressive progress has been made experimentally. This situation results largely from recent measurements with Penning-trap [59] or Schottky [60] spectrometers which have enlarged the region of known masses, in particular towards the neutron-deficient side of the valley of nuclear stability of direct interest for the p-process. The new Atomic Mass Evaluation [26] contains 2214 measured masses, i.e. 250 more than the 1995 one [61]. A more accurate mass determination is also available now for about 132 nuclides originally included in the 1995 compilation. Less progress has been made on the neutron-rich side of the chart of the nuclides, where the premises of the p-process may take place in some situations (e.g. Section 8.3). Over the last six years, only some 30 new masses have been measured in that region with a poor resolution. The calculation of the reaction and decay rates also requires the knowledge of other ground state properties, such as the deformation, density distribution, single-particle level scheme, pairing force and shell correction energies, for which nuclear structure theory must provide estimates.

Attempts to evaluate nuclear masses go back to the liquid-drop mass formula of [62]. Improvements to this original model have been brought little by little, leading to the development of macroscopic–microscopic mass formulae, the most sophisticated version of which is the ‘finite-range droplet model’ (FRDM) [63]. In this framework, the macroscopic contribution to the masses and the microscopic corrections of phenomenological nature are treated independently, both parts being

connected solely through a parameter fit to experimental masses. Despite the great empirical success of the FRDM formula (it fits the 2135 $Z \geqslant 8$ experimental masses [26,61] with an rms error of 0.676 MeV), it suffers from major shortcomings, such as the incoherency of the link between the macroscopic part and the microscopic correction, the instability of the mass prediction to different parameter sets, or the instability of the shell corrections. As a consequence, its reliability when extrapolating far from experimentally known masses is severely limited. For astrophysics and other applications, there is an obvious need to develop a mass model that is more closely connected to the basic nuclear interaction properties. The result is that the most microscopically founded mass formulae of practical use were till recently those based on the so-called ETFSI (extended Thomas–Fermi plus Strutinsky integral) method [64]. The ETFSI method is nothing else than a high-speed macroscopic–microscopic approximation to the Hartree–Fock method based on Skyrme forces, with pairing correlations generated by a δ-function force that is treated in the usual BCS approach (with blocking). The macroscopic part consists of a purely semi-classical approximation to the Hartree–Fock method, the full fourth-order extended Thomas–Fermi method. The microscopic part (based on the integral form of the Strutinsky theorem) constitutes an attempt to improve this approximation perturbatively, and in particular to restore the shell corrections that are missing from the ETF part. The latest version of the ETFSI mass table [65] reproduces the 2031 $A \geqslant 36$ experimental masses with an rms of 0.730 MeV.

A new major progress has been achieved recently within the Hartree–Fock method [27,66,67]. It is now demonstrated that this microscopic approach, making use of a Skyrme force fitted to essentially all the mass data, is not only feasible, but can successfully compete with the most accurate droplet-like formulae available nowadays concerning the quality of reproduction of measured masses. As illustrated in Fig. 13, this holds true not only when the pairing force is described in the BCS approximation (HFBCS model), but also when the Bogoliubov method is adopted (HFB model), which has the advantage of ensuring the self-consistency of the treatment of the nuclear single-particle and pairing properties. The most recent large-scale HFB calculations [67] make use of a conventional 10-parameter Skyrme force along with a 4-parameter δ-function pairing force. The Skyrme and pairing parameters are derived from a fit to the full data set of 2135 measured masses of nuclei with $Z,N \geqslant 8$, leading to an rms error of 0.674 MeV. A complete mass table, referred to as HFB-2, results. It provides all ground state properties for nuclei lying between the two drip lines over the range of Z and $N \geqslant 8$ and $Z \leqslant 110$. Fig. 14 provides a comparison between the HFB and FRDM predictions. It demonstrates vividly that two mass models which reproduce measured masses with comparable rms deviations can diverge more or less markedly in their predictions for nuclei far from stability. It should also be noted that, even if the HFB and FRDM mass parabolas present more or less the same slope, they sometimes differ noticeably in their predicted deformations or shell structures. These differences may influence the nucleosynthesis predictions.

3.3.3. Nuclear level densities

Although reliable microscopic models (mainly based on statistical or combinatorial approaches) have been developed over the last four decades to estimate nuclear level densities (NLDs), only approaches based on the Fermi gas approximation have been used until recently for practical applications (e.g. [68]). This results mainly from the fact that they provide a mean to estimate NLDs through the use of simple analytical formulae. They are unfortunately always obtained at the expense of drastic approximations concerning in particular the description of the shell, deformation and

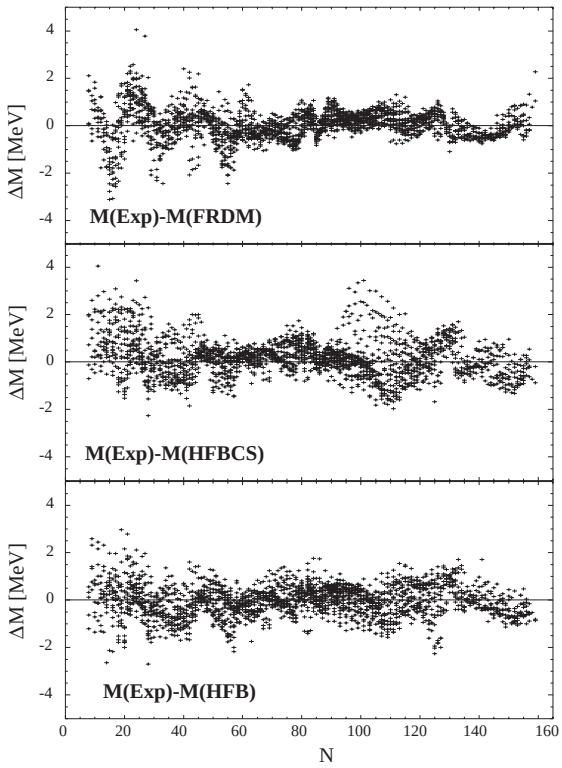

Fig. 13. Comparison between measured masses [26] and the predictions of three mass models: FRDM [63] (upper panel), HFBCS [27] (middle), and HFB [67] (lower).

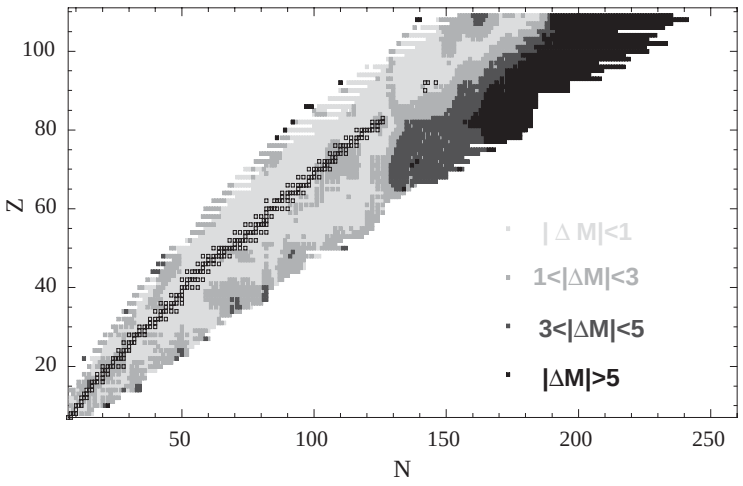

Fig. 14. Mapping of the chart of the nuclides in the ranges N and $Z \geqslant 8$ and $Z \leqslant 110$ with the differences $\Delta M = M_{\mathrm{HFB}} - M_{\mathrm{FRDM}}$ (in MeV) between the HFB and FRDM theoretical predictions. The differences are coded as indicated in the figure.

pairing effects. As an illustration, the formulations of the back-shifted Fermi gas (BSFG) type, which are of most common use today, just introduce some phenomenological improvements to the original prescription of [69]. In particular, use is made of a highly simplified energy dependence of the key 'NLD parameter' a which cannot account properly for the nuclear excitation spectra. In addition, the complex pairing effects are just described in terms of a simple energy shift. In such conditions, it is not surprising that the existing analytical NLD prescriptions are unable to match the experimental data with a reasonable level of accuracy. This shortcoming is cured to some extent by adjustments of a more or less large number of free parameters. Such a procedure introduces, however, a substantial unreliability if predictions have to be made when experimental data are scarce or non-existent, as it is very often the case in certain, sometimes extended, ranges of excitation energies, or for nuclei far from stability of importance for the modeling of the p-process and for a large variety of other applications. The lack of measured level densities still constitutes the main problem faced by the NLD models and the parameter fitting procedures they require, even if the number of analyses of slow neutron resonances and of cumulative numbers of low energy levels grows steadily. This concerns in particular the s-wave neutron resonance spacings D at the neutron separation energy S_n. For a nucleus $(Z,A+1)$ resulting from the capture of a low-energy neutron by a target (Z,A) with spin J_0, D is given by

$$D = \frac{2}{\rho(S_n, J_0 + 1/2) + \rho(S_n, J_0 - 1/2)} \quad \text{for } J_0 > 0 \ ,$$
$$= \frac{2}{\rho(S_n, 1/2)} \quad \text{for } J_0 = 0 \ , \tag{7}$$

the factor of 2 in the numerator relating to the classical assumption of equal probabilities of both parities π at all energies. The separation D is thus a direct measure of the spin-dependent level density $\rho(U,J)$ in the nucleus $(Z,A+1)$ at the excitation energy $U = S_n$. Other sources of information have also been suggested, such as the analysis of spectra of evaporated particles and coherence widths of cross section fluctuations. However, most of these experimental data are affected by systematic errors resulting from experimental uncertainties, as well as from the use of approximate models.

The NLD predictive power can be largely enhanced if the requirement of analytical formulations is relaxed, which allows to duly take quantitatively into account various nuclear properties, and in particular the discrete structure of the single-particle spectra derived from realistic effective nuclear interactions. Such a 'microscopic' approach has the major advantage of treating in a consistent way shell, pairing and deformation effects when evaluating the thermodynamic quantities that enter the NLD calculations. It is, however, not free from some problems related to the very choice of the nuclear and pairing interactions. In this spirit, [70] calculates NLDs by using the single-particle level scheme and pairing strength of the ETFSI model (Section 3.3.2). This work reproduces experimental data (neutron resonance spacings at the neutron separation energy) reasonably well, as illustrated in Fig. 15, and demonstrates the interest and viability of microscopic evaluations of the NLDs, even if some clear disagreements exist between theory and experiments. In fact, these deficiencies are cured in a HFBCS-based model (Section 3.3.2) developed by [71]. In this framework, the experimental s-wave resonance spacings at the neutron separation energy are reproduced with an accuracy of typically a factor of about 2, which is comparable to the one obtained with a free parameter fit by the phenomenological BSFG formula [71] (see Fig. 15). It also provides a reliable extrapolation of

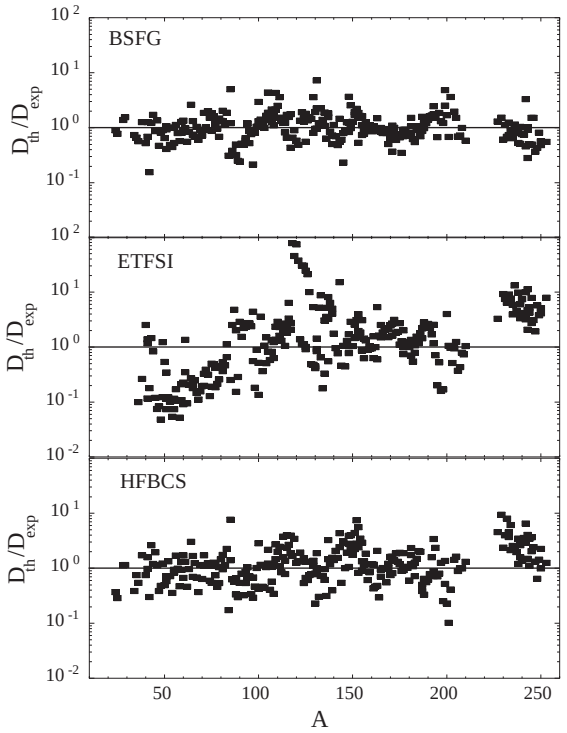

Fig. 15. Comparison between experimental s-wave neutron resonance spacings D_{exp} at the neutron separation energy S_n and predicted values D_{th} derived from the use of the ETFSI [70] (middle panel) or of a HFBCS [71] (lower panel) model. The results from the global BSFG approximation of [58] are also shown (upper panel).

the NLDs at low energies, as seen from a confrontation with available experimental data.[2] In spite of the good aforementioned agreement between the BSFG and HFBCS-based level density predictions when experimental data are available, Fig. 16 shows that large differences may exist between them for nuclei located far from the line of nuclear stability.

3.3.4. Optical potentials

Phenomenological optical potentials (OPs) of the Woods–Saxon type may not be well suited for applications involving exotic nuclei in general, and for the modeling of the p-process in particular. It is considered profitable to use more microscopically-based potentials, whenever possible. A semi-microscopic OP, usually referred to as the JLM potential [72], is available for the description of the nucleon–nucleus case. It is derived from the Brückner–Hartree–Fock approximation based on a Reid's hard core nucleon–nucleon interaction. This OP has been revised recently for nucleons incident on spherical or quasi-spherical nuclei with masses $40 \leqslant A \leqslant 209$ at energies ranging from the 1 keV to 200 MeV [73]. The resulting new version, referred to as the JLM-Bruyères or JLMB

[2] The microscopic HFBCS-based model has been renormalized on experimental neutron resonance spacings and low-lying levels of a variety of nuclei in order to enhance the quality of the predictions concerning the energy dependence of the NLD for these nuclei. This information is needed in various applications.

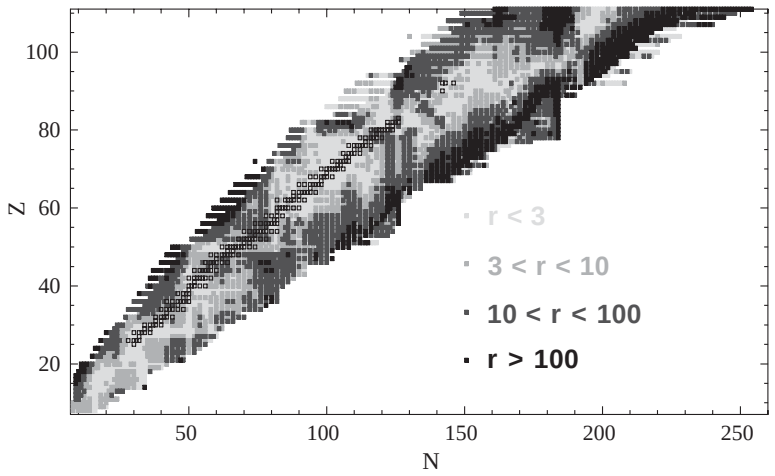

Fig. 16. Comparison between the state densities $\omega(U) = 2\sum_J (2J+1)\rho(U,J)$ at the neutron separation energy $U = S_n$ calculated by the HFBCS and BSFG models already selected in Fig. 15. The factor of 2 in the definition of ω relates to the assumed equal probabilities of both parities π at all energies. The values of r displayed for all nuclides in the ranges N and $Z \geqslant 8$ and $Z \leqslant 110$ located between the proton and neutron drip lines are defined as $r = 10^{|\log(\omega_{\mathrm{HFBCS}}/\omega_{\mathrm{BSFG}})|}$. Its values are coded as indicated in the figure.

potential, features in particular a renormalization to an extensive set of nucleon scattering and reaction data [74]. Even if differences remain in some cases between rates calculated with different OPs, the predictions based on the semi-microscopic potentials referred to above give a global satisfactory agreement with experimental data (see Section 3.4). Some improvements would be most welcome, however, especially in the low-energy domain and in the treatment of deformed or exotic nuclei.

The situation for the α-particle–nucleus OPs is much less satisfactory, and one still has to rely on phenomenological potentials. Most of the proposed OPs are derived from fits to elastic α-nucleus scattering data at energies $E \gtrsim 80$ MeV or, in some cases, to (n,α) cross sections at lower energies (e.g. [76–79] for details). However, the OP, and in particular its imaginary component, is known to be strongly energy dependent at energies below the Coulomb barrier. As a consequence, its extrapolation to sub-Coulomb energies is even more unsecure than in the case of nucleons, as exemplified by the ^{144}Sm(α,γ)^{148}Gd case (Section 3.4). The development of a global α-nucleus OP to describe scattering and reaction cross sections at energies $E \lesssim 20$ MeV of better relevance to astrophysics has been attempted adopting a Woods–Saxon [80] or a double folding (DF) [31,51] component of the real part. In both cases, a phenomenological form of the imaginary OP and of its energy dependence is adopted. More specifically, [51] base their DF model for the real part of the OP on a realistic nucleon-nucleon interaction. From this, three different types of imaginary potentials are constructed from the assumption of volume or surface absorption, or from the adoption of the so-called dispersion relations that link the real and imaginary parts of the OP. The three corresponding OPs are constrained in order to reproduce at best scattering and reaction data. In the case of the OP with a purely volume imaginary term (OP I of [51]), this is done through the fitting of nineteen free parameters. This number is decreased to ten in the case of a volume plus surface imaginary potential (OP II of [51]), with a concomitant reduction of the ambiguities in deriving the OP from the data. This is even better achieved by using the dispersive relation (OP III of [51]).

The three global α-nucleus OPs derived in such a way are able to reproduce the bulk of the existing experimental data at sub-Coulomb energies [51], as shown for (α,γ) cross sections in Section 3.4 (see in particular Fig. 19). Experimental data are scarce, however, particularly in the $A > 100$ mass range. This limits dramatically the predictive power of any of the OPs referred to above, especially in view of their high impact on cross section estimates. At the energies of astrophysical relevance, these are found to vary in some cases by more than one order of magnitude just as a result of a different choice among the potentials constructed by [80,51]. In fact, ^{144}Sm(α,γ)^{148}Gd provides a remarkable test case of prime interest for the p-process (Section 9.3). Its analysis demonstrates that the energy dependence of the imaginary component of the OP for this reaction must be assumed to follow a Fermi-type function instead of the conventional Brown–Rho parametrization [81] (see Section 3.4 and Fig. 20). Clearly, additional experimental data extending over a wide mass range, and especially low-energy radiative captures by $A \approx 100$–200 nuclei, are of paramount importance to further constrain the construction and enhance the reliability of global low-energy α-particle–nucleus OPs. This dedicated experimental effort has to be complemented with further theoretical work. Much indeed remains to be done in this field.

3.3.5. γ-ray strength function

As reminded in Section 3.3.1, the total photon transmission coefficient appearing in Eq. (2) when it is applied to radiative captures is dominated by the $E1$ transitions. The calculation of the $E1$-strength function necessitates the knowledge of the low-energy tail of the GDR of the compound system formed in the reaction process. The photon transmission coefficient is most frequently described in the framework of the phenomenological generalized Lorentzian model [82–84]. In this approximation,

$$T_{E1}(\varepsilon_\gamma) = \frac{8}{3}\frac{NZ}{A}\frac{e^2}{\hbar c}\frac{1+\chi}{mc^2}\frac{\varepsilon_\gamma^4 \Gamma_{\mathrm{GDR}}(\varepsilon_\gamma)\varepsilon_\gamma^4}{(\varepsilon_\gamma^2 - E_{\mathrm{GDR}}^2)^2 + \Gamma_{\mathrm{GDR}}^2(\varepsilon_\gamma)\varepsilon_\gamma^2}\ , \tag{8}$$

where E_{GDR} and Γ_{GDR} are the energy and width of the GDR, m is the nucleon mass and $\chi \simeq 0.2$ is an exchange-force contribution to the dipole sum rule. This model is even the only one used for practical applications, and more specifically when global predictions are requested for large sets of nuclei.

The Lorentzian GDR approach suffers, however, from shortcomings of various sorts. On the one hand, it is unable to predict the enhancement of the $E1$ strength at energies below the neutron separation energy demonstrated by nuclear resonance fluorescence experiments. This departure from a Lorentzian profile may manifest itself in various ways, and especially in the form of a so-called pygmy $E1$ resonance [85,86] which is observed in *fp*-shell nuclei, as well as in heavy spherical nuclei near closed shells (Zr, Mo, Ba, Ce, Sn, Sm and Pb). Another illustration (see Fig. 21) is provided by recent experiments on ^{181}Ta(γ,n)^{180}Ta. On the other hand, even if a Lorentzian function provides a suitable representation of the $E1$ strength, the location of its maximum and its width remain to be predicted from some underlying model for each nucleus. For astrophysical applications, these properties have often been obtained from a droplet-type of model [87]. This approach clearly lacks reliability when dealing with exotic nuclei.

In view of this situation, combined with the fact that the GDR properties and low-energy resonances may influence substantially the predictions of radiative capture cross sections, it is clearly of substantial interest to develop models of the microscopic type which are hoped to provide a reasonable reliability and predictive power for the $E1$-strength function. Attempts in this direction have been conducted within models like the thermodynamic pole approach [68], the theory of

finite Fermi systems or the QRPA approximation [88]. The spherical QRPA model making use of a realistic Skyrme interaction has even been used recently for *large-scale* derivations of the $E1$-strength function [89]. This global calculation predicts the location of the GDR in close agreement with experimental data, the rms deviation of the predictions from measurements for 84 nuclides amounting to about 300 keV only. The QRPA $E1$-strength functions also reproduce satisfactorily the average resonance capture data at low energies [83]. The aforementioned QRPA calculations have been performed for all the $8 \leqslant Z \leqslant 110$ nuclei lying between the two drip lines. In the neutron-deficient region of most direct interest for the p-process, as well as along the valley of β-stability, the QRPA distributions are very close to a Lorentzian profile. However, cases where some extra strength is present at low energies are known to exist, and can be predicted by microscopic models only, as illustrated below (Section 3.4; Fig. 21).

Significant departures from a Lorentzian are found for neutron-rich nuclei. In particular, RPA calculations [89,90] show that the neutron excess affects the spreading of the isovector dipole strength, as well as the centroid of the strength function. The energy shift is found to be larger than predicted by the usual $A^{-1/6}$ or $A^{-1/3}$ dependence given by the phenomenological liquid drop approximations [87]. In addition, some extra strength is predicted to be located at sub-GDR energies, and to increase with the neutron excess. Even if it represents only about a few percent of the total $E1$ strength, it can produce an increase by up to an order of magnitude of the rates of radiative captures by some exotic neutron-rich nuclei [89]. These reactions play no role in the p-process except, to some extent at least, in the case of exploding sub-Chandrasekhar white dwarf stars (Section 8.3).

3.4. A confrontation between measured and calculated reaction rates

In order to evaluate the overall quality of the reaction rate predictions, this section presents a confrontation between selected experimental data and calculations based on Eqs. (4) and (6) in which just the ground state contribution ($\mu = 0$) is taken into account, the consideration of target excited states being irrelevant in the laboratory conditions. For astrophysical applications, such calculations have been performed with the help of a computer code referred to as MOST [91]. Although many other statistical model codes have been developed (e.g. those known as Talys [92], Empire [93] or Non-Smoker [94]), MOST represents the only effort to derive all nuclear inputs from global microscopic models, a feature of particular importance as explained in Section 3.3.1.

In addition, MOST calculates Eqs. (4) and (6) with the provision that various sets of models predicting the necessary nuclear input can be selected. In the following, the MOST calculations are conducted with 14 different combinations of the global models describing the ground-state properties [63,67], nuclear level density [68,71,94], nucleon- and α-optical potentials [75,72,73,77,80,51] and γ-ray strength [82,84,89]. These combinations are defined in Table 2. Some of them are made of purely microscopic nuclear ingredients. This is the case in particular for Set 1, which leads to what is referred to in the following as the 'standard' (ST MOST) rates. In contrast, Set 2 is made of phenomenological-type models only. Set 10 includes the same inputs as the ones adopted in the compilation by [94] (note that the α-particle OP of [77] is almost identical to the one constructed by [76]), so that the predictions reported there are in fact included in the rate uncertainties discussed below.

Let us first turn to radiative nucleon capture reactions. Fig. 17 compares the MOST predictions of the Maxwellian-averaged (n,γ) rates $\langle \sigma v \rangle$ at $T = 3.5 \times 10^8$ K with experimental data for some 228 nuclei heavier than ^{40}Ca included in the compilation of [28]. It appears that the calculations agree

Table 2
Combinations of nuclear ingredients used in the statistical model reaction rate calculations using the computer code MOST

Set	Ground-state	NLD	Nucleon OMP	α OMP	$E1$ strength
1	HFB-2 [67]	HFBCS [71]	JLMB [73]	OPIII of [51]	QRPA [89]
2	FRDM [63]	BSFG [58]	Woods-Saxon [75]	Woods-Saxon [77]	Lorentzian [84]
3	HFB-2 [67]	HFBCS [71]	JLMB [73]	Woods-Saxon [80]	Lorentzian [84]
4	HFB-2 [67]	BSFG [58]	JLMB [73]	OPIII of [51]	QRPA [89]
5	HFB-2 [67]	HFBCS [71]	JLM [72]	OPIII of [51]	QRPA [89]
6	FRDM [63]	HFBCS [71]	JLMB [73]	OPIII of [51]	QRPA [89]
7	HFB-2 [67]	HFBCS [71]	JLMB [73]	Woods-Saxon [77]	QRPA [89]
8	HFB-2 [67]	HFBCS [71]	JLMB [73]	OPI of [51]	Lorentzian [84]
9	HFB-2 [67]	HFBCS [71]	JLMB [73]	OPII of [51]	Lorentzian [84]
10	FRDM [63]	BSFG [94]	JLM [72]	Woods-Saxon [77]	Lorentzian [82]
11	HFB-2 [67]	HFBCS [71]	JLM [72]	Woods-Saxon [77]	Lorentzian [82]
12	HFB-2 [67]	BSFG [58]	Woods-Saxon [75]	OPII of [51]	Lorentzian [84]
13	HFB-2 [67]	HFBCS [71]	JLMB [73]	OPIII of [51]	Lorentzian [84]
14	HFB-2 [67]	HFBCS [71]	JLMB [73]	Woods-Saxon [80]	Lorentzian [84]

Combination 1 provides the ‘standard’ (ST) rates.

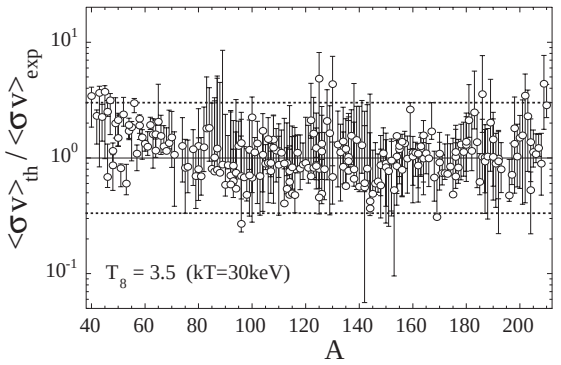

Fig. 17. Comparison of MOST Maxwellian-averaged (n,γ) rates $\langle\sigma v\rangle_{\rm th}$ with experimental values [28] at $T = 3.5 \times 10^8$ K. The open dots correspond to the ‘standard’ (ST) rates (from Set 1 of Table 2). The vertical bars define the variations in the values of the displayed ratios when the 13 other combinations of nuclear ingredients defined in Table 2 are used for the MOST calculations.

with all data to within a factor of 3. Fig. 18 compares the experimental cross sections for some of the low-energy (p,γ) reactions reported in Fig. 12 with MOST calculations performed with Sets 1 and 5 of Table 2 selected in particular for illustrating the sensitivity of the rate predictions to the nucleon–nucleus OP. Again, the MOST predictions are in nice agreement with the vast majority of the (p,γ) data. This comparison is limited, however, to targets up to Sn. Experiments with heavier nuclei would be most welcome, as they might help refining the predictions.

The situation is by far less clear for the (α,γ) reactions. This results from the lack of a large enough body of experimental data for sub-Coulomb cross sections (Section 3.2) combined with the difficulties to construct global and reliable α-nucleus OPs (Section 3.3.4). These theoretical problems are magnified by the fact that, at the sub-Coulomb energies of astrophysical relevance, the

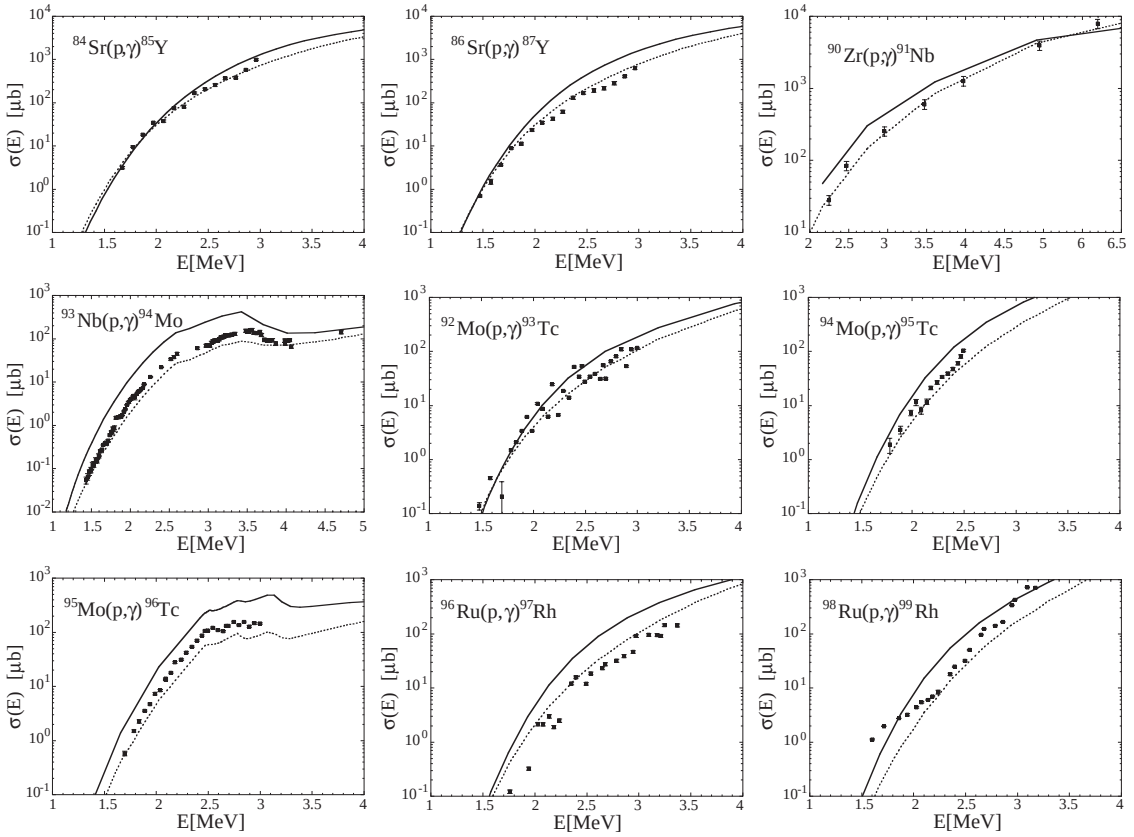

Fig. 18. Comparison between measured cross sections of some (p,γ) reactions selected among those reported in Fig. 12 (black symbols) and the MOST predictions derived from Sets 1 (ST MOST; solid lines) and 5 (dotted lines) of Table 2.

reaction rate predictions are highly sensitive to these potentials through the corresponding α-particle transmission coefficients. Fig. 19 displays a comparison between some low-energy measurements of (α,γ) cross sections and MOST predictions. The quality of the agreement appears to vary from case to case. Uncertainties in the calculated values originating from those in the NLDs and α-nucleus OPs are also displayed. They are seen to be uncomfortably large in some cases. As already emphasized in Section 3.3.4, more experiments on low-energy radiative α-captures by $A \approx 100$–200 targets would be extremely helpful in order to construct better and more reliable α-nucleus OPs suited for sub-Coulomb energies.

The reaction ^{144}Sm(α,γ)^{148}Gd is of special astrophysics interest (Section 9.3). It also illustrates quite vividly the difficulties to reliably predict low-energy (α,γ) cross sections. It is thus worth to discuss the case in some more detail. Fig. 20 displays the experimental astrophysical S-factor for this reaction obtained by [50] (black dots). This quantity is classically defined from the reaction cross section σ at the relative energy E by $\sigma(E) = S(E)/E \exp[-Z(\alpha)Z(^{144}\mathrm{Sm})e^2/(\hbar v)]$, where $Z(i)e$ is the charge of nucleus i and v is the relative velocity corresponding to energy E. Hauser–Feshbach predictions are also shown, and are seen to diverge widely at low energy, and especially close to the energies $E \approx 9$–10 MeV of relevance for ^{144}Sm(α,γ)^{148}Gd in p-process conditions (i.e. the so-called

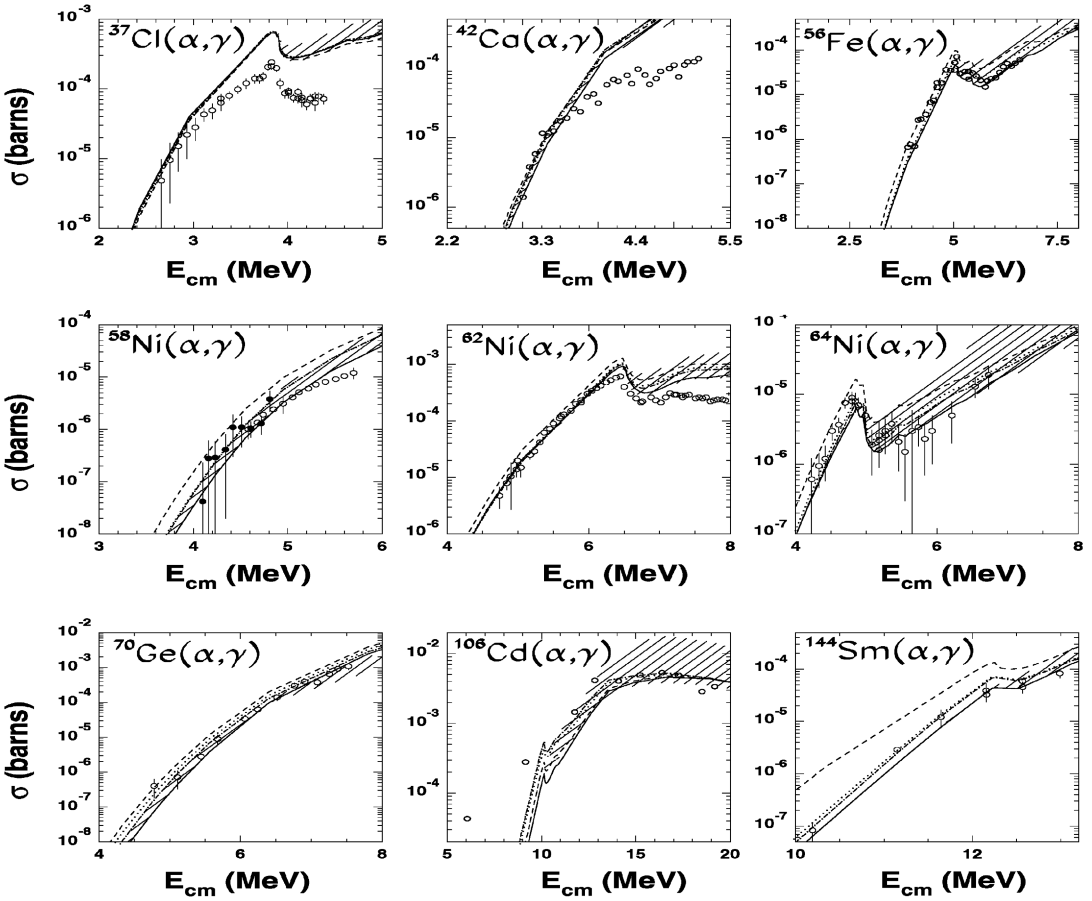

Fig. 19. Cross sections for the (α,γ) reactions on ^{37}Cl [95], ^{42}Ca [96], ^{56}Fe [97], ^{58}Ni [98], ^{62,64}Ni [95], ^{70}Ge [47], ^{106}Cd [99] and ^{144}Sm [50] (see also Fig. 20 for more details about the latter reaction). Black and open circles represent experimental data. The dotted, dot-dashed and solid lines give the MOST predictions obtained with the three global α-nucleus potentials I, II and III of [51]. The shaded areas give a measure of the uncertainties due to those in the nucleon-nucleus OPs and NLD's. The results obtained with the Woods–Saxon α-nucleus OP of [77] are represented by dashed lines (from [51]).

'Gamow energy' for this reaction). Even the global energy trend of S at the lowest energies is not the same in all calculations. These marked differences are due to the use of different α-nucleus OPs. The potential of [77] is a global one of phenomenological nature. In contrast, the potential of [100] is specifically deviced in order to fit a low energy ($E_{\rm lab} = 20$ MeV) $^{144}\mathrm{Sm} + \alpha$ scattering experiment, but is unable to reproduce the reaction data at energies $E_{\rm cm} \lesssim 11.5$ MeV. This failure is in fact very revealing of the limited reliability of the constructed α-particle OPs at low energies. The potential of [100] has indeed been tailored at a time when the $E_{\rm cm} \lesssim 11.5$ MeV data were still missing! In fact, tests conducted with the code MOST demonstrate that the remarkable experimental energy trend of the S-factor can be reproduced with a strongly energy-dependent α-nucleus OP at the lowest energies reached so far in the laboratory. The OP real and imaginary parts are constructed under the constraint of reproducing at best experimental low-energy scattering and reaction data concerning

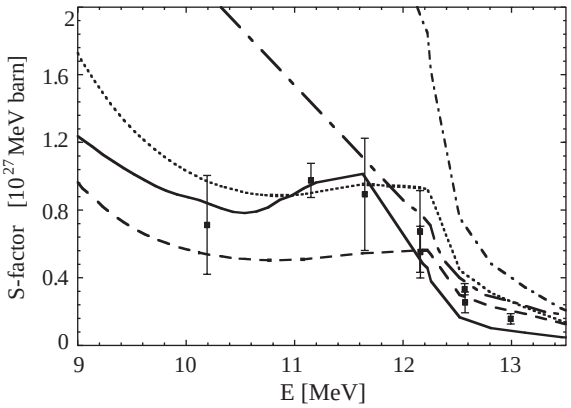

Fig. 20. The astrophysical S-factor for ^{144}Sm(α,γ)^{148}Gd. Measured values [50] are represented by black squares. The theoretical values are derived from the code MOST with the selection of different global α-nucleus potentials: OPI (dotted line) and OPIII (dashed line) from [51], OP from [50] (solid line), OP from [100] (long dashed-dot line), and OP from [77].

the α-^{144}Sm interaction, as described in detail in [50]. The resulting rate calculations fit nicely the measurements, even at the lowest energies, as shown in Fig. 20. The major drawback of this OP is its specificity to the ^{144}Sm(α,γ)^{148}Gd reaction, or, in other words, its lack of any global character. The three global potentials of [51] attempt to cure this shortcoming by imposing constraints not only from ^{144}Sm(α,γ)^{148}Gd, but also from other available data (Fig. 19). As shown in Figs. 19 and 20, they all reproduce well the (α,γ) data. The three potentials are also able to reproduce satisfactorily the bulk of experimental data on (α,n), (α,p) and (n,α) reactions, as well as the existing elastic scattering data at energies of relevance to astrophysical applications [51]. However, when considering reaction rates on experimentally unexplored targets, deviations up to a factor of 10 are found (Section 3.5). These uncertainties can be regarded today as typical of the level of confidence one is able to reach today in the global prediction of low-energy α-induced reaction cross sections.

Finally, the MOST predictions are confronted with direct (γ,n) cross section measurements. Fig. 21 compares the experimental data for ^{181}Ta(γ,n)^{180}Ta of special astrophysical interest (Section 6.3) with the predictions derived from the Lorentzian [84] and QRPA [89] prescriptions for the $E1$-strength functions. The two predictions differ most markedly at energies close to the neutron threshold. The phenomenological Lorentzian model predicts a too precipitous drop of the cross section with decreasing energies when approaching the neutron threshold. Clearly, the observed relative enhancement of the cross section at these energies cannot be accounted for by Eq. (8). This shortcoming is avoided by the QRPA model which is based on a microscopic description of the single-particle and collective excitations. It predicts an extra strength for $E \approx 8$–10 MeV which nicely agrees with the experimental data.

Table 3 confronts MOST calculations with laboratory (γ,n) rates at $T = 2.5 \times 10^9$ K measured by the bremsstrahlung technique described in Section 3.1. The photoneutron rates are seen to be predicted within a factor of about 2, which is an accuracy similar to the one reached by the predictions of the reverse radiative capture data. The lowest values are obtained with the Lorentzian-type $E1$-strength function [84,82], while the largest values with respect to the ST rates are found when using the QRPA $E1$ strength and the BSFG prescription for the NLD (Sections 3.3.3 and 3.3.5).

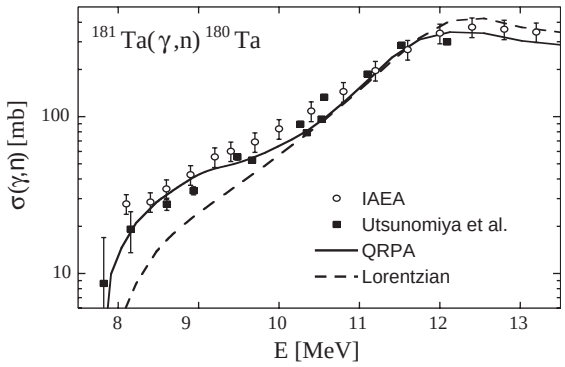

Fig. 21. Comparison between the experimental photoneutron cross sections for ^{181}Ta(γ,n)^{180}Ta [30,35] with the HF predictions based on the QRPA [89] (solid line) and Lorentzian-type [84] descriptions of the $E1$-strength function.

Table 3
Comparison of experimental (γ,n) rates [101] at a temperature $T = 2.5 \times 10^9$ K with standard ST MOST calculations (Set 1 of Table 2)

Target	Exp	ST MOST	Min	Max
^{190}Pt	0.65 ± 0.33	0.29	0.11	0.48
^{192}Pt	0.43 ± 0.13	0.56	0.20	1.27
^{198}Pt	72.7 ± 16.5	106.8	34.4	127.5
^{198}Au	5.82 ± 0.75	5.60	2.73	9.12
^{196}Hg	0.40 ± 0.07	0.58	0.20	0.75
^{198}Hg	1.98 ± 0.31	2.07	0.77	3.00
^{204}Hg	58.5 ± 7.8	165.5	46.7	192.2
^{204}Pb	1.56 ± 0.25	3.02	0.98	3.83
^{186}W	314 ± 44	245.4	113.4	276.0

As in Fig. 11, it is assumed that $\sigma_{(\gamma,n)}(E) = \sigma_0 \sqrt{(E - E_{\rm thr})/E_{\rm thr}}$ near the reaction threshold $E_{\rm thr}$, σ_0 being determined by the bremstrahlung experiments (Section 3.1). The maximum and minimum theoretical rates are obtained by considering the remaining 13 Sets of Table 2.

3.5. Rate prediction uncertainties evaluated from the use of different sets of nuclear inputs

In the comparison between experimental reaction data and calculations (Section 3.4), the impact of changes in the predicted nuclear quantities (ground-state properties, nuclear level density, nucleon- and α-optical potentials, γ-ray strength) entering the computation of Eqs. (2)–(4) has already been evaluated. It is worth extending this analysis to a larger set of reactions, especially those involving unstable targets for which no experimental data are available. For this purpose, the 14 sets of models defined in Table 2 are used again as inputs to the code MOST. Fig. 22 illustrates in the (N,Z)-plane the maximum variations predicted at a temperature of 2.5×10^9 K between the 14 corresponding rates computed for each of the considered radiative neutron-, proton- and α-captures. As far as (n,γ) reactions are concerned, discrepancies are found principally for neutron-rich nuclei. They mainly result from different predictions of ground state masses and NLDs. In contrast, variations by less

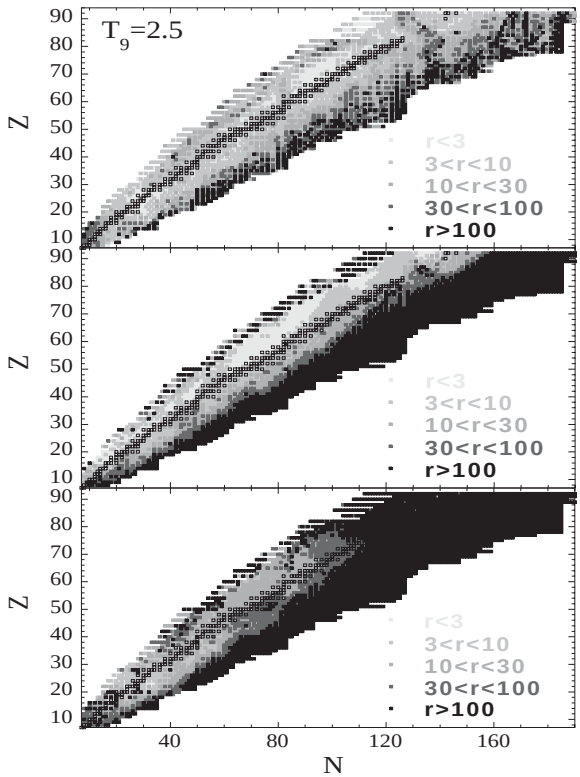

Fig. 22. Representation in the (N,Z)-plane of the ratio r between the maximum and minimum rates for individual neutron (upper), proton (middle) and α (lower panel) radiative captures obtained when the 14 different sets of nuclear ingredients defined in Table 2 are used in the code MOST. The different codings correspond to different r ranges. The adopted temperature is $T_9 = 2.5$ ($T = T_9 \times 10^9$ K).

than a factor of 10 are found on the proton-rich side. The situation for (p,γ) reactions deteriorates even for nuclei lying along the valley of stability, although the proton captures on proton-rich nuclei span a range of values not exceeding a factor of 10. The most unreliable predictions clearly concern (α,γ) reactions. In this case, deviations due to different α-nucleus OPs amounting to factors up to 100 are found along the valley of β-stability, as well as on the neutron-deficient side of interest for the p-process. Of course, the situation for the radiative captures translates directly into the one for the photodisintegrations when the reciprocity theorem is used (Eq. (5)), being even worsened when experimental masses are not available.

3.6. The nuclear reaction network used in the p-process modeling

The detailed modeling of the transformation of s- or r-nuclides into p-species requires the handling of extended reaction networks involving typically more than 2000 nuclides in a large mass range (from well below to well above the iron peak) linked by more than 20 000 reactions. In some scenarios (e.g. Section 8.3), this already large network has even to be supplemented with many other

nuclear species (up to 4000) and reactions (up to 50 000). The considered reactions comprise neutron, proton and α-particle captures and the reverse transformations, including photodisintegrations. The 'special' 3α reaction, as well the various $^{12}C + {}^{12}C$, $^{12}C + {}^{16}O$ and $^{16}O + {}^{16}O$ channels are also included. The nuclear reactions are complemented with all possible $\beta^{\pm}$-decays and electron captures. The build-up of these networks clearly requires the input of an impressive amount of data about the nuclear quantities discussed above in this section. As already emphasized before, it is obvious that the vast majority of these data have to be provided by theory, especially as only very few of the considered nuclei are located in the close vicinity of the bottom of the valley of nuclear stability.

Unless otherwise specified, the abundance calculations to be reported below rely on a reaction network constructed with the help of the 'Network Generator' referred to as NETGEN, and described in [102]. NETGEN also provides details about the sources of the selected reaction rates. Routinely, the rates of the reactions on targets up to Si are the values referred to as 'adopted' in the NACRE reaction rate compilation [103]. For heavier targets, use is made of the standard ST MOST rates defined in Section 3.4 (see Set 1 of Table 2). In several instances, abundance calculations are also performed with the rates derived from the 13 other combinations of nuclear input defined in Table 2 in order to provide a measure of the impact of the rate uncertainties on the p-nuclide abundance predictions. The MOST rates are superseded, whenever possible, by experimentally-based neutron [28] and charged-particle capture rates (references and details are available in the Brussels Nuclear Astrophysics Library [102]). We will have to report below on some p-process calculations based on different networks and reaction rates. These cases correspond to computations performed before the NACRE and/or MOST rates became available, and which have not been updated yet, or to modelings originating from other research teams than the one to which the authors of this review belong.

4. Massive stars: the pre-Type II supernova production of the p-nuclides

4.1. Some pedestrian considerations about the evolution of massive stars leading to Type II supernovae

For readers who are not familiar with the stellar astrophysics which will have to be dealt with below, we first present a very brief and rough sketch of the evolution of those stars with initial masses $M \gtrsim 10\ M_{\odot}$, generally referred to as 'massive' stars, which are thought to lead to explosions known as Type II supernovae (SNII).

The evolution of single stars of this sort with different initial masses or compositions and the concomitant nucleosynthesis have been the subject of much computation, at least in one dimensional spherically symmetric cases [104–108], and in absence of rotation. In this relatively simple situation, and as pictured very schematically in Fig. 23, the evolution of the central regions of a massive star is made of successive 'controlled' thermonuclear burning stages and of phases of gravitational contraction. The latter phases are responsible for a temperature increase, while the former ones produce nuclear energy through charged-particle induced reactions. Of course, composition changes also result from these very same reactions, as well as, at some stages at least, from reactions which in contrast do not play any significant role in the stellar energy budget. Fig. 23 illustrates that the nuclear burning phases involve nuclear fuels of increasing charge number Z and take place at temperatures

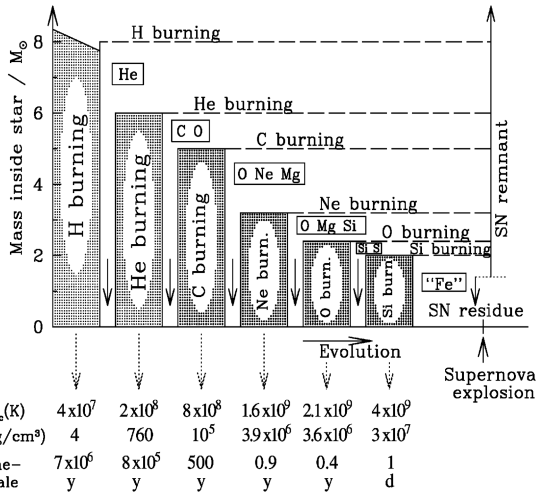

Fig. 23. Schematic representation of the evolution of the internal structure of a spherically-symmetric massive ($M \approx 25\ M_{\odot}$) star. The shaded zones correspond to nuclear burning stages. A given burning phase starts in the central regions and then migrates into thin peripheral burning shells. Typical central temperatures T_c, central densities ρ_c and durations of the core burning phases are indicated at the bottom of the figure (adapted from [109]). In between the central nuclear burning phases are episodes of gravitational contraction (downward arrows). The chemical symbols represent the most abundant nuclear species left after each nuclear-burning mode ("Fe" symbolizes the iron-peak nuclei with $50 \lesssim A \lesssim 60$). If the star explodes as a SNII, the most central parts may leave a 'residue', while the rest of the stellar material is ejected into the ISM, where it is observed as a supernova 'remnant'.

increasing from several tens of 10^6 K to about 4×10^9 K. Concomitantly the duration of the successive nuclear-burning phases decreases in a dramatic way. This situation results from the combination of (i) a decreasing energy production when going from H burning to the later burning stages, and (ii) an increasing neutrino production and concomitant energy losses for temperatures exceeding about 5×10^8 K (see [104, Chapter 10]). Fig. 23 also depicts schematically that a nuclear burning phase, once completed in the central regions, migrates into a thin peripheral shell. As a consequence the deep stellar regions look like an onion with various "skins" of different compositions.

It has to be stressed that the true stellar structure is certainly not as simple as the one sketched in Fig. 23 (cf. Figs. 10.5-6 of [104]), especially in the presence, but even in the absence of departures from spherical symmetry. These additional complexities may arise e.g. from the, even approximate, consideration of rotation [110]. They culminate when multi-dimensional simulations are attempted [111,112]. Let us also emphasize that steady mass loss from a star may also affect its structure and evolution in various ways. Stellar evolution computations currently treat this effect in an approximate way through the use of simple phenomenological mass loss rate formulae [113–115].

The various nuclear burning phases depicted in Fig. 23 lead to the formation of an iron core the fate of which is, in certain cases at least, a catastrophic explosion referred to as a 'core collapse supernova (CCSN)' event. When the exploding star exhibits H-lines in its spectrum at maximum light, as it is expected when the star as retained its H-envelope up to the time of the explosion (as depicted in Fig. 23), it is classified as a Type II supernova (SNII). In contrast, if stellar winds have been strong enough to peel off the H envelope before the explosion, so that the star spectrum

is devoid of H lines, the CCSN is classified as a TypeIb/Ic supernova (SNIb/c). The p-process in SNII is discussed in Sections 5 and 6, while Section 8.2 deals with the SNIb/c. In all cases, the nucleosynthesis calculations are conducted in the framework of 'canonical' spherically symmetric CCSN with kinetic energies of the order of 10^{51} ergs. Some CCSN events may depart from this canonical situation either through their asphericity, for which observational as well as theoretical evidence is accumulating, or through their energetics, their kinetic energy exceeding or being lower than the canonical value. These outliers, referred to as 'hypernovae' (some of which being considered as likely progenitors of at least some subclass of gamma-ray bursts) or 'faint SN', respectively, are considered to be associated with the explosion of $M \gtrsim 20$–$25\ M_\odot$ (e.g. [116]). No information is available to-date on the p-process in such objects.

4.2. The seeds for the p-process

As recalled in Section 1, the thermonuclear production of the p-nuclides is considered to result from the transformation of pre-existing s- or r-nuclides by an ensemble of photodisintegrations of the (γ,n), (γ,p) or (γ,α) types, possibly complemented with nucleon captures. It may be imagined that these seed species are just inherited from the ISM by the stars at their birth. An obvious alternative is their in-situ production in stellar layers where the p-process will eventually develop. Several of the zones identified in Fig. 23 can indeed be proper sites for the development of the s-process. One of the zones of special interest in this respect is the He-burning core, where the s-process is triggered mainly by the ^{22}Ne(α,n)^{25}Mg neutron source, ^{22}Ne resulting from the transformation at the beginning of He burning of the ^{14}N synthesized by the CNO cycles.

Fig. 24 shows typical abundance distributions produced by the s-process developing during the core He-burning of a massive ($25\ M_\odot$) star with $Z = Z_\odot$ and $Z = 0.1\ Z_\odot$. As is well-known (e.g. [121]), these distributions depend on the relative abundances of (i) the neutrons produced by ^{22}Ne(α,n)^{25}Mg, (ii) the iron peak and trans-iron nuclides present initially in the He core (the s-process seeds), and

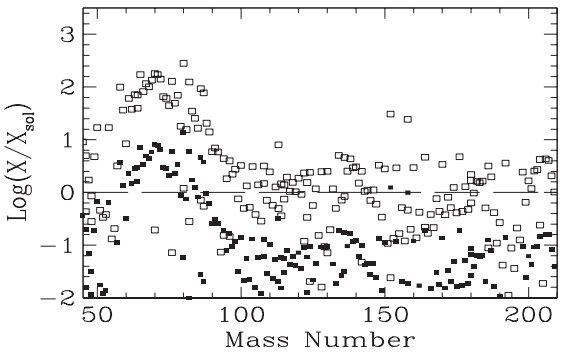

Fig. 24. Abundances of the s-nuclides at the termination of He burning in the core of a $25\ M_\odot$ star with $Z = Z_\odot$ (open squares) and with $Z = 0.1\ Z_\odot$ (black squares). They are based on the stellar models of [117,118] and on the rates of [119] for charged-particle captures and on the compilation by [120] for neutron captures. In the $Z = 0.1\ Z_\odot$ case, the initial mass fractions of the nuclides with mass numbers $20 \leqslant A \leqslant 30$ and $A > 30$ (including Fe) are scaled as $X(Z) = (Z/Z_\odot)X(Z_\odot)$ and $X(Z) = (Z/Z_\odot)^{1.42}X(Z_\odot)$ respectively. The Fe/O ratio is assumed to vary with O/H as [Fe/O] = 0.42 [O/H] (see [121] for a discussion of the choice of the initial abundances).

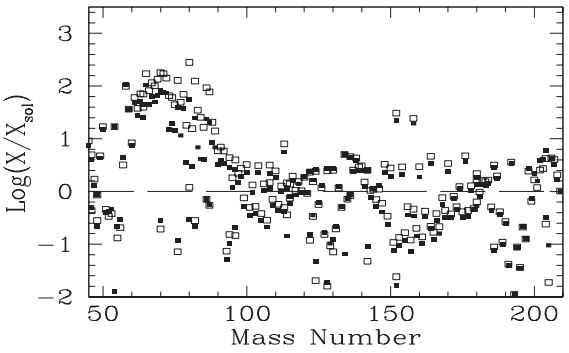

Fig. 25. Same as Fig. 24, but for the $Z = Z_{\odot}25\ M_{\odot}$ star with two different nuclear inputs. The data represented by open squares are obtained with the charged-particle capture rates from [119] and are identical to those displayed in Fig. 24. The black squares correspond to the selection of the recommended NACRE rates. In both cases, the neutron capture rates are taken from [120] (from M. Rayet, private communication).

(iii) the lighter nuclides generally referred to as 'neutron poisons', as they capture neutrons that are consequently lost for the s-nuclide production. The s-nuclide abundances displayed in Fig. 24 exhibit the classical feature of a substantial enhancement (with respect to the initial composition) of the s-nuclides that is limited to the $A \lesssim 90$ mass region, irrespective of the metallicity. The precise levels of enhancement of specific nuclides or subsets of nuclides is less well established, however. These uncertainties arise from various sources, like the intricate question of the s-process seeds to poison abundance ratio, its evolution with metallicity in the Galaxy being far from trivial. This concerns in particular Fe/O, the importance of oxygen as a neutron poison increasing with decreasing metallicity. Problems remain also at the stellar level, as e.g. the impact on the s-process efficiency of the description of the boundaries of the He-burning core (e.g. mixing with the overlying layers, not talking about rotational effects). Finally, nuclear physics brings its share of uncertainties, even if substantial progress has been made recently in the knowledge of the stellar rates of some key reactions, and in particular of $^{22}Ne(\alpha,n)^{25}Mg$ (see Section 6.1). Some of these problems are discussed in detail by [121]. Fig. 25 just illustrates the s-abundance changes implied by two different choices of the rates of charged particle captures by targets up to Si, the neutron capture rates being kept unchanged. The corresponding largest changes concern the abundantly produced $70 \leqslant A \leqslant 90$ s-nuclides.

4.3. Some comments on the non-explosive p-process in massive stars

For long, it has been considered [1,10] that the most likely site for these transmutations to operate is the outer H-rich region of massive stars at their SNII stage (see Fig. 23). This scenario has been challenged by [11,12] on grounds of the implausibility to reach in the envisioned spherically symmetric H-rich supernova envelopes the temperatures in excess of 10^9 K required for an efficient operation of photodisintegrations or proton captures (it remains to be seen if this situation might be different in aspherical jet-driven SNII; for models of this type, see e.g. [123]). Instead, it has been proposed to locate the p-process in the deep O–Ne-rich layers of massive stars either at their pre-supernova or SNII phases (see Fig. 23).

The early examination by [11,12] of the pre-explosion production of the p-nuclides in massive stars was making use of approximations to relatively low-quality models for the late evolution of massive stars available at the time. A full nuclear reaction network was adopted, including neutron, proton and α-emitting photodisintegrations, as well as neutron and proton captures. The rates of these reactions were predicted from an approximation of the Hauser–Feshbach statistical model.

In spite of the very preliminary nature of this exploration, it already put forth the potentialities of the scenario of pre-explosive p-processing in the O–Ne shells of massive stars. It also identified some features that are largely shared by the more recent thermonuclear models to be described below. In particular, a superposition of astrophysical conditions (temperatures,...) appeared mandatory in order to have a chance of reproducing the solar abundance distribution of the p-nuclides (Fig. 3). It also identified a series of p-species the predicted underproduction of which (with respect to solar) was confirmed by subsequent models. The pre-explosion production of the p-nuclides in massive stars has been revisited on grounds of more realistic models and of more reliable nuclear physics input than considered initially. In particular, evaluations have been made in the framework of the models of [117,118,122], as well as by [124] for $15 \leqslant M \leqslant 25\ \mathrm{M}_{\odot}$ stars with solar metallicity $\mathrm{Z}_{\odot}$. The situation has also been explored for very massive stars, as described in Section 7.

Many nuclear physics and astrophysics problems hamper the reliability of the predicted pre-SN p-nuclide production. Among others let us cite the pre-p-process production of the s-nuclides which serve as seeds for the p-nuclides (Section 4.2). Another severe and most difficult question concerns the proper description of the mechanisms of transport of material ('convection') in the stellar layers of relevance to the pre-SN p-process. This description affects drastically the abundance predictions, which is an unfortunate situation in view of the very unsatisfactory state of affairs concerning the convection algorithms adopted in classical one-dimensional model stars. Clearly, a necessary condition for improving substantially the present situation in this respect is to grapple with multi-dimensional star simulations (see below). In fact, the description of the convective properties of the pre-SN O–Ne-rich layers also affects deeply the extent to which p-nuclides produced before the SN event eventually survive the explosion. As an illustration, the evaluations by [122] based on the models of [117,118] lead to the conclusion that most of the pre-SN p-nuclides are destroyed during the explosion because of their concentration in layers that become too hot during the SN shock passage. In contrast, [124] find some survival of the pre-SN p-nuclides, its extent depending quite drastically, however, upon the stellar mass.

An exciting prospect concerning the pre-SN production of the p-nuclides in the O–Ne-rich zones is put forth by recent two-dimensional (2D) hydrodynamic simulations of the convective O-rich shell in massive stars which reveal a number of mixing phenomena that cannot be simulated by the standard mixing length theory used in 1D stellar models [125,126]. In particular, extra convective mixing induced by gravity waves is found to develop in formally stable regions above and below the O-rich layers, providing special C-, O- and Ne-rich blends. A 1D model has been developed [127] in order to simulate the properties of 2D individual convective fluid elements. Such a model estimates the changes in the thermodynamic properties of these elements due to internal energy changes resulting from nuclear burning, neutrino cooling and radiation, as they move across a 1D static O-shell background. The 1D model has been applied to estimate the temporal density and temperature trajectories resulting from an initial particle density perturbation of $|\delta\rho/\rho| = 5\%$, as suggested by the 2 to 7% range predicted by the 2D simulations of [125]. Fig. 26 illustrates the temperature variations experienced by a particle moving adiabatically close to the Si core and by

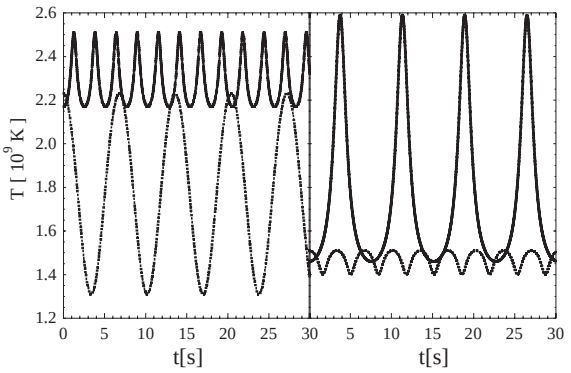

Fig. 26. Temperature profile in two of the periodic orbits calculated by [127]. The solid and dashed lines are obtained for initial overdensities of +5% and −5%. The left panel corresponds to a particle close to the Si core at a background temperature of about 2.2×10^9 K, and the right panel to a particle closer to the C shell at 1.5×10^9 K.

one neighboring the C-rich shell of a 20 $M_\odot$ star with $Z = Z_\odot$ when $\delta\rho/\rho = \pm 5\%$. The displayed thermal histories differ significantly from the constant temperature case corresponding to $\delta\rho/\rho = 0$. The temperature increases and decreases are of course associated with downward and upward movements, and imply variable rates of consumption of oxygen and of the carbon dredged down from the C-rich zone.

Fig. 26 suggests that the p-process might have a good chance to develop in multi-dimensionally simulated pre-supernova O-rich shells. As a bonus, the predicted 2D extended convection may provide the p-nuclides synthesized pre-explosively a better chance to survive the supernova explosion than the one offered by the 1D models. Clearly, this interesting prospect calls for future developments of multi-dimensional simulations and related studies of the nucleosynthesis in general, and of the p-process in particular.

5. Massive stars: the SNII production of the p-nuclides

After having experienced all the burning phases depicted in Fig. 23, massive stars develop an Fe core that is lacking further nuclear fuels, any transformation of the strongly bound Fe nuclei being endothermic. In fact this core becomes dynamically unstable and implodes as a result of free-electron captures and Fe photodisintegration, the former transformation playing an especially important role at the low end of the massive star range. Through a very complex chain of physical events the implosion can, in certain cases at least, turn into a catastrophic SNII explosion.

It is beyond the scope of this review to describe this highly complex phenomenon. The interested reader is referred to e.g. [104, esp. Chapters 12 and 13] for the detailed discussion of its mechanism and for the model predictions of its observables (see also a recent status report by [128]). In very short, the sequence of physical events leading eventually to a SNII event following the dynamical implosion of the core mentioned above starts with the production of neutrinos in the innermost stellar regions. The diffusion of these neutrinos through the supernova crucially helps the generation and powering of a shock wave propagating outward through most of the supernova layers. This shock

wave compresses the various traversed layers, heats them up before pushing them outward until their ejection into the ISM. This expansion is of course accompanied by a cooling of the material. This heating and cooling process of the layers hit by the supernova shock wave allows some nuclear transformations to take place during quite a brief time, modifying more or less significantly the pre-explosion composition of the concerned layers. The study of the composition of the ejected material that makes up the supernova remnant is one of the main chapters of the theory of 'explosive nucleosynthesis'.

In this supernova picture not the whole of the stellar mass is returned to the ISM (Fig. 23). The innermost parts are bound into a 'residue', which may be a neutron star (observable as a pulsar if it is magnetized and rapidly rotating) or even a black hole. If a general consensus has been reached on the above description of massive star explosions, many very complicated astrophysics and nuclear physics questions have yet to be answered, even in the simplest spherically symmetric case sketched here. Needless to say, even more formidable problems are encountered when multidimensional calculations are attempted to simulate supernova explosions.

Following the suggestion by [11,12], most of the investigations of the p-process have been concerned with the explosion of the O–Ne-rich layers associated with SNII events. The first calculations of this type [129] made use of parametrized conditions for the thermodynamic description of the relevant supernova layers, of solar s-nuclide seeds, and of a simplified reaction network involving only (γ,n), (γ,p) and (γ,α) photodisintegrations, neutron and proton captures being totally neglected. Some other computations have followed, improving one aspect or another of this first study. The most detailed calculations performed so far [24,124] are conducted in the framework of one-dimensional explosions of non-rotating stars in the $13\text{–}15 \leqslant M \leqslant 25\ \mathrm{M}_{\odot}$ mass range (more precisely, [24] refer to the evolution of He cores with masses M_{α} in the $3.3 \leqslant M_{\alpha} \leqslant 8\ \mathrm{M}_{\odot}$ range). The metallicity is in general assumed to be solar, Section 5.4 illustrating an exception to this choice. In spite of this limitation, these extended studies represent the first step towards the quantitative build-up of a model for the evolution of the galactic p-nuclidic content.

The following discussion of the SNII p-nuclide production summarizes the computations discussed extensively by [24], and based on the stellar models of [117,118] for the aforementioned metallicity and mass range. They demonstrate that the p-process can develop in the O–Ne layers of the considered massive stars explosively heated to peak temperatures T_m comprised approximately between 1.7 and 3.3×10^9 K, a range already suggested by previous, less quantitative, studies. These zones are referred to in the following as the p-process layers (PPLs). Fig. 27 displays the distributions of PPL peak temperatures versus mass coordinates for exploding stars of several of the considered model stars. The PPLs are located close to the bottom of their O–Ne-rich zone, and are thus far enough from the SNII mass cut for their precise location not to affect the predicted p-process yields in any significant way. In contrast, these distributions, and more specifically the precise location and mass of the PPLs, are sensitive namely to the assumed final kinetic energy of the ejecta, as well as to the still somewhat uncertain $^{12}\mathrm{C}(\alpha,\gamma)^{16}\mathrm{O}$ reaction rate. The nominal values adopted for these quantities are a kinetic energy of 10^{51} erg and the reaction rate proposed by [130]. Recent experiments [131] demonstrate that this choice is quite judicious at typical non-explosive He-burning temperatures. Fig. 27 provides an illustration of the influence of a change in the adopted $^{12}\mathrm{C}(\alpha,\gamma)^{16}\mathrm{O}$ rate on the distribution of peak temperatures. The impact of a modification of this rate and of the final kinetic energy on the global SNII p-process yield predictions for the $25\ \mathrm{M}_{\odot}$ star is briefly discussed in Section 5.3. The $25\ \mathrm{M}_{\odot}$ star is also selected to analyze various questions of interest, like the impact

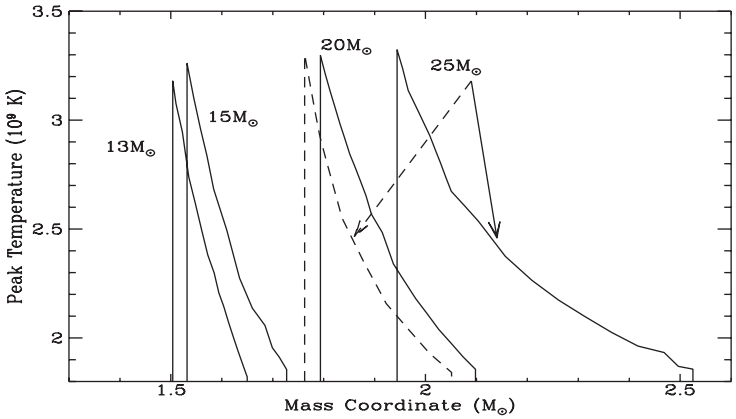

Fig. 27. PPL peak temperatures versus the interior mass for four different SNII masses. The solid lines correspond to the selection of the nominal final kinetic energy of the ejecta (10^{51} erg) and $^{12}C(\alpha,\gamma)^{16}O$ reaction rate from [130]. The dashed line is obtained when this rate is replaced by the lower one proposed by [119].

of the use of different sets of reaction rates (Section 5.5) on the p-nuclide yields. As an extension of these analyses, a comparison is briefly presented in Section 5.6 between our 25 $M_\odot$ p-nuclide abundance predictions and those of [124] obtained with different astrophysics and nuclear physics inputs. Finally, a specific discussion is devoted to the especially interesting cases of the relatively abundant Mo and Ru p-isotopes (Section 6.1) and of rare odd–odd nuclides ^{138}La (Section 6.2) and ^{180}Ta (Section 6.3).

The s-process that develops pre-explosively in the stellar mass zones making eventually the PPLs provides the seeds for the p-process. As recalled in Section 4 (see also Figs. 24 and 25), the s-process accompanying core He burning in massive stars strongly enhances the $60 \lesssim A \lesssim 90$ s-nuclei, while the abundances of the heavier nuclei are only very weakly increased. The s-abundances at core He exhaustion are likely to represent closely enough the p-process seed abundances, except in some specific cases for which corrections are imposed by the astrophysical conditions encountered between the end of He-burning and the start of the p-process [24]. One has to acknowledge that this statement is not fully correct, as some s-nuclides are already transformed prior to the explosion into p-nuclides which, however, do not survive the explosion of the considered model stars (Section 4). This slight inconsistency introduces an uncertainty in the computed final p-nuclide yields that is likely not more severe than the uncertainties in the abundance pattern of the s-seeds due to the modeling of the s-process itself and of the convective spreading of these seeds prior to the SN explosion. This inconsistency is cured in the recent computations by [124] which, however, do not discuss the impact of s-process uncertainties on the p-process yields [see Sections 5.5 (especially Fig. 34) and 6.1 for a brief analysis of some aspects of this question]. As far as the $A < 40$ species lighter than the s-nuclides are concerned, their abundances are clearly substantially modified between core He exhaustion and the onset of the explosion. Their PPL pre-explosion abundances are taken from the predictions of the adopted presupernova models (see [24] for details).

The nuclear reaction network adopted in the calculations of [24] differs slightly from the NETGEN-generated one and does not make use of the NACRE and MOST rates (Section 3.6), which were not available at the time of the study. The network is thoroughly described in [132]. In short, it includes

approximately 1050 nuclei and 11 000 reactions induced by neutrons, protons and α-particles, as well as photodisintegrations. The 3α reaction and the various $^{12}C + {}^{12}C$, $^{12}C + {}^{16}O$ and $^{16}O + {}^{16}O$ channels are also considered, so that all light particle abundances are calculated self-consistently. This is especially the case for the neutrons, the captures of which are shown by [132] to play a non-negligible role in some PPLs, at variance with the assumption made in the early calculations of [129]. The impact of the use of the NACRE and MOST rates on the predicted p-nuclide yields is discussed in Section 5.5.

5.1. Some comments on the main p-process nuclear flows

The main properties of the nuclear flows in the PPLs have already been discussed in detail by [132] in the framework of parametrized PPL thermodynamic histories characterized by a sudden increase of temperature and density to peak values T_m and ρ_m followed by their adiabatic decrease on typical e-folding timescales τ_{ex}, i.e. $T(t) = T_m \exp(-t/3\tau_{ex})$ and $\rho(t) = \rho_m \exp(-t/\tau_{ex})$. Fig. 28 shows that this approximation reproduces quite satisfactorily the SNII model predictions if τ_{ex} is shorter than $\tau_{\rm free}\ [{\rm s}] = 446/\sqrt{\rho_m[{\rm g/cm^3}]}$ adopted in Fig. 28 by a factor of the order of 1.5.

We restrict ourselves here to some limited reminders concerning the main characteristics of the p-process flows identified by [132]:

(1) the synthesis of the heavy p-nuclides requires lower-T PPLs than the one of the light p-nuclides, which are more resistant to photodisintegrations. More specifically, the light ($N \lesssim 50$), intermediate-mass ($50 \lesssim N \lesssim 82$) and heavy ($N \gtrsim 82$) p-nuclides are essentially produced in the temperature ranges $T_{m,9} \gtrsim 3$, $3 \gtrsim T_{m,9} \gtrsim 2.7$ and $T_{m,9} \lesssim 2.5$, respectively ([24,132,133] for details). Even more so, each p-nucleus is substantially produced in a narrow

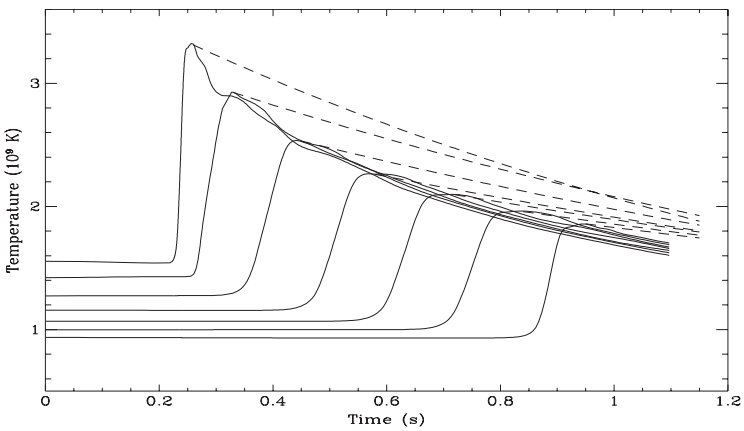

Fig. 28. Temporal temperature profiles in selected PPLs of the 25 $M_\odot$ SNII (solid lines). The dotted lines are obtained from a parametric model often used in early explosive nucleosynthesis calculations. In this model, the evolution of the temperature from the peak temperature T_m is given by $T(t) = T_m \exp(-t/3\tau_{ex})$, the corresponding density variations following $\rho(t) = \rho_m \exp(-t/\tau_{ex})$. In these expressions, τ_{ex} is a free parameter that is adopted equal to the free expansion timescale $\tau_{\rm free}[{\rm s}] = 446/\sqrt{\rho_m[{\rm g/cm^3}]}$ to derive the dashed curves.

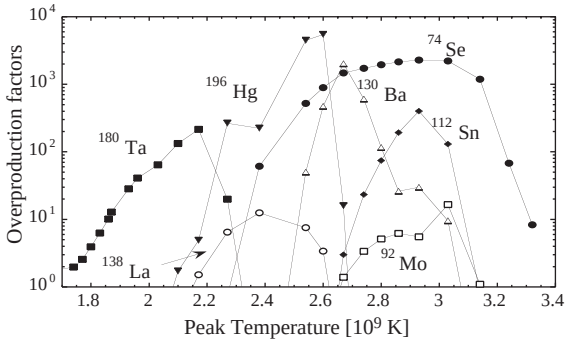

Fig. 29. Illustration of the sensitivity of the level of overproduction (with respect to solar) of some selected p-nuclides to the peak temperature $T_{m,9}$ reached in the PPLs of the 25 $M_\odot$ star already considered in Fig. 28. Here and in the following figures, the displayed ^{180}Ta data correspond to the sum of the produced short-lived $^{180}Ta^{g}$ ground state and long-lived $^{180}Ta^{m}$ isomer, the only one to be present in the solar system (see Section 6.3 for a discussion of the expected $^{180}Ta^{m}$ yields from SNII explosions).

range of temperatures only, as illustrated in Fig. 29. This extreme sensitivity of the results to T_m makes the use of realistic stellar models mandatory;

(2) starting from the s- and r-nuclides, the dominant nuclear flows go towards the neutron-deficient region through (γ,n) reactions. Along these isotopic paths, the proton separation energies get progressively smaller, while the corresponding energies for the neutrons go up. As a result, the flows to more neutron-deficient isotopes are hindered and, at some point, are deflected by (γ,p) and (γ,α) photodisintegrations. These branching points are shown in Fig. 30 as downward arrows, and correspond to a slowing down of the photo-reaction rates, where matter tends to accumulate and eventually β-decays to stable isobars after the nuclear reactions become too slow to operate on typical evolution timescales as a result of the cooling of matter (one talks about the 'freeze-out' of the nuclear reactions). This is the dominant mechanism for the production of most heavy p-nuclides at $T_{m,9} > 2.2$ (e.g. [132]);

(3) the photodisintegration flows may be impeded by neutron captures. In fact, (n,γ) reactions may compete with photo-induced reactions, and even dominate, for nuclei that are not easily photodisintegrated. This is the case for most of the lower-Z isotopes or, in general, even–even nuclei, especially in the vicinity of the branching points where both (γ,n) and (γ, p) reactions are particularly slow. The nuclides for which (n,γ) captures become the dominant reactions are represented in Fig. 30 by an arrow pointing to the right, indicating that the isotopic flux towards lighter nuclei is hindered at these points. Cases where this happens on the left of the branching points are not shown, since the nuclei in this region are only produced in negligible amounts, and do not contribute to the main nuclear flows;

(4) proton captures are never found to be the dominant transformation path for the $Z \leqslant 32$ nuclides in the conditions favorable to the development of the p-process.

The qualitative features just described are common to the two cases exemplified in Fig. 30. However, more quantitative properties depend on temperature. One concerns the position of the branching points which are located deeper into the neutron-deficient region with increasing temperature, especially for

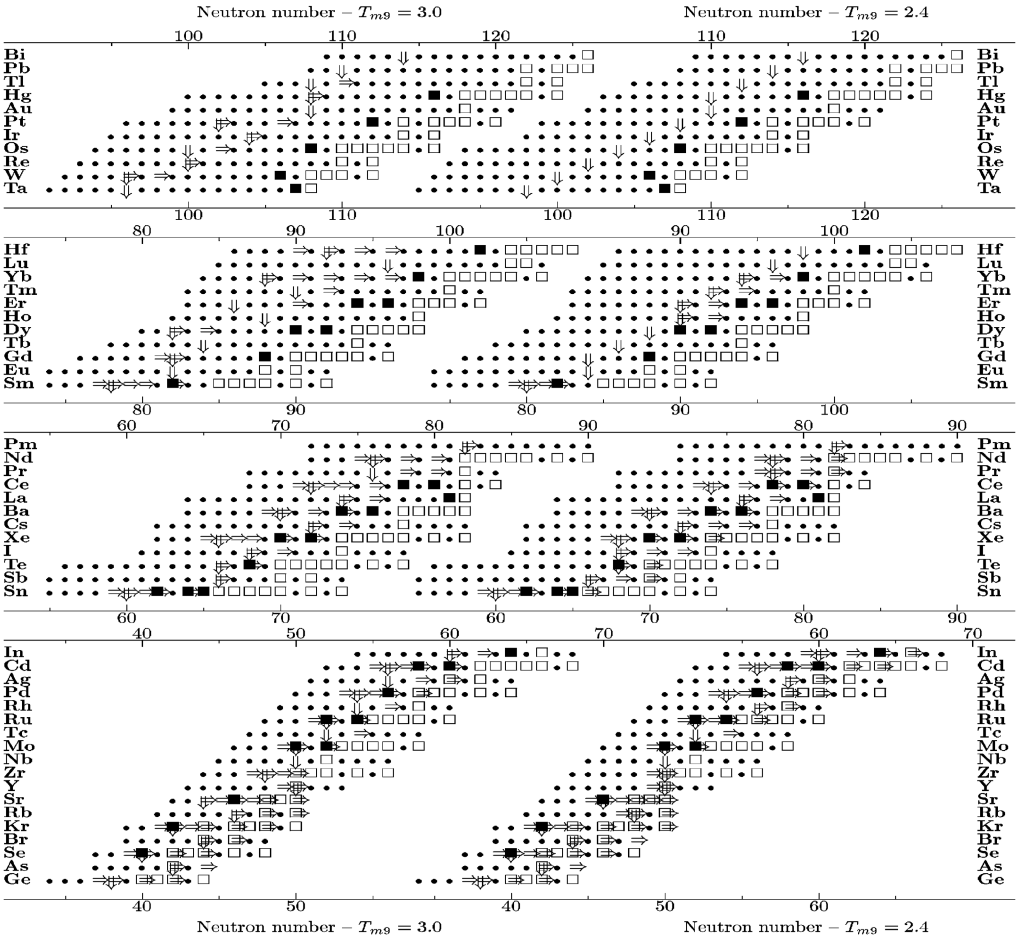

Fig. 30. Schematic representation of nuclear flows during the p-process in the $Z \geqslant 32$ range, as they result from the parametric p-process calculations of [132]. The neutron number scale is split up in order to show the relevant information on reaction fluxes for two different peak temperatures $T_{m,9} = 3$ (left part) and 2.4 (right part) at times where the maximum neutron concentrations are reached. The symbols have the following meaning: open squares s- and r-nuclides; black squares: p-nuclides; black dots: other (unstable) nuclides belonging to the network; double downward arrow: point where (γ,p) or (γ,α) start to dominate over (γ,n). At the right of such a point, the main nuclear flow is driven to the left by (γ,n) reactions; double rightward arrow: nuclides for which the (γ,n) isotopic flow is impeded by (n,γ) (from [132]).

the heaviest elements. The importance of neutron captures with respect to photo-reactions is also expected to be temperature-dependent, although their relative importance as a function of T is hard to predict on qualitative grounds.

As a final remark about the p-process flows, it has to be noted that the discussion above is based on the parametrized calculations of [132]. The mentioned general features remain essentially unchanged when the more realistic SNII models mentioned above are used.

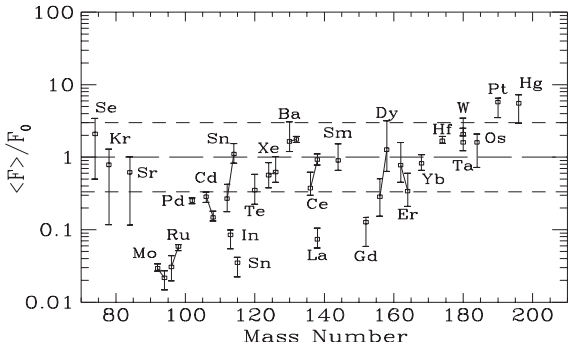

Fig. 31. Ranges of variations of the normalized p-nuclide overproductions predicted for the individual SNII explosions of $Z = Z_{\odot}$ stars with masses in the range from 13 to 25 $M_{\odot}$. For the sake of simplicity, these ranges are just schematized by vertical bars. Open squares indicate the values of the normalized overproductions obtained by integration over the IMF proposed by [134]. Solid lines join different p-isotopes of the same element. As noted in Fig. 29, the displayed ^{180}Ta data correspond to the sum of the ^{180}Ta^{g} and ^{180}Ta^{m} abundances. Roughly speaking, ^{180}Ta^{m} (the only Ta form to be present in the solar system) represents about half of the total ^{180}Ta SNII yields, as discussed in Section 6.3 (from [24]).

5.2. Predicted p-nuclide abundances: influence of the SNII mass, and IMF-averaged yields

The p-process abundances predicted by [24] are displayed in Fig. 31 in terms of normalized overproduction factors $\langle F_i \rangle(M)/F_0(M)$. The mean overproduction factor $\langle F_i \rangle(M)$ for a star with mass M is defined as the total mass of the p-nuclide i produced in its PPLs divided by the corresponding mass if the PPLs had a solar composition. The normalizing factor $F_0(M)$ is the mean overproduction factor averaged over the 35 p-nuclides listed in Table 1. With these definitions, all the normalized overproductions would be equal to unity if the derived abundance patterns were solar.

For each p-nuclide, the variations of its normalized overproduction for $Z = Z_{\odot}$ stars with masses M spanning the $13 \leqslant M \leqslant 25\ M_{\odot}$ range are represented by vertical bars, the results for individual model stars not being represented (Precise data for each of the considered stars can be found in Table 2 of [24]). Roughly speaking, these overproduction factors are seen to depend only relatively weakly on the star masses, this being less true, however, for the lightest p-nuclei ^{74}Se, ^{78}Kr and ^{84}Sr.

The SNII yields for individual stars have been used by [24] in order to evaluate for the first time the evolution of the galactic content of the p-nuclides. As a zeroth-order approximation to the build-up of a full galactic chemical evolution model, the p-process yields have been averaged over an initial mass function (IMF), leading to the IMF-averaged normalized overproduction factors displayed in Fig. 31. Of course, the build-up of a model for the temporal evolution of the galactic content of the p-nuclides not only requires the knowledge of the stellar mass dependence of their yields, but also their variations with the metallicity. This question has been first addressed qualitatively by [24] on grounds of calculations performed for the supernova 1987A (Section 5.4).

From the IMF-averaged overproduction factors displayed in Fig. 31, it is concluded that about 60% of the produced p-nuclei fit the solar system composition within a factor of 3. Some discrepancies are also apparent. In particular, the Mo and Ru p-isotopes are predicted to be severely underproduced. This problem is discussed in Section 6.1. The nuclides ^{113}In, ^{115}Sn, ^{138}La and ^{152}Gd are also

underproduced in our SNII calculations, just as in the early calculations of [11,12]. No other clear source has been identified yet for ^{113}In. In contrast, and as mentioned in Section 2.1 (Fig. 3), some ^{115}Sn and a substantial amount of the solar ^{152}Gd may owe their origin to the s-process. This process also contributes to ^{164}Er. From the level of p-process production of this nuclide shown in Fig. 31, it appears that ^{164}Er may well have a combined s- and p-origin without having to fear any insuperable overproduction with respect to the neighboring p-nuclides. The rare odd–odd nuclide ^{180}Ta^{m} emerges naturally and in quantities consistent with its solar abundances from all the considered SNII models. This interesting case is discussed further in Section 6.3.

In order for SNII to be potentially important contributors to the galactic p-nuclides, it remains to make sure that they do not produce too much of other species, and in particular oxygen, the abundance of which is classically attributed to SNII explosions. This question has been examined in some detail by [24], who conclude that the p-nuclides are globally underproduced in the $Z = Z_{\odot}$ 25 $M_{\odot}$ star by a factor of about 4 ± 2 relative to oxygen when all the abundances are normalized to the bulk solar values. The factor 4 is obtained with the nominal input physics defined in Section 5.2, and the mentioned uncertainty relates to changes in the $^{12}C(\alpha,\gamma)^{16}O$ rate and in the explosion energy discussed in Section 5.3. The problem of the oxygen overproduction may be eased in lower mass SNII explosions, while it is worsened with decreasing metallicity [24]. It may thus be that the p-process enrichment of the Galaxy has been slower than the oxygen enrichment. There is at present no observational test of this prediction. It may also be eased due to a higher than nominal production of s-nuclides, which might also help solving the Mo–Ru underproduction problem made apparent by Fig. 31, as suggested in Section 6.1. At this point, it must also be kept in mind that uncertainties in stellar convection introduce a large uncertainty (a factor of 2–3) in the oxygen yield of massive stars [135]. Likewise, the extent of the PPLs and the efficiency of the p-process might be affected. This efficiency concerns not only the explosive production of the PPLs, but also the possible survival of pre-explosively synthesized p-nuclides [12,124]. It has also to be stressed that the influence of multi-dimensional phenomena, and possibly of rotation, on the relative production of oxygen and the p-nuclides remains largely unknown.

5.3. Predicted p-nuclide abundances: influence of the $^{12}C(\alpha,\gamma)^{16}O$ rate and of the explosion energy

Test calculations have been performed by [24] in order to evaluate the impact of uncertainties in the $^{12}C(\alpha,\gamma)^{16}O$ rate and of a change in the final kinetic energy of the ejecta on the p-process yields from the $Z = Z_{\odot}$ 25 $M_{\odot}$ star already considered above. More specifically, the nominal reaction rate adopted from [130] (Section 5) has been decreased by a factor of about 2.5 in order to bring it closer to the rate proposed by [119], which is slightly lower than the lower limit of the rate derived by [131] at He-burning temperatures. On the other hand, a kinetic energy 1.5 times larger than the nominal value has been considered.

Fig. 32 shows that the abundances of ^{74}Se, ^{78}Kr and ^{84}Sr are again the most sensitive to variations in the input physics (see [24] for a discussion of this feature). More generally, the impact of the considered changes is, roughly speaking, of the same magnitude as the changes implied by the consideration of models of different masses calculated with the same input physics (more details are provided by [24]). In such conditions, the net impact of $^{12}C(\alpha,\gamma)^{16}O$ rate changes on the galactic p-nuclide enrichment, once properly evaluated from IMF-averaged yields (see Section 5.2), is likely

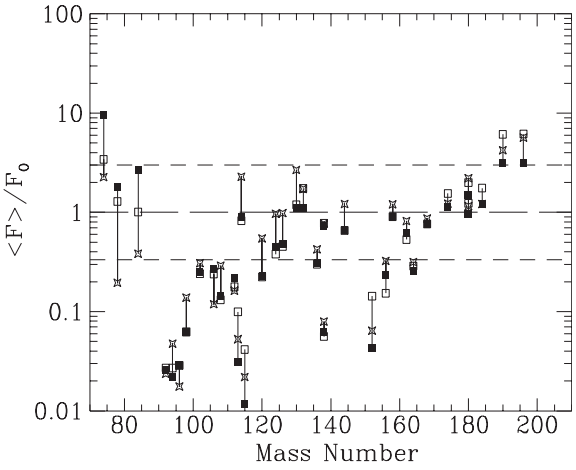

Fig. 32. Values of the normalized overproduction factor $\langle F_i \rangle (M)/F_0(M)$ calculated for three different 25 $M_\odot$ explosion models: (a) the nominal case defined above (open squares), (b) same as (a), but with $^{12}C(\alpha,\gamma)^{16}O$ rates divided by a factor of 2.5 (asterisks), and (c) same as (b), but with a final explosion kinetic energy increased by a factor of 1.5 (black squares) (from [24]).

to be weakened to some extent with respect to the changes derived for just one star, as displayed in Fig. 32.

5.4. Predicted p-nuclide abundances: influence of metallicity

The question of the influence of metallicity has been addressed qualitatively by [24], who have just evaluated the role of metallicity on the p-process yields from a comparison between the results obtained for the 20 $M_\odot$ star with $Z = Z_\odot$ and the predictions by [133] for the 20 $M_\odot$ SN1987A progenitor with the Large Magellanic Cloud metallicity $Z \approx 0.3\, Z_\odot$. In the considered Z range, the 20 $M_\odot$ PPL characteristics are expected to be essentially the same, so that a metallicity change mostly affects the efficiency of the s-process responsible for the p-process seeds [121]. In fact, it appears that the p-process is about twice less efficient in SN1987A than in its solar metallicity counterpart, while the relative yields are globally quite similar, as illustrated in Fig. 33. Even if this conclusion is likely to be safely extrapolated to the other considered model stars, the question of the influence of metallicity on the p-process in SNII clearly deserves further studies.

5.5. Impact of changes in reaction rate estimates on the predicted p-nuclide yields

As already stressed above, the SNII yields of [24] displayed in Figs. 31–33 have been calculated by making use of sets of reaction rates that have by now been superseded by the NACRE and MOST values (Section 3.6). It is worth analyzing the impact of the selection of these new rate sets on the p-nuclide yield predictions. This sensitivity study is conducted for the 25 $M_\odot$ model only.

Fig. 34 isolates the impact of just replacing the [119] rates on targets up to Si by the recommended NACRE rates, all the other nuclear and astrophysics ingredients of the calculations being kept identical to those adopted in Section 5.2. The main changes are seen to affect almost exclusively

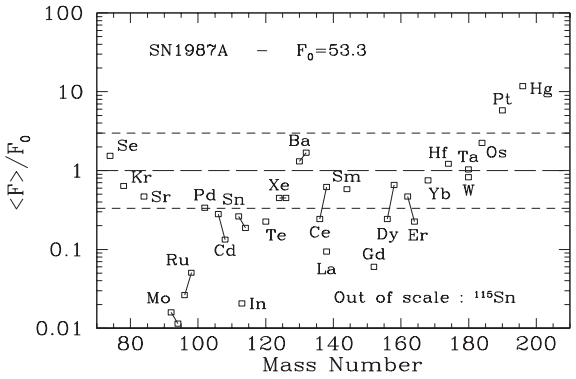

Fig. 33. Same as Fig. 31, but for normalized p-nuclei overproductions predicted for the $Z = 0.3\ Z_{\odot}$ 20 $M_{\odot}$ SN1987A progenitor (from [133]).

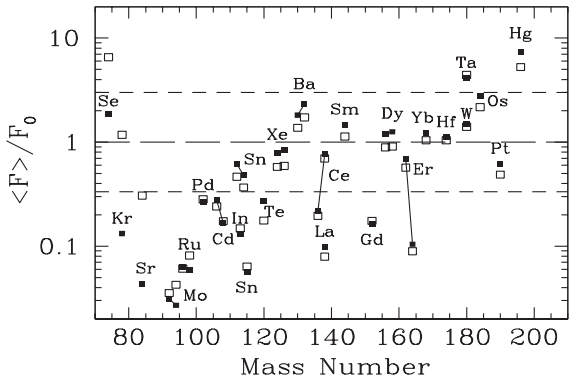

Fig. 34. Comparison between the p-nuclide normalized overproduction factors for the $Z = Z_{\odot}$ 25 $M_{\odot}$ star calculated with the two different sets of rates for charged particle captures by targets up to Si already considered in the calculations of the s-process displayed in Fig. 25. The black and open squares correspond to the adoption of the NACRE recommended rates and to the rates from [119], respectively (M. Rayet, private communication).

the calculated abundances of the lightest p-nuclides. This is a direct consequence of modifications in the efficiency of the core He-burning s-process, and more specifically in the amount of produced neutrons, when switching from the [119] to the NACRE rates. Fig. 35 complements the analysis presented in Fig. 34. It is obtained from the use of the network and input physics described in Section 3.6, the 14 sets of MOST rates (Table 2) being considered. The large variations in the abundances of the heaviest p-nuclides result almost entirely from the use of different α-nucleus optical potentials. This situation makes especially unfortunate the lack of experimental data which could help constraining these potentials in the heavy mass range (see Section 3.3.4). The abundances of the lighter species are mainly affected by uncertainties in the predicted nuclear level densities (Section 3.3.3) and the nucleon-nucleus potential (Section 3.3.4). While the considered nuclear uncertainties are seen to influence the nucleosynthesis predictions in a non-negligible way, they obviously cannot be held responsible for the large underproduction neither of the Mo and Ru p-isotopes,

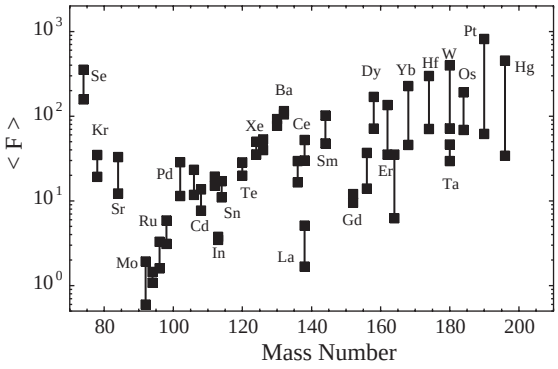

Fig. 35. Impact of the nuclear uncertainties on the p-nuclide overproduction factor $\langle F \rangle$ by the $M = 25\ M_\odot$ SNII model. The reaction network and nuclear inputs are those described in Section 3.6. Displayed for each nuclide are the maximum and minimum abundances predicted from the p-process calculations performed with the 14 Sets of rates obtained from the nuclear input combinations defined in Table 2. Note that the maximum and minimum abundances are not necessarily obtained with the same rate sets for all the p-nuclides.

nor of ^{113}In, ^{115}Sn or ^{138}La already encountered in the earlier calculations of [24], as seen in Fig. 31. The slightly increased Se overproduction shown in both Figs. 34 and 35 may be a matter of concern. Of course, it has to be kept in mind that the above discussion only concerns a 25 $M_\odot$ star with $Z = Z_\odot$. It should be pursued for a wide range of stellar masses and metallicities.

5.6. A comparison between two sets of p-nuclide abundances predicted by different authors using different astrophysics and nuclear physics inputs

Nucleosynthesis calculations including the p-process have been conducted recently by [124] in the framework of an improved version of the evolution models of [136] for $Z = Z_\odot$ stars in the $15 \leqslant M \leqslant 25\ M_\odot$ range. The nucleosynthesis is followed with the help of a network involving more than 1000 nuclides connected by the same types of reactions as those referred to in Section 3.6. The adopted standard set of rates differs, however, from the standard MOST one, while being very similar to the MOST rates obtained with Set 10 of Table 2. Two other sets of rates are also used for light targets, one of them including the adopted NACRE rates [except for $^{12}C(\alpha,\gamma)^{16}O$].

Fig. 36 compares the p-nuclide yields predicted from the SNII explosion of the 25 $M_\odot$ star already considered in Sections 5.2, 5.3 and 5.5 with the ones obtained by [124] for their model N25, i.e. the case of a 25 $M_\odot$ star with the selection of the NACRE rates for the $Z \leqslant 14$ targets. Roughly speaking, the overall agreement between the two calculated distributions appears to be reasonably good, considering that the stellar models and a substantial part of the nuclear physics input are different. The most important discrepancies concern ^{78}Kr, ^{84}Sr, ^{180}Ta^m and ^{190}Pt. For the two light nuclides, the situation may be due, in part at least, to the significant pre-supernova contribution limited to the three lightest p-nuclides obtained by [124] for the considered star, while it is negligible in our calculations. The reason for the discrepancy at ^{190}Pt cannot be easily identified, but may well be of nuclear physics origin, and in particular to the use of different α-particle OPs. The case of ^{180}Ta^m is quite complicated, as discussed further in Section 6.3. The total ^{180}Ta abundance shown in

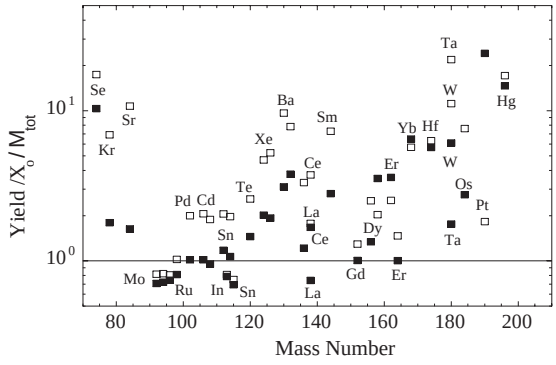

Fig. 36. Comparison between the p-process predictions of [124] for their 25 $M_\odot$ star N25 (open squares) and the results for the 25 $M_\odot$ star already considered in Section 5.2 obtained with the network defined in Section 3.6 and the ST MOST rates (black squares). The ordinate provides the mass fraction of the p-nuclides in the total initial mass M_{tot} at the SN stage normalized to the solar mass fraction [13]. These normalized mass fractions are obtained under the assumption that the ejected layers in which the heavy elements remain unprocessed during the whole evolution of the star keep their initially solar mass fractions of p-species. If a p-nuclide has an ordinate value lower than unity, its amount ejected at the SN stage is smaller than its quantity acquired by the star at its birth.

Fig. 36 (about half of which is in the form of the Ta isomeric state present in the solar system, see Fig. 31), is obtained in our calculations without considering any possible production by the neutrino interactions making up the so-called *ν*-process which may develop during the SNII explosion (See Section 6.2). In contrast, part of the abundance taken from [124] is due to such a process, which is included in their calculations in the form of inelastic neutral-current scatterings. The role of the *ν*-process in the synthesis of ^{180}Ta and of other species, and in particular of the other rare odd–odd nuclide ^{138}La, is discussed further in Sections 6.2 and 6.3.

Finally, let us note that the $M = 25\,M_\odot$ star is found by [124] to overproduce ^{16}O relative to the average p-nuclide production, a situation already encountered by [24] (see Section 5.2). More specifically, a value of about 14 is predicted by [124] in the scale of Fig. 36. This value is quite similar to the one derived from the 25 $M_\odot$ star considered by [24] once their data (see their Table 3) is translated in the scale of Fig. 36.

6. An examination of some puzzling cases

6.1. The underproduction of the light Mo and Ru isotopes: is the s-process a troublemaker?

In spite of their many virtues in reproducing the solar-system p-nuclide abundance distribution, the models calling for the transformation of seed s- into p-nuclides in the SNII O–Ne layers suffer from some shortcomings. As stressed in Section 5.2, one of them concerns the persistent and marked underproduction of the light Mo (^{92}Mo, ^{94}Mo) and Ru (^{96}Ru, ^{98}Ru) p-isotopes. Some have tried to remedy this situation with exotic solutions, calling in particular for a combined contamination of the solar system by ejecta from accreting neutron stars and black hole accretion disks

(e.g. [137]). Needless to say, the level of such a contamination is just impossible to assess in any reliable way.

In contrast, it has been emphasized many times over the last decade that the problem might just be due to some misrepresentation of the production in the He-burning core of massive stars of the s-nuclide seeds for the p-process (e.g. [138]; see also Section 4.2). This possible 'non-exotic' solution to the problem of the synthesis of the light Mo and Ru isotopes has started to be scrutinized in a quantitative way by [139], who have examined the impact of the large uncertainties in the ^{22}Ne$(\alpha,n)^{25}$Mg rate reported by the NACRE compilation of reaction rates [103]. More specifically, the NACRE upper limit to this rate is as much as about 20 to 500 times higher than the reported 'adopted' value in the 2.5 to 3.5×10^8 K temperature range of relevance to the s-process in massive stars. The s-process in the He-burning core of the aforementioned $Z=Z_{\odot}$ 25 $M_{\odot}$ model star has been computed in detail by [139] with the use of different sets of ^{22}Ne$(\alpha,n)^{25}$Mg rates lying between the NACRE adopted and upper limit values. On these grounds, it is concluded that the ^{94}Mo and ^{98}Ru underproduction is eliminated for a neutron production rate that is about 50 times the NACRE adopted value, the ^{92}Mo and ^{96}Ru underproduction being limited to less than a factor of 3 in these conditions. For a ^{22}Ne$(\alpha,n)^{25}$Mg rate limited to 10 times the adopted value, the Mo and Ru p-isotope underproduction amounts to a factor of only 2–5. In addition to the substantial increase in the production of the light Mo and Ru isotopes, [139] also noted some other pleasing features directly related to an increase of the ^{22}Ne$(\alpha,n)^{25}$Mg rate. In particular, the overall underproduction of the p-nuclides with respect to oxygen mentioned in Section 5.2 would be largely cured at the same time.

At first sight, it might be felt that the s-process abundance distributions obtained with ^{22}Ne$(\alpha,n)^{25}$Mg rates much in excess of the NACRE adopted values exhibit some unwanted or embarrassing features. One of these concerns the underproduction of the $70\lesssim A\lesssim 80$ s-nuclides relative to the $A\approx 90$ ones. Another one relates to the fact that a more or less substantial production of heavy s-nuclides (like in the Ba region) would screw up the pattern of the s-process main component ascribed to lower-mass stars. The opinion is expressed by [139] that none of these predictions can really act as a deterrent to ^{22}Ne$(\alpha,n)^{25}$Mg rates substantially in excess of the NACRE adopted value. This conclusion contradicts the statement made by [124] that 'an intolerably strong s-process may result'. It is even suggested by [139] that a discrepancy, if any, between the observed Ba overabundance in the SN1987A ejecta [140] and the model predictions could be cured in a natural way by increasing the adopted ^{22}Ne$(\alpha,n)^{25}$Mg rate.

The array of pleasing features reported above was hardly brought to light by [139] that new experimental results on ^{22}Ne$(\alpha,n)^{25}$Mg [141] have casted doubts on the plausibility of its rate being increased by the requested amounts (factors of at least 5–10 with respect to the NACRE adopted rate). In fact, the new upper limit of the rate proposed by [141] is roughly equal to the NACRE adopted rate in the $2–3\times10^8$ K range. If true, the answer to the puzzle of the synthesis of ^{92,94}Mo and ^{96,98}Ru does not lie in the ^{22}Ne$(\alpha,n)^{25}$Mg rate. The 'saga' of this rate does not seem to have come to an end yet, however. From a careful analysis of the ^{nat}Mg + n total and ^{25}Mg(n,γ) cross sections, [142] concludes that [141] underestimate the uncertainties in their measured ^{22}Ne$(\alpha,n)^{25}$Mg rates by at least a factor of 10 in the temperature range of interest for the s-process. It is thus fair to conclude that the precise responsibility of an incorrect evaluation of the s-process neutron production in the calculated underabundances of the Mo and Ru p-isotopes remains an open problem. The s-process may also be a troublemaker in the abundance predictions of these species through its more

astrophysics aspects, some of which still lack a detailed scrutiny (Section 4.2). This concerns e.g. the possible effects of rotation or of much debated 'extra-mixing' processes on the predicted s-process yields. Anyway, the fact that the answer to the question of the exact SNII contribution to the solar system light Mo and Ru isotopes still eludes us provides a reasonable alibi to scrutinize if other astrophysically plausible nucleosynthetic agents could have the required efficiency to account for the measured ^{92,94}Mo and ^{96,98}Ru abundances. An example of this kind is discussed in Section 8.3.

6.2. The puzzle of the origin of the rare nuclide ^{138}La: a nuclear physics solution?

The odd–odd neutron-deficient heavy nuclides ^{138}La and isomeric ^{180}Ta^{m} are among the rarest solar system species (Fig. 3). In spite of its very small abundance (^{138}La/^{139}La $\approx 10^{-3}$), ^{138}La is underproduced in all p-process calculations performed so far (Figs. 31–35). This results from an unfavorable balance between its main production by ^{139}La(γ,n)^{138}La and its main destruction by ^{138}La(γ,n)^{137}La, even in the PPLs that are most favorable to the ^{138}La production (in the $Z=Z_{\odot}$ $M=25$ M$_{\odot}$ SNII model already considered above, these PPLs correspond to peak temperatures around 2.4×10^{9} K, as shown in Fig. 29).

In view of the low ^{138}La abundance, it has been attempted to explain its production by non-thermonuclear processes (Section 1) involving either stellar energetic particles [5,6] or neutral current neutrino-induced transmutations [143]. The former mechanism is predicted not to be efficient enough, except under ad-hoc assumptions, while the latter is found by [143] to be able to overproduce the solar ^{138}La/^{139}La ratio by a factor of about 50. This prediction has to be taken with some care, however, especially in view of the qualitative nature of the evaluation.

The thermonuclear inability to produce ^{138}La in large enough quantities might just result from inadequate astrophysics and/or nuclear physics inputs. On the astrophysics side, one might incriminate an uncertain prediction of the evolution of the thermodynamic conditions of the ^{138}La producing layers during the explosion. Modifying these conditions is unlikely, however, to cure the ^{138}La underproduction. For any astrophysically plausible conditions, the SNII layers releasing the highest ^{138}La yields are also those overproducing even more significantly heavier p-nuclides, such as ^{156}Dy, ^{162}Er or ^{168}Yb. Of course, it remains to be seen if the situation could be drastically modified if multi-dimensional effects were duly taken into account at the SN stage. On the nuclear physics side, one has to be aware of the fact that the ^{138}La yield predictions rely entirely on theoretical nuclear reaction rates. One is thus entitled to wonder about the sensitivity of the computed ^{138}La underproduction to the nuclear uncertainties that affect the production and destruction channels.

This question has been tackled in a quantitative way by [145] on grounds of the solar metallicity $M=25$ M$_{\odot}$ SNII model already considered above. The abundances of the s-process seeds for the production of the p-nuclides are calculated with the NACRE adopted ^{22}Ne(α,n)^{25}Mg rate, as described by [139]. The standard version of the nuclear reaction network defined in Section 3.6 is adopted for the p-process calculations. The only exceptions concern ^{137}La(n,γ)^{138}La and ^{138}La(n,γ)^{139}La, from which the reverse (γ,n) rates of direct relevance to the question of the production of ^{138}La are evaluated by the application of the reciprocity theorem (Eq. (5)). More specifically, [145] examine the extent to which the rate of ^{137}La(n,γ)^{138}La has to be *decreased* and the one of ^{138}La(n,γ)^{139}La *increased* in order to bring the ^{138}La overproduction at levels comparable with those of the neighboring p-nuclides. In the following, the factors of decrease and increase are noted $F_{\rm down}$ and $F_{\rm up}$, respectively. The corresponding reverse photodisintegration rates are decreased and increased by the

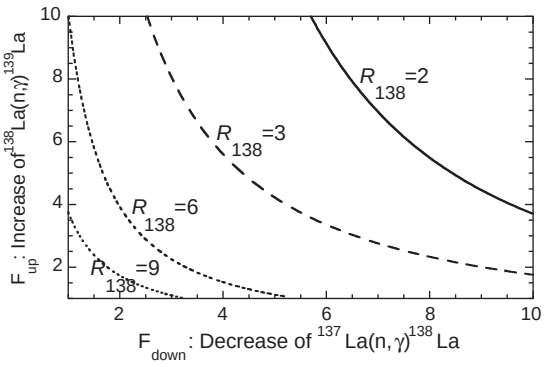

Fig. 37. ^{138}Ce to ^{138}La overproduction ratio R_{138} for different values of the factors $F_{\rm down}$ and $F_{\rm up}$ by which the standard ST MOST rates (Section 3.4) of ^{137}La(n,γ)^{138}La and ^{138}La(n,γ)^{139}La are decreased or increased.

same factors. In the numerical tests of [145], $F_{\rm down}$ and $F_{\rm up}$ are selected to vary independently in the 1–10 range.

Fig. 37 shows the ratio $R_{138} = \langle F(^{138}\mathrm{Ce})\rangle / \langle F(^{138}\mathrm{La})\rangle$ obtained in this test. The choice of ^{138}Ce as the normalizing p-nuclide is dictated by the fact that it is produced in an amount close to the average value F_0 defined in Section 5.2, so that R_{138} gives a good representation of the ^{138}La production by the p-process. It is seen that R_{138} is pushed inside the $0.3 \leqslant \langle F\rangle / F_0 \leqslant 3$ range represented in Figs. 31–33 only for $F_{\rm down} \times F_{\rm up} \approx 20$–25. Following the analysis of [145], it appears likely that errors in the capture rate predictions can amount to about a factor of 2 for ^{138}La(n,γ)^{139}La at the temperature of relevance (2.4×10^9 K) for the ^{138}La synthesis. In view of scarcer experimental information able to constrain the rate prediction, larger uncertainties affect the ^{137}La(n,γ)^{138}La rate. Even so, it is unlikely that the product $F_{\rm down} \times F_{\rm up}$ introduced above can realistically reach the requested value of about 20–25 in order for the underproduction of ^{138}La with respect to ^{138}Ce not to exceed a factor of 3. Of course, only experimental determinations of the ^{138}La and ^{139}La photodisintegration rates could really put this theoretical conclusion on a safe footing. Such experiments are now contemplated (Section 3.1).

While waiting for such laboratory efforts, [145] have revisited the possibility of producing ^{138}La at a level compatible with the solar system abundances through the interaction (ν-process; [143]) of the SN material with the (anti)neutrinos streaming out of the nascent neutron star resulting from the $M = 25\ \mathrm{M}_\odot$ explosion model considered above. The p-process network used throughout Section 5 is augmented with all neutrino-induced reactions (charged and neutral currents) up to Kr, as well as all charged-current neutrino and antineutrino scatterings up to Po. The neutral-current scatterings off nuclei heavier than Kr are considered only for the Ba, La and Ce isotopes of relevance to the ^{138}La synthesis, as well as for those of Hf, Ta and W entering the study of the ^{180}Ta production (Section 6.3). The details concerning the evaluation of these neutrino cross sections and the adopted time-dependent fluxes of the various neutrino types can be found in [145], and are not repeated here. [3]

[3] The work of [145] was completed by the time the SNO collaboration has announced that their neutrino data were supporting the existence of neutrino oscillations [146]. A quantitative analysis of the impact of this exciting discovery on the ν-synthesis of ^{138}La remains to be conducted.

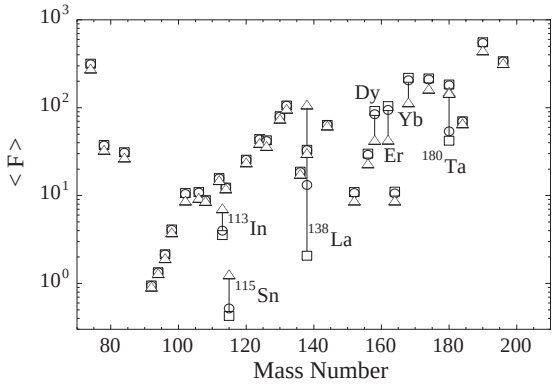

Fig. 38. Comparison of the p-process overabundances obtained with and without (squares) neutrino interactions (with standard MOST rates). Two sets of luminosities $L_\nu[10^{51}\ \text{ergs s}^{-1}] = (3, 4, 16)$ (circles) and (30, 40, 160) for $(\nu_e, \bar{\nu}_e, \nu_x)$ (triangles) are adopted for the calculations with neutrinos.

Fig. 38 shows the impact of the neutrino interactions on the p-nuclide production for the two sets of typical neutrino luminosities [147] $L_\nu[10^{51}\ \text{ergs s}^{-1}] = (3, 4, 16)$ and $(30, 40, 160)$ for ($\nu_e, \bar{\nu}_e$ and ν_x) (x stands for μ and τ (anti)neutrinos). These two L_ν combinations lead to increases of the ^{138}La production with respect to the case without neutrinos by factors of 4.8 and 36, respectively. This enhanced synthesis originates entirely from the ν_e-capture by ^{138}Ba, the neutral current scatterings on ^{139}La being found to have an impact limited to about 10% only. Despite relatively similar cross sections, the ^{138}Ba ν_e-capture is found particularly efficient due to the large initial ^{138}Ba abundance (about 10 times the ^{139}La one). For the high luminosity set, the ν_e-captures also enhance the production of ^{113}In, ^{115}Sn and ^{180}Ta, but slightly decrease the production of the Dy, Er and Yb p-isotopes. Despite the numerous uncertainties still affecting supernova models and the neutrino physics in supernovae (spectra, luminosity, temperature, oscillation, interaction cross sections,…), ν_e-captures appear so far to be the most efficient production mechanism of the solar ^{138}La in SNII explosions. This conclusion does not preclude at all a substantial fraction of the solar ^{138}La from having a thermonuclear origin if agents other than SNII could have contaminated the solar system with p-nuclides. Section 8.3 identifies sub-Chandrasekhar White Dwarf explosions as potential contributors of this sort.

6.3. *The p-process character of* $^{180}Ta^{m}$

The odd–odd nuclide ^{180}Ta has the remarkable property of having a short-lived ($t_{1/2} = 8.15$ h) $J^\pi = 1^+$ ground state (^{180}Ta^{g}) and a very long-lived ($t_{1/2} > 1.2 \times 10^{15}$ yr) $J^\pi = 9^-$ isomeric state (^{180}Ta^{m}). As a result, only ^{180}Ta^{m} is present in the solar system. Its minute abundance (^{180}Ta^{m}/^{181}Ta $\approx 10^{-4}$) is enough to give it the status of the only naturally occurring isomer in nature.

The study of the ^{180}Ta^{m} production raises the specific problem of the possibility of thermalization of ^{180}Ta^{g} and ^{180}Ta^{m} in stars. This question is of substantial interest for evaluating the effective decay lifetime, and thus the probability of survival, of ^{180}Ta in those conditions. As in the case of nuclear reactions (see Section 3.3.1 and Eq. (4)), it is obtained in thermal equilibrium conditions as a sum over the decay rates of the ground and excited states weighted with their Maxwell–Boltzmann

populations. As a result, the ^{180}Ta^{m} effective decay lifetime may be dramatically reduced in stars with respect to the value measured in the laboratory. The question of the stellar thermalization of ^{180}Ta^{g} and ^{180}Ta^{m} has been investigated many times over the years. Clearly, this cannot be reached through direct and highly forbidden transitions between the ground and isomeric states. Instead, it has been demonstrated recently that this equilibration can be obtained through a series of mediating levels located at excitation energies $E_x > 1$ MeV [148,149] for temperatures in excess of the critical value $T_{9,\mathrm{crit}} \gtrsim 0.4$. In these conditions, the stellar ^{180}Ta^{m} effective lifetime $\tau(^{180}\mathrm{Ta}^{m})_*$ is close to the laboratory ground state value $\tau(^{180}\mathrm{Ta}^{g})_{\mathrm{lab}}$. In contrast, temperatures $T_9 \lesssim 0.15$ do not allow a sufficient population of the state for it to play its mediating role with sufficient efficiency, so that $\tau(^{180}\mathrm{Ta}^{m})_*$ recovers its laboratory value. In the intermediate $0.15 \lesssim T_9 \lesssim 0.4$ temperature regime, the non-Maxwellian populations of the levels involved in the evaluation of $\tau(^{180}\mathrm{Ta}^{m})_*$ have in principle to be calculated from kinetic equations involving the various transition probabilities of relevance. In practice, however, this computation is not required. Indeed, the cooling from $T_9 = 0.4$ to $T_9 = 0.15$ of the SNII PPLs responsible for the ^{180}Ta^{m} synthesis (i.e. the layers with $T_{9,m} \approx 2$, as seen in Fig. 29) takes place on timescales shorter than about 2 s. The order of magnitude estimate of the duration of this transition regime is obtained by approximating the temperature history of the relevant layer by $T(t) \approx 2\exp(-t[s]/1.8)$, which is seen from Fig. 28 to reproduce reasonably enough the profile predicted by the detailed SN model for the 25 $M_\odot$ star. During this estimated 2 s time interval, even the fully equilibrated ^{180}Ta would have no time to decay. It has to be stressed that the above-mentioned $T_{9,\mathrm{crit}}$ value should have to be lowered if mediating states with excitation energies below 1 MeV were found, which cannot be excluded by the present experiments. This would shorten further the duration of the transition regime.

From the above discussion, one concludes that ^{180}Ta equilibrated at temperatures in excess of $T_{9,\mathrm{crit}}$ can survive to a substantial extent after the freezing of its production or destruction photodisintegrations assumed to take place at $T = T_{\mathrm{freeze}}$ if

$$\Delta t(T_{\mathrm{freeze}} \rightarrow T_{\mathrm{crit}}) \ll \tau(^{180}\mathrm{Ta}^{m})_* \approx 12\ \mathrm{h}\ , \tag{9}$$

where Δt is the time needed for the temperature to decrease from T_{freeze} to T_{crit} ($T_{\mathrm{freeze}} \gg T_{\mathrm{crit}}$ in all realistic conditions). Adopting the 25 $M_\odot$ star profile considered just above, a typical value $T_{9,\mathrm{freeze}} = 1$ and $T_{9,\mathrm{crit}} = 0.4$, $\Delta t \approx 1.65$ s, so that the survival criterion is largely fulfilled in the considered SNII scenario. At a critical temperature $T_{9,\mathrm{crit}}$, the amount of ^{180}Ta in its isomeric form is given by

$$p_m = \frac{1}{1 + (2J^g + 1)/(2J^m + 1)\exp(E^m/kT)} = \frac{1}{1 + 3/19\exp(0.874/T_{9,\mathrm{crit}})}\ , \tag{10}$$

where $E^m = 75.3$ keV and $J^m = 9$ are the energy and spin of the isomeric state, and $J^g = 1$ is the ground state spin. Thus, at $T_{9,\mathrm{crit}} = 0.4$, about 40% of the ^{180}Ta produced at the SN stage can survive in its isomeric form and be injected into the ISM. Some test calculations have also been conducted prior to the experiments of [148,149] under the extreme assumption that ^{180}Ta^{g} and ^{180}Ta^{m} never equilibrate during the p-process. In these conditions, about half of the total ^{180}Ta is found to be in its isomeric state, a figure similar to the 40% reported above. The situation concerning the survival of ^{180}Ta^{m} possibly produced at the pre-SN stage is quite different, the fulfillment of requirement (9)

being unlikely. Anyway, the p-nuclides produced at the pre-SN stage are predicted not to survive the eventual explosion in some of the considered models (Section 4.3). All in all, the pre-SN p-process contribution to the solar Ta is most likely to be insignificant.

Explosions of the SNII type appear to be much more efficient $^{180}Ta^{m}$ producers, even after reducing by the factor of about 2 discussed above the $^{180}Ta^{g} + {}^{180}Ta^{m}$ overabundances displayed in Figs. 29–36 and 38 in order to isolate the $^{180}Ta^{m}$ abundances to be compared to the solar system value. After accounting for this correction, it is apparent from the discussion of Sections 5.2–5.5 and from Figs. 29–36 and 38 that $^{180}Ta^{m}$ is overproduced in SNII events at comparable levels as the neighboring p-nuclides. Such explosions thus appear as privileged sites for the origin of $^{180}Ta^{m}$. This result confirms the conclusions of [133] based on parametrized p-process calculations (see Section 5.1). Surprisingly enough, it has remained sometimes unnoticed or incorrectly appreciated in the nuclear astrophysics literature for the last fifteen years. As an example, [148] claim that 'In spite of considerable experimental and theoretical efforts the nucleosynthesis of $^{180}Ta^{m}$ still represents an unsolved problem' (the same claim is repeated by [149]), and put the p-process among 'more speculative scenarios'! More specifically, [149] consider as a serious embarrassment of the p-process model for the production of $^{180}Ta^{m}$ the fact that it can emerge in substantial quantities only from a highly restricted ensemble of SNII PPLs with peak temperatures in the close vicinity of 2×10^{9} K (Fig. 29). This criticism does not really appear as well-grounded as O–Ne layers satisfying this constraint are clearly found in all SNII models, even if the masses of these zones may vary from one model to the other (this statement refers at least to spherically symmetric one-dimensional supernova simulations). As an illustration of the robustness of the predictions concerning the ability of the p-process to synthesize $^{180}Ta^{m}$, we note that the conclusions of [124] in this respect are in line with those derived by [24] (Fig. 31) even if use was made of different underlying models.

True, the predicted $^{180}Ta^{m}$ SNII yields suffer from some nuclear uncertainties on top of the question of the thermalization discussed above. Among them are the ones concerning the rates of the $^{181}Ta(\gamma,n)^{180}Ta$ and $^{180}Ta(\gamma,n)^{179}Ta$ photodisintegrations which most directly influence the $^{180}Ta^{m}$ production and destruction. The latter cannot be estimated from experimental data using the reciprocity theorem (Eq. (5)), the radiative neutron capture cross section on the unstable ^{179}Ta being unmeasured. As mentioned in Section 3.1, the situation concerning the former reaction has recently been substantially improved. On the one hand, the $^{180}Ta^{m}(n,\gamma)^{181}Ta$ cross section has been measured by [150]. This experimental information can enter the calculation of the rate of the reverse photodisintegration of direct interest through the application of the reciprocity theorem. As noted in Section 3.1, the $^{181}Ta(\gamma,n)^{180}Ta$ cross section has even been measured directly, the relative production by this reaction of the ground and isomeric states of ^{180}Ta being obtained experimentally as well [33,35]. Of course, the stellar photodisintegration rate of ^{181}Ta can differ significantly from the laboratory value due to the contribution of its thermally excited states. Even so, such measurements strongly constrain the nuclear input, and in particular the $E1$-strength function (Section 3.3.5), and thus help reducing the uncertainties affecting the stellar rate predictions.

The conclusion that $^{180}Ta^{m}$ is a natural thermonuclear product of the p-process is considered to be robust, and to hold irrespectively of the intricacies and uncertainties related to the rates of the main photodisintegrations responsible for its production and destruction, to the equilibration of ^{180}Ta, or to the details of the SNII models, at least in their spherically symmetric one-dimensional approximation. These views are largely shared by [124]. Concomitantly to its thermonuclear production, $^{180}Ta^{m}$ could also owe some of its synthesis in SNII explosions to the neutrino nucleosynthesis found to be nicely

efficient in the case of the other rare odd–odd p-nuclide ^{138}La (Section 6.2). This possibility has been raised by [143] on grounds of a rather crude neutrino cross section and yield estimates. The question of the ^{180}Ta^{m} neutrino nucleosynthesis has been revisited recently in the nuclear and astrophysics framework already described in Section 6.2 for the ^{138}La case. This includes the same improved model for the evaluation of the neutrino interaction cross sections, as well as the same 25 $M_{\odot}$ SN II model, neutrino luminosities and extended reaction network. Fig. 38 shows that the neutrino interactions increase by a factor of about 3 the overproduction derived from the photodisintegration processes only, the charged current capture on ^{180}Hf being a more important contributor than the neutral current on ^{181}Ta. This extra production is of course affected by uncertainties concerning the neutrino luminosity, temperature and interaction cross sections. As in the case of ^{138}La (Section 6.2), neutrino oscillations are neglected.

Even if the p-process, possibly complemented by a neutrino nucleosynthesis contribution, can account in a natural way for the solar system ^{180}Ta^{m}, other production mechanisms have been considered. In particular, it has been suggested that ^{180}Ta^{m} could be synthesized by galactic cosmic ray-induced spallation reactions [5,6] or by the s-process. Some early calculations based on detailed stellar models [151] have suggested that ^{180}Ta^{m} could emerge from this neutron capture process developing during core carbon burning in massive ($M \gtrsim 30\ M_{\odot}$) stars. The recent experiments dealing with the thermalization of ^{180}Ta^{g} and ^{180}Ta^{m} [148,149] invalidate this possibility, however. The s-process production of ^{180}Ta^{m} during the thermal pulse phase of low- or intermediate-mass asymptotic giant branch (AGB) stars has also been envisioned. The outcome is controversial, however. While optimism is expressed by [152] about this ^{180}Ta^{m} source, a negative result is obtained by [153]. Further work on this issue is required.

7. The p-process in very massive stars exploding as pair-creation supernovae

7.1. A sketch of the evolution of very massive stars

The evolution and fate of very massive stars ($M \gtrsim 130\ M_{\odot}$) has been a matter of concern over the years, even if their very existence is, at best, difficult to assess from observation. This is motivated in particular by an attempt to interpret certain supernovae in terms of the explosion of such stars (e.g. [154]). A renewed burst of interest relates to the mounting expectation that the first generation of stars, referred to as Population III or zero-metallicity ($Z = 0$) objects, may have been quite massive (e.g. [107,108]) and could have left a distinct nucleosynthetic signature in the very young galaxies. Of course, these $Z = 0$ stars are of no concern here, as they do not contain the necessary seed s- and r-nuclides for the p-process. In the rest of this section, we will in fact be concerned only with $Z = Z_{\odot}$ stars.

At least in the spherically symmetric non-rotating approximation, the main characteristics of the evolution of very massive stars are largely governed by their initial mass M_{ZAMS}, and even more so by the mass of the oxygen core they develop. Broadly speaking (e.g. [155] for some details), stars with M_{ZAMS} in a relatively narrow region below about 100 $M_{\odot}$ are expected to experience violent pulsational instabilities followed some time later by iron core collapse similar to the one experienced by massive stars (Section 4.1). Stars with M_{ZAMS} in the approximate range $100 \lesssim M_{\mathrm{ZAMS}} \lesssim 250\ M_{\odot}$ suffer a thermonuclear explosion triggered by a copious $e^{+} - e^{-}$ pair production. They are thus

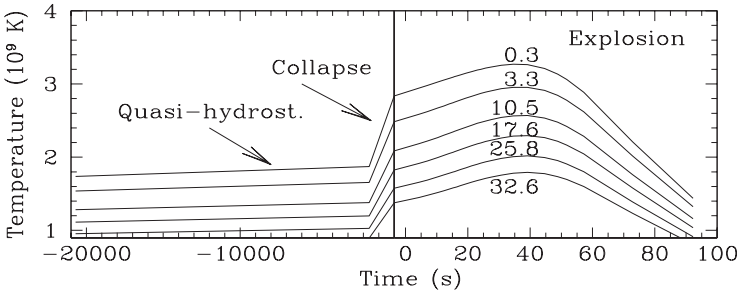

Fig. 39. Evolution of the temperature in various layers of the 50 $M_\odot$ oxygen core during its quasi-hydrostatic contraction, collapse and explosion (note the change in the timescales). The various layers are labelled with the corresponding values of $M_r/M_\odot$, where M_r is the mass inside a sphere of radius r.

naturally referred to as Pair Creation Supernovae (PCSN). The case of a $M_{\rm ZAMS} = 140\ M_\odot$ PCSN is discussed in greater detail below in relation with the development of a p-process. Finally, stars with $M_{\rm ZAMS} \gtrsim 250\ M_\odot$ are found to collapse to black holes following core helium depletion. It has to be stressed that the values of the limiting masses reported above are just indicative and suffer from uncertainties. They are also influenced by rotation which is found to enlarge the PCSN mass domain [156].

7.2. The p-process in a PCSN

The suggestion that PCSN could produce p-nuclides has first been made by [157]. The only detailed p-process calculations based on this unique scenario have been conducted by [158] on grounds of detailed models for a $Z = Z_\odot$ mass losing star with $M_{\rm ZAMS} = 140\ M_\odot$ evolving from the main sequence all the way to the PCSN.

In brief, the evolution of the considered star proceeds as follows. By the end of core He burning, the model star resembles a Wolf-Rayet star of spectroscopic type WNL. It is made of an oxygen core of about 50 $M_\odot$ surrounded by an extended He envelope still containing some hydrogen enriched with nitrogen. The further evolution of the considered star proceeds through short phases of core carbon and neon burnings, followed by a core oxygen burning stage during which the conditions are suitable for the creation of $e^\pm$-pairs that lead to the collapse of the inner core accompanied with the explosive burning of about 4 $M_\odot$ of oxygen on a timescale of about 50 s. The associated release of energy is sufficient to reverse the collapse into an explosion with a kinetic energy of 4.4×10^{51} erg. Fig. 39 shows the evolution of the temperature in various PPL candidates in the oxygen core during its quasi-hydrostatic contraction (i.e. a contraction on timescales longer than the free fall one), collapse and eventual explosion.

The p-process nucleosynthesis is followed with the help of the reaction network already adopted in the study of SNII explosions by [24] (Section 5; e.g. Fig. 31). The seed abundances are derived from a full s-process calculation (Section 4.2), the concentrations of the species lighter than Fe being obtained directly from the stellar evolution computations.

The resulting normalized overabundances of the p-nuclides (defined as in Section 5.2) are displayed in the panel of Fig. 40 labelled $M_{\rm bh} = 19\ M_\odot$. It shows a marked deficiency of the p-nuclides lighter

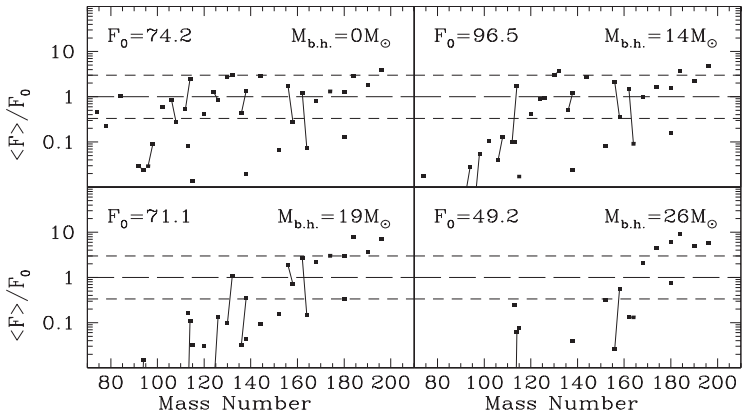

Fig. 40. Normalized p-nuclides overproductions (defined as in Section 5.2) obtained following the PCSN explosion of a $M_{\mathrm{ZAMS}} = 140\ \mathrm{M}_{\odot}$ star of solar metallicity, and for different remnant black hole masses M_{bh}, $19\ \mathrm{M}_{\odot}$ being the value derived from the detailed evolutionary computations. Solid lines join different p-isotopes of the same element.

than Ba relative to the heavy ones. As analyzed by [158], this mainly results from the trapping in the black hole remnant of the layers that are hot enough for producing significant amounts of the light p-nuclei, while not contributing to the synthesis of the heavy ones (see Section 5.1 for a discussion of the influence of the explosion temperatures on the mass ranges of dominantly produced p-nuclides). It has to be emphasized that the M_{bh} value cannot be accurately predicted. It indeed depends sensitively on the peak temperatures achieved during the collapse phase preceding the explosion. This in turn implies a high sensitivity to the total amount of consumed oxygen, or to the initial mass of the oxygen core. The value of this mass relative to the initial total stellar mass depends upon various ingredients of the model (metallicity, mass loss rate, description of the convection, extent of the convective overshooting,...). Even the absence of a remnant cannot be excluded, and is even privileged by some models. As a consequence, the level of light p-nuclei depletion is quite uncertain as well. In order to evaluate the extent of this uncertainty, Fig. 40 displays also the post-explosion overabundances predicted when $M_{\mathrm{bh}} = 0$, 14 or $26\ \mathrm{M}_{\odot}$ (in all these cases, the temperature and density profiles derived consistently in the $M_{\mathrm{bh}} = 19\ \mathrm{M}_{\odot}$ case are assumed to remain unchanged). In the extreme situation of no black hole, the global overabundance pattern qualitatively resembles the SNII one displayed in Figs. 31–35. One noticeable exception is $^{180}\mathrm{Ta}^{\mathrm{m}}$, which is found to be underproduced with respect to its neighbors as long as $M_{\mathrm{bh}} \lesssim 20\ \mathrm{M}_{\odot}$. Also note that no significant ν-process is expected to accompany stellar explosions of the PCSN type.

It is of interest to stress that, as demonstrated in Fig. 41, the PCSN p-process yields result to a very large extent from the quasi-hydrostatic evolutionary phase prior to the explosion. More specifically, the heavy p-nuclides, which emerge from relatively cool regions, appear to be almost unaffected by the explosion. In contrast, the explosion produces a substantial fraction of the three lightest ones, the synthesis of which requires high temperatures (and which would be locked in the remnant for $M_{\mathrm{bh}} \gtrsim 15\ \mathrm{M}_{\odot}$). In the intermediate-mass range, the p-nuclides are either slightly produced or destroyed during the explosion, the largest destruction occurring for low-abundance species, like $^{113}\mathrm{In}$, $^{115}\mathrm{Sn}$ or $^{152}\mathrm{Gd}$. These results remind of the possibility for part at least of the p-nuclide yields

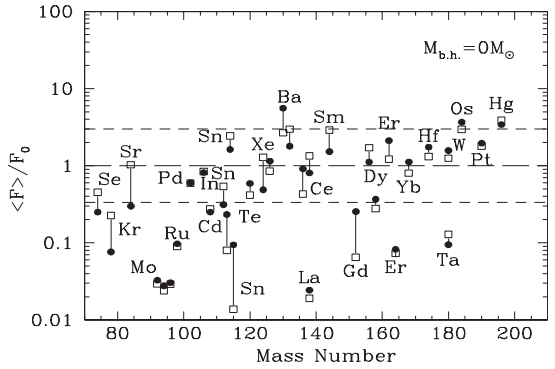

Fig. 41. Comparison between the p-process yields obtained just prior (black dots) and after (open squares) the PCSN explosion, assumed here to leave no remnant. The relative abundance changes due to the explosion would not be qualitatively different for other M_{bh} values.

from massive stars to be produced pre-explosively and to survive their SNII explosions, as discussed in Section 4. As in this case, the conclusions concerning the efficiency of the pre-explosion p-process are sensitive to the modeling of convection.

At this point, the question arises of the possible contribution of PCSN to the galactic p-nuclide content. It cannot be answered quantitatively at this stage, especially because the frequency of occurrence and yields of these events versus metallicity is unknown. Obviously, and except perhaps in the very young Galaxy, such stellar explosions cannot be frequent. This statement relates to the likely increasingly severe mass losses the considered very massive stars experience with increasing metallicities. As a result of these mass losses, it may be that no PCSN exists after all for Z in excess of some critical value which could well be lower than $Z_\odot$! From the PCSN infrequency, it is also expected that their yields would be quite inhomogeneously spread in the Galaxy. In this respect, it has to be recalled that it is totally unknown how the p-nuclides are distributed outside of the solar system, and if the solar p-nuclide content is representative of the galactic content.

8. The p-process in Type I supernovae

8.1. The case of the Type Ia explosions

Supernovae which do not show hydrogen lines, but exhibit strong silicon features, in their spectra near maximum light are named Type Ia supernovae (SNIa). In a ‘canonical’ view, they are believed to be the result of the total disruption of the carbon–oxygen white dwarf (WD) member of a binary star which accretes material from its companion at a suitable rate to the point where its mass reaches a value close to the so-called Chandrasekhar limit ($M_{Ch} \approx 1.4\ M_\odot$).[4] At this point, the WD is subjected to a hydrodynamical burning triggered by the thermonuclear runaway of carbon, and a supernova explosion ensues. It has to be noted, however, that SNIa do not form a fully homogeneous

[4] The Chandrasekhar mass is the limiting mass of a configuration the mechanical equilibrium of which is obtained through the compensation of the gravitational forces by the pressure from fully degenerate electrons.

class of events. This may imply a certain diversity in the thermonuclear explosion regimes and/or in the progenitor stars whose very nature is still in doubt, as it cannot be inferred from any available observation.[5] This fact, combined with the often questioned astrophysical plausibility for a C–O WD of initial mass probably not exceeding about 0.6 $M_\odot$ to reach its critical mass M_{Ch} through accretion, has led to the development of variants to the canonical SNIa model. They include the thermonuclear explosion of oxygen-neon WDs or the merging of two WDs. Another scenario envisions a C–O WD capped with a helium layer accreted by a companion, and exploding as the result of a hydrodynamical burning before having reached the Chandrasekhar limit. This scenario, to be dealt with in more detail in Section 8.3, is referred to as a 'sub-Chandrasekhar-mass' supernova, which may exhibit properties which cannot match easily the observed properties of typical SNIa events.

Over the years, SNIa have attracted much attention from observers and model builders. The special interest for these stellar explosions has been boosted further by the announcement that distant SNIa appear to be fainter than their local counterparts. This observation may have far-reaching cosmological implications and forces to take a new look at the distant Universe, and concomitantly to wonder about what one really understands about the assuredly complex physics of the SNIa. Recent and extended reviews have been devoted to the SNIa observed properties and models [160], and more specifically to their cosmological implications [162]. We just limit ourselves here to a short presentation of some aspects of the physics of the canonical SNIa scenario which have a bearing on the p-process.

Until the mid-nineties, SNIa have been mostly described in a one-dimensional (1D) spherically symmetric approximation (see [160] for references). This framework is unable to provide a satisfactory description of the intricate aspects of the intrinsically multi-dimensional features of the thermonuclear burnings which are expected to develop in M_{Ch}-mass C–O WDs. This is why some recent attempts to develop multi-dimensional (2D, and even 3D) simulations have been conducted (see [160,161] for references). Still, the 1D models remain a privileged framework for extended nucleosynthesis network calculations as those required for the p-process modeling.

Owing to the strong temperature dependence (of the order of T^{12} at $T \approx 10^{10}$ K) of the rates of the nuclear reactions involved in the WD thermonuclear explosion invoked by the canonical model, the nuclear burning in the course of the explosion is confined to microscopically thin layers. These propagate either diffusively as subsonic deflagrations ('flames') or by shock compression as supersonic detonations, both modes being hydrodynamically unstable to spatial perturbations. The first hydrodynamical simulations of an exploding M_{Ch}-WD have assumed that a detonation wave starts the thermonuclear combustion. This regime is by now considered to be unlikely to develop in the relevant astrophysical conditions, and may instead be subject to self-quenching. Another argument against this scenario is the impossibility to reconcile the observed SNIa spectral features with the prediction that almost the entirety of the initial WD C–O material is burned into iron-peak nuclei. This is why much effort has been devoted to the highly intricate modeling of the deflagration regime. The subsonic thermonuclear flame characterizing the deflagration regime may ignite either in central regions or in peripheral WD shells (or spots in the context of multi-dimensional simulations). The location of this ignition influences substantially the explosion energetics and nucleosynthesis. Once ignited, the flame is subjected to various instabilities and continues to propagate through the WD until

[5] The detection of a small amount of hydrogen in early SNIa spectra might, however, help constraining the nature of their progenitors [159].

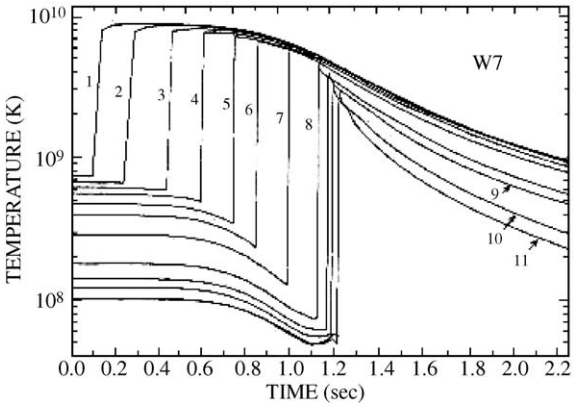

Fig. 42. Temperature evolution of selected layers of WDs subjected to a turbulent carbon deflagration. The WD mass at ignition of the thermonuclear runaway is close to the Chandrasekhar mass (1.378 $M_\odot$). The zones labelled 1 to 11 correspond to masses (in $M_\odot$) of 0.0011, 0.009, 0.036, 0.10, 0.25, 0.41, 0.70, 1.00, 1.12, 1.17 and 1.23. For each layer, the temperature increases abruptly when it is hit by the deflagration front, and decreases as a result of its expansion. Only the outer layers 9 to 11 experience peak temperatures $T_m \lesssim 4 \times 10^9$ K (from [163]; model W7).

it is quenched by expansion or transforms into a detonation wave, this situation being referred to as a delayed detonation. Many 1D simulations of this regime have been found to provide excellent fits to SNIa spectra and light curves. A different variety of delayed detonations, named 'pulsational delayed detonations', has also been identified in 1D simulations. They are predicted to occur when the initial turbulent deflagration phase fails to release enough energy to disrupt the WD, which instead starts pulsating. A detonation could be triggered at a time close to the maximum compression phase of the pulse. This scenario is not found, however, in multi-dimensional simulations.

As said above, the nucleosynthesis accompanying the deflagration or delayed detonation regimes has been studied in detail in 1D simulations only. The corresponding yield predictions are highly uncertain, as they are found to depend strongly (i) on the accretion rate. This, in turn, is a function of the precise characteristics of the progenitor binary system and of the nature of the WD companion, which are unknown observationally and theoretically, (ii) on the deflagration flame speed, as well as (iii) on the critical densities for the transition from deflagration to detonation in delayed detonation scenarios. Neither flame speeds nor critical densities can be estimated from first principles in the considered models, and just have the status of free parameters (they are in fact also subjected to large uncertainties in available multi-dimensional modelings).

Roughly speaking, the carbon thermonuclear runaway triggering a deflagration or a delayed detonation evolves into the explosive burnings of Si, O–Ne and C when moving from the innermost to the outermost WD layers. Only the external zones where C burns explosively experience the proper temperature conditions for the development of the p-process, the other ones reaching too high values. Some relevant temperature profiles are depicted in Figs. 42 and 43.

Following some exploratory parametric calculations by [165], the p-process has been studied on grounds of SNIa simulations. In particular, [23] base their nucleosynthesis calculations on the thermodynamic conditions encountered in the outermost 0.05 $M_\odot$ layers of the delayed detonation model of [164] (Fig. 43). The total p-nuclide yields from these layers normalized to the solar abundances

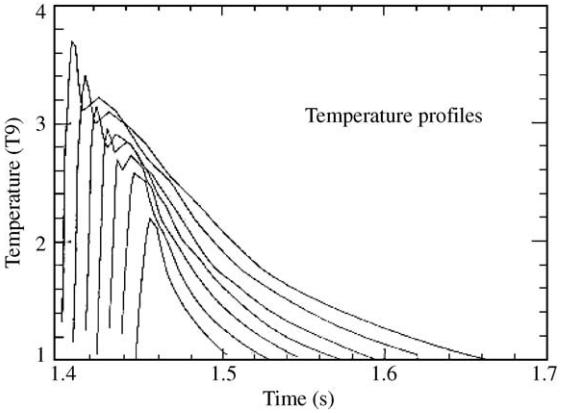

Fig. 43. Same as Fig. 42, but for a delayed detonation. The WD at ignition has a mass of 1.42 $M_{\odot}$. Temperatures are represented for some of the 15 outer zones which comprise about 0.05 $M_{\odot}$, and which are suitable PPLs (from [164]; model N21).

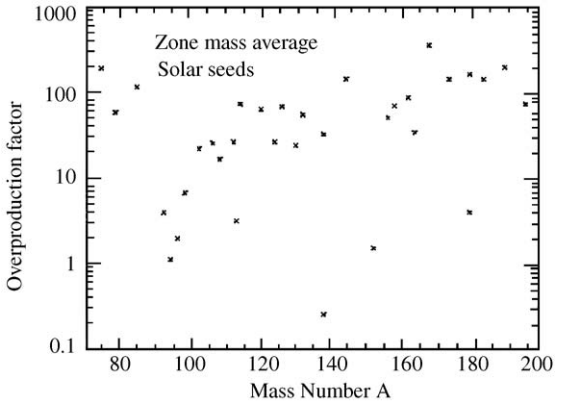

Fig. 44. Overproduction (with respect to solar) of the p-nuclides in the delayed detonation model N21 of [164] (see Fig. 43). The seed distribution is assumed to be solar (from [23]). The approximate reaction rates on heavy targets used for these calculations are the same as in [129]. This is also true for the reaction network, except that neutron and proton captures are duly taken into account.

are displayed in Fig. 44 for a solar distribution of seeds, or in Fig. 45 when use is made of a seed distribution considered to be representative of the s-process developing during the thermal pulse phase of asymptotic giant branch (AGB) stars (for a more recent calculation in $Z = Z_{\odot}$ AGB stars, see e.g. [153]). In this case, the s-nuclides with mass numbers $A \gtrsim 90$ have abundances that can exceed the solar ones by factors as high as 10^3–10^4. This s-process enhancement translates directly into an increase in the p-nuclide overproduction factors. This (expected) high sensitivity of the p-process efficiency to the assumed seed distribution makes predictions of the p-nuclide yields from delayed detonations quite unreliable, as the s-process content of the material accreted by the WD has never been calculated self-consistently. It is just estimated that this material is polluted by an

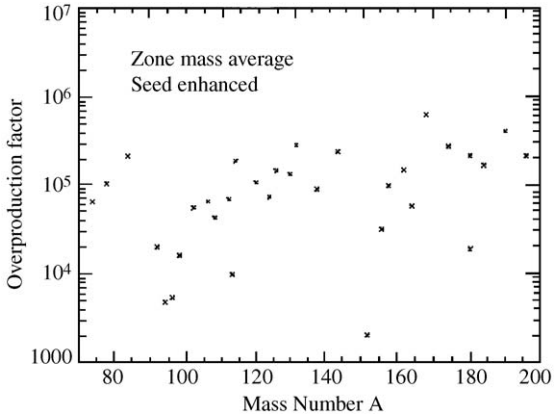

Fig. 45. Same as Fig. 44, but the seed distribution is assumed to be representative of the s-process developing during the thermal pulse phase of AGB stars (from [23]).

AGB s-nuclide donor, or it is speculated that it may be the site for some s-processing prior to the thermonuclear runaway. Uncertainties in the p-nuclide yields originating from those affecting the seed distributions are widespread. They are indeed encountered for SNII explosions, as discussed in Section 6.1, as well as in the case of deflagrations (see below) or of sub-Chandrasekhar WD explosions (see Section 8.3). Further problems of course arise from the uncertainties in the very modeling of the delayed detonations mentioned above.

Keeping these uncertainties in mind, it appears from Figs. 44 and 45 that, roughly speaking, the overall relative distribution of the p-nuclides emerging from the considered delayed detonation model is not drastically different from the one predicted for the SNII (Section 5) or for the PCSN events (Section 7). In particular the p-isotopes of Mo and Ru remain underproduced, this conclusion being at variance with the hope originating from the early parametrized calculations of [165]. This difference results from the overestimate of the role of proton captures by the parametrized approach, and concomitantly of the synthesis of the light p-nuclides. The delayed detonation also shares the underproduction of ^{113}In, ^{115}Sn, ^{138}La and ^{152}Gd with the SNII and PCSN massive star explosions. In contrast, the delayed detonation appears unable to produce enough ^{180}Ta^{m}, a situation which differs markedly from the one encountered in SNII (Section 6.3). Note that no contribution of the ν-process to ^{138}La or ^{180}Ta^{m} is considered here. In fact, it is likely to be inefficient in delayed detonations.

For the purpose of this review, the p-processing in SNIa has been complemented with new calculations conducted on grounds of the turbulent deflagration model W7 of [163], the outer zones of which appear to be suitable PPLs (Fig. 42). Fig. 46 presents the total p-nuclide yields calculated with the use of the standard reaction network defined in Section 3.6 and with two different s-seed distributions, the proper one being largely unknown at this time, as in the case of the delayed detonation model discussed above. The conclusions one can derive from the inspection of Fig. 46 are quite similar to those resulting from the consideration of massive star explosions (Figs. 31 and 40) or from turbulent deflagration scenarios (Figs. 44 and 45). This concerns in particular the general pattern of the p-nuclide distribution, its high sensitivity to the assumed seed distribution, and the set of underproduced species (esp. ^{92,94}Mo, ^{96,98}Ru, ^{113}In, ^{115}Sn, ^{138}La and ^{180}Ta^{m}). It has of course to be

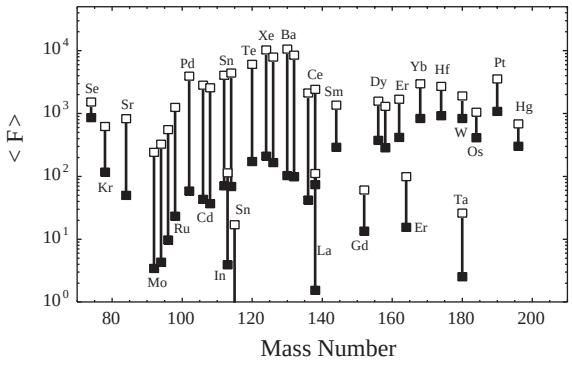

Fig. 46. Abundances of the p-nuclides in the SN Ia deflagration model W7 [163]. The overproduction factors refer to the 0.12 $M_\odot$ of the PPLs (zones between about 1.12 and 1.23 $M_\odot$ in Fig. 42). They are calculated with solar s-seeds (black squares), or with a seed distribution which is representative of the s-process in $Z = Z_\odot$ AGB stars [153] (open squares).

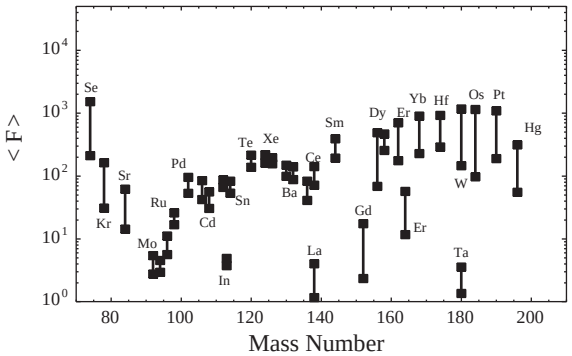

Fig. 47. Impact of the nuclear uncertainties on the p-nuclide overproduction by the SNIa deflagration model W7 [163]. Displayed for each nuclide are the maximum and minimum abundances computed from the p-process calculations performed with the 14 sets of rates obtained from the nuclear input combinations defined in Table 2. Note that the maximum and minimum abundances are not necessarily obtained with the same rate set for all the p-nuclides. A solar s-seed distribution is adopted.

kept in mind that the simulation of deflagrations is extremely intricate, and model uncertainties certainly bring their share to the reliability of the yield predictions.

As in the SNII case, the impact of a change in the nuclear reaction rates on the results displayed in Fig. 46 has been analyzed. The 14 sets of rates defined in Section 3.4 (Table 2) already used to construct Fig. 35 for the SNII nucleosynthesis have been selected again to obtain Fig. 47. It appears that the uncertainties of nuclear origin are larger than average for the 3 lightest and for the $A \gtrsim 160$ p-nuclides. It is also demonstrated that the predicted underabundances cannot be cured by reasonable reaction rate changes.

8.2. The case of the Type Ib/Ic explosions

Type Ib/Ic supernovae (SNIb/c) share with SNIa the absence of hydrogen lines in their spectra at maximum light. They also lack the strong Si features which are characteristic of the SNIa. The progenitors of these supernovae are generally considered to be massive stars of the Wolf–Rayet (WR) type having lost their hydrogen envelope either through severe winds, or through mass transfer onto a companion star in a close binary system.

Single WR stars are generally considered to represent a normal phase in the evolution of O-type stars with initial masses $M_{\rm ZAMS}$ in excess of some critical mass $M_{\rm crit}$, the value of which depends on the metallicity Z, on the adopted mass loss rates, as well as on rotation (e.g. [166,110] for reviews). In absence of rotation, $M_{\rm crit}$ may be as low as about 25–30 $M_\odot$ for $Z = 0.04$ (twice $Z_\odot$), and reach 60–80 $M_\odot$ for $Z = 0.001$. During their non-explosive evolution, stars going through the WR phase are expected to experience in their central regions the sequence of nuclear burning stages (from the combustion of H to Si burning) that is typical of massive stars (see Fig. 23). Mass loss governs the evolution of the WR surface, which starts being enriched with the products of H burning before showing the He-burning ashes if the surface stripping is extensive enough. In contrast, the products of subsequent burning phases are not uncovered, as the post-He burning evolution is too rapid for a significant amount of matter to be lost between the C and Si burning stages. The stellar wind also determines the pre-supernova mass of the stars, which are made of C- to Si-burning zones overlaid by a He-envelope. These structures are to some extent reminiscent of the He stars adopted by [24] (Section 5), and are referred to here as 'He star remnants'. Their masses calculated by [167] largely overlap the masses of the He stars studied by [24].

In close binary systems, it is expected that a fraction of the $M < M_{\rm crit}$ O-type stars can transform into WR stars through Roche lobe overflow, their companion being either a massive OB-type companion, or a compact object (see the review by [168]). In addition, the pre-supernova He star remnant would be on average less massive in the binary case than in the single star scenario [169].

The He star remnants resulting from the evolution of single or binary stars are expected to experience an eventual supernova explosion of the CCSN type, just as the one ending the evolution of massive stars (Section 4.1) [167,169]. No calculation of the p-process accompanying these explosions has been carried out to-date (only the s-seed distributions emerging from the burning of He have been computed in detail [25]). In view of the fact that several of the exploding He star remnants have masses in the range of the He stars explored in Section 5, one may consider as a first-order approximation that the p-nuclide yields from a SNIb/c explosion of a He star remnant of given mass are not drastically different from those from a SNII explosion of a He star of the same mass. However, as emphasized by [167,169], the equality of the He star remnant and of the He star masses does not guarantee the identity of the structure and chemistry of the pre-supernova configuration, and consequently of the explosion and of its yields. Considering the sensitivity of the p-process flows to the exact thermodynamic history of PPLs in massive stars (Section 5), detailed calculations are awaited before drawing strong conclusions on the p-nuclide yields from SNIb/c events.

8.3. The case of the sub-Chandrasekhar white dwarf explosions

Several scenarios suggest that a variety of close binary stars end up as helium star cataclysmics. Such objects are made of a CO WD with sub-Chandrasekhar mass $M < 1.4\ M_\odot$ (CO-SCWD)

accumulating a He-rich layer at its surface. This accreted He might result from the burning, under certain restrictive conditions, of the hydrogen contained in the material transferred from a companion [170], or from the direct accretion of a He-rich layer transferred from a nondegenerate companion burning He in its core. A probability as high as 0.01 yr^{-1} has been estimated for the formation of the latter systems [171].

Much work has been devoted to the possible outcome of the helium cataclysmics, particularly in relation with the identification of the SNIa progenitors. In spite of some virtues, they are not considered today as the most favored objects which can give rise to these explosions (e.g. the discussion by [160]). It cannot be excluded, however, that they are responsible for some special types of events, depending in particular on the He accretion rate and on the CO-SCWD initial mass (e.g. [171]). Unidimensional simulations of He cataclysmics characterized by suitably selected values of these quantities reach the conclusion that the accreted He-rich layer can detonate. Most commonly, this explosion is predicted to be accompanied with the C-detonation of the CO-SCWD (e.g. [172,173]). In some specific cases, however, this explosive burning might not develop, so that a remnant would be left following the He detonation [174]. Multidimensional calculations cast doubt on the nature, and even occurrence, of the C-detonation in CO-SCWD. It might even well be that the He-ignition is of point-like nature (e.g. [160]).

The possibility of development of the p-process following the detonation of the He-rich material assumed to be accreted directly onto a CO-SCWD has been explored by [175] in the framework of a 1D model of the He detonation of a non-rotating 0.8 $M_\odot$ WD. In short (see [175] for the details of the model), a thermonuclear runaway develops near the base of the He envelope when about 0.18 $M_\odot$ has been accreted. It is triggered by the transformation $^{14}N(e^-,\nu)^{14}C$ of a trace amount of ^{14}N assumed to be left over in the He shell from the CNO cycle [176,173,177]. This triggering works as follows: When the temperature gets high enough, the resulting ^{14}C transforms into ^{18}O through $^{14}C(\alpha,\gamma)^{18}O$, this α-particle consumption channel competing successfully with the 3α-reaction in the relevant temperature and density regimes. The associated energy release is responsible for the detonation of He. More precisely, two shock waves propagate both inward and outward from the He-ignition shell. The outward-moving He-detonation wave heats the matter to temperatures around 3×10^9 K, and leads to the ejection of about 0.18 $M_\odot$ into the ISM. Fig. 48 displays the temperature history of the detonating He-rich accreted layers. It clearly appears that some of them can reach suitable temperatures ($T \gtrsim 2\times10^9$ K) for allowing the development of the p-process.

The p-process in the accreted material is followed with the reaction network defined in Section 3.6. It involves more nuclides (4000 up to Po) and more reactions (50 000) than in the other scenarios discussed above. This extension is imposed by the specific complexity of the nucleosynthesis associated with the detonation. In fact, the typical p-process flow pattern discussed in Section 1 develops following inroads into the neutron-rich side of the valley of nuclear stability, making the inclusion in the network of a quite large variety of neutron-rich nuclei mandatory. More precisely, the main characteristics of the flow may be summarized as follows. At the start of the detonation, high neutron densities build up following the transmutation by $^{18}O(\alpha,n)^{21}Ne$ of the ^{18}O produced by the burning of ^{14}N that triggers the detonation (see above). Further neutrons are subsequently released by $^{22}Ne(\alpha,n)^{25}Mg$ and $^{26}Mg(\alpha,n)^{29}Si$, ^{22}Ne and ^{26}Mg being produced during the detonation. As a result, neutron concentrations reaching values as high as $N_n \simeq 10^{22}$–10^{23} cm^{-3} are obtained. A weak r-process ensues, as illustrated in Fig. 49. The eventual increase of temperature to $T_9 \gtrsim 1.5$ then induces fast photodisintegrations driving the matter back to the valley of β-stability, and even

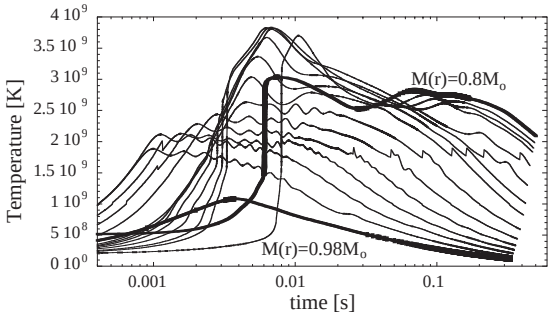

Fig. 48. Temperature history of selected layers of the detonating 0.18 $M_\odot$ of He-rich material accreted onto a WD with a sub-Chandrasekhar mass of 0.8 $M_\odot$. The energetics of the detonation is computed with the help of a network that is larger (188 nuclides linked by 571 reactions) than the ones commonly used in the simulations of He detonation. This extended network is found to be important for a correct prediction of the thermodynamics of the PPLs. The WD is assumed to be made of C and O with mass fractions $X_C = 0.3$ and $X_O = 0.7$. The composition of the accreted material is $X_{He} = 0.98$, $X_C = 0.005$, $X_O = 0.005$, and $X_{^{14}N} = 0.01$ (from [175]).

to its neutron-deficient side. From this point on, two major nucleosynthesis processes take place (see Fig. 49).

In the layers with peak temperatures $2 \lesssim T_{m,9} \lesssim 3$, a typical p-process develops. The associated nuclear flow is dominated by (γ,n), (γ,p) or (γ,α) photodisintegrations, complemented with mainly some neutron captures. For layers with peak temperatures $T_{m,9} \gtrsim 3$, a so-called αp-process [178] takes place, temperatures being high enough to produce large amounts of ^{40}Ca and ^{44}Ti by radiative α-captures. Further α-captures of the (α,p) type proceed, leading to proton mass fractions as high as about $X_p = 6 \times 10^{-3}$. In the considered hot environment, these protons are rapidly captured to produce heavier and heavier neutron-deficient species, making up a kind of 'proton-poor rp-process', in view of the much lower proton concentrations than in the 'classical' rp-process [178]. In this process, some nuclei are produced with proton separation energies that are small enough to experience (γ,p) photodisintegrations which slow down the nuclear flow. However, (n,p) reactions made possible by the high neutron density ($N_n \simeq 10^{19}$ cm^{-3}) revive the flow towards higher-mass nuclei. One might thus talk about a 'proton-poor neutron-boosted rp-process', coined *pn*-process by [175]. The nuclear flow associated with this variant of the rp-process is displayed in Fig. 49. Its main path lies much further away from the proton-drip line than in the classical rp-process, which eases somewhat the nuclear physics problems. This results from the lower proton and non-zero neutron concentrations encountered in the He detonation.

The final envelope composition is displayed in Figs. 50(a) and 51 when the initial abundances of the nuclides heavier than Ne are assumed to be solar. As an interesting prediction associated with the He detonation, we note that almost all the p-nuclei are overproduced in solar proportions within a factor of 3 as a combined result of the p- and *pn*-processes. This includes the puzzling Mo and Ru p-isotopes (see Section 6.1), which are efficiently produced at peak temperatures $T_{m,9} \gtrsim 3.5$. The lighter Se, Kr and Sr p-isotopes are synthesized in layers heated to $3 \lesssim T_9 \lesssim 3.5$, ^{78}Kr being the most abundantly produced in these conditions.

Fig. 50(a) also makes evident that the Ca-to-Fe nuclei are overabundant with respect to the p-nuclei but ^{78}Kr by a factor of about 100, which implies that the considered He detonation cannot be an

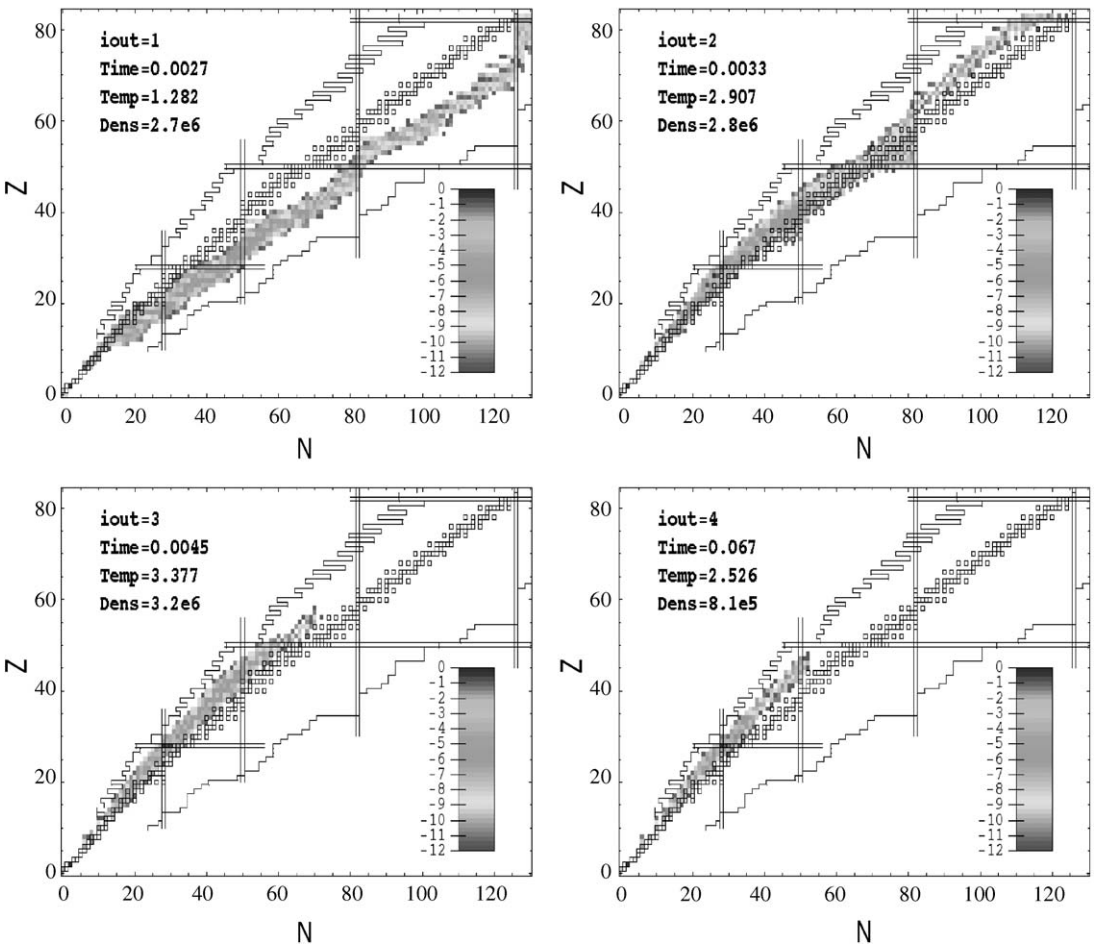

Fig. 49. Snapshots in the nuclidic chart of flow patterns in a detonating He layer accreted onto the 0.8 $M_{\odot}$ SCWD considered in Fig. 48. The selected times and corresponding temperatures or densities are given in the different panels. The stable nuclides are indicated with open squares. The magic neutron and proton numbers are identified by vertical and horizontal double lines. The drip lines predicted by the HFB model of [67] are also shown. The abundances are coded following the grey scales shown in each panel. At early times (top left panel), an r-process type of flow appears on the neutron-rich side of the valley of nuclear stability. At somewhat later times (top right panel), the material is pushed back to the neutron-deficient side rather close to the valley of β-stability. As time passes (two bottom panels), an αp-process [178] and a pn-process [175] develop (see text for details).

efficient source of the bulk solar-system p-nuclides. In order to cure this problem, one may envision enhancing the initial abundance of the s-seeds, which has already seen before to be an essential factor determining the level of production of the p-nuclides (see Section 6.1 and Figs. 44 and 45). Figs. 50(b) and 51 indeed show that an increase by a factor 100 of the s-nuclide abundances over their solar values makes the overproduction of a substantial variety of p-nuclides comparable to the one of ^{78}Kr and of the Ca-to-Fe nuclei. The factor 100 enhancement would have to be increased somewhat if the material processed in the core of the CO-SCWD by a C-detonation were ejected along with

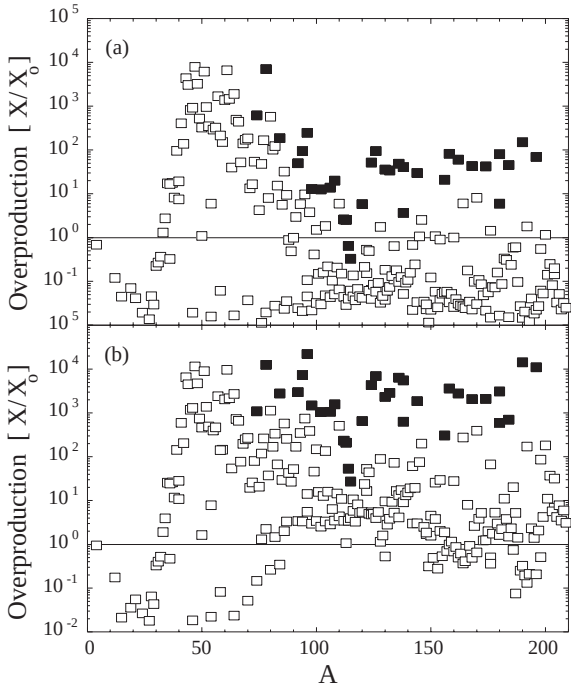

Fig. 50. (a) Final composition versus mass number A of the SCWD envelope ejected as a result of the detonation of its accreted He-rich envelope. The abundances are normalized to the solar values. The initial abundances above Ne are assumed to be solar. Full symbols denote the p-nuclides; (b) Same as (a), but the initial abundances of the s-nuclides are assumed to be 100 times solar (from [175]).

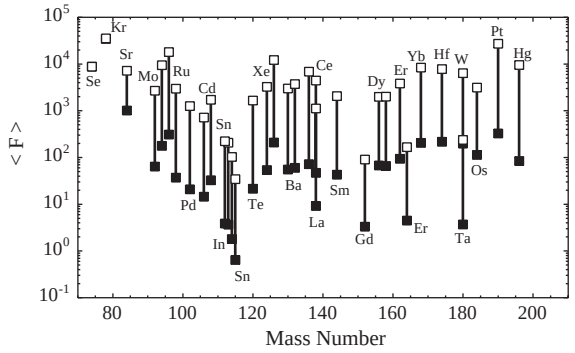

Fig. 51. Same as Fig. 50, but limited for clarity to the overproduction of the p-nuclides only. The full and open symbols correspond to solar s-seed abundances, and to solar seeds increased by a factor 100, respectively.

the envelope. At this point, one essential question concerns the plausibility of the required s-nuclide enhancement. There is no definite answer to this key question. This enrichment of the accreting WD might result from its past AGB history if indeed some of its outer s-process enriched layers

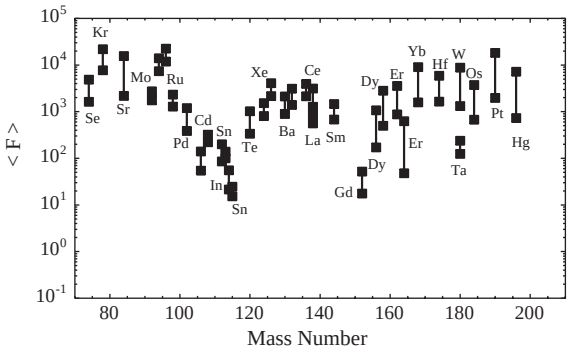

Fig. 52. Impact of the nuclear uncertainties on the p-nuclide overproduction by the He-accreting SCWD model [175]. Displayed for each nuclide are the maximum and minimum abundances computed from the p-process calculations performed with the 14 sets of rates obtained from the nuclear input combinations defined in Table 2. Note that the maximum and minimum abundances are not necessarily obtained with the same rate set for all the p-nuclides. The adopted seed abundances are 100 times solar (see Figs. 50 and 51).

could be mixed convectively with part at least of the accreted He-rich layers before the detonation. Alternatively, the He-rich layer accreted by the WD could be (or become) enriched in s-process elements. Such speculations need to be confirmed by detailed simulations.

Fig. 52 completes the analysis of the production of the p-nuclides in He-accreting SCWD model with an examination of the impact of nuclear uncertainties on the predicted abundances. The various sets of nuclear reactions used here are defined in Table 2, and are the same as the ones already selected to construct Figs. 35 and 47. As in the previous studied cases, the uncertainties resulting from the considered reaction sets do not qualitatively modify the conclusions drawn from the adoption of the standard set of reactions defined in Table 2 (Section 3.4). Let us just note that ^{138}La does not appear from Fig. 52 to be irrevocably underproduced with respect to the neighboring p-nuclides when just considering its thermonuclear synthesis, i.e. without any *v*-process contribution. This situation contrasts markedly with the one encountered for the other astrophysical situations considered above (Section 6.2).

9. The p-process isotopic anomalies and chronometry

As noted in Section 2.2, there is now observational evidence for the existence of isotopic anomalies involving the p-isotopes of Kr, Sr, Mo, Xe, Ba and Sm in various meteoritic materials, including the so-called FUN inclusions and various classes of grains of possible circumstellar origin (e.g. [18–21]). These anomalies manifest themselves as excesses or deficits of the abundances of the p-nuclides with respect to the more neutron-rich isotopes, when comparison is made with the bulk solar mix. In addition, two isotopic anomalies are attributable to the now extinct neutron-deficient radionuclides ^{92}Nb^{g} and ^{146}Sm which have decayed in the meteoritic material where excesses of ^{92}Zr and ^{142}Nd are observed now.

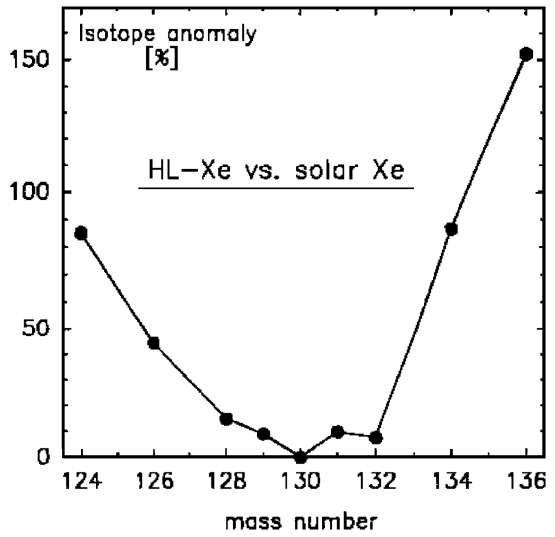

Fig. 53. Typical isotopic pattern of the Xe-HL component carried by circumstellar diamonds (from [179]). The overabundances (in %) are relative to the solar Xe [180]. The two lightest and two heaviest isotopes are of pure p- and r-origin, respectively. Normalisation is to the s-only isotope ^{130}Xe.

9.1. The Xe-HL anomaly

Among the discovered anomalies, one of the most puzzling concerns the so-called Xe-L, which is characterized by excesses of ^{124}Xe and ^{126}Xe and, to a lesser extent, of ^{128}Xe with respect to solar. Remarkably enough, this special Xe is found to be correlated in still enigmatic nanodiamonds of presumed circumstellar origin with Xe-H, the distinguishing characteristic of which is an excess of the r-process isotopes ^{134}Xe and ^{136}Xe that cannot be separated from Xe-L.

A typical Xe-HL isotopic pattern is displayed in Fig. 53. For the lightest p-nuclei, it corresponds to isotopic ratios of $2.1 \lesssim {}^{124}\mathrm{Xe}/{}^{126}\mathrm{Xe} \lesssim 2.4$ and $6.1 \lesssim {}^{128}\mathrm{Xe}/{}^{126}\mathrm{Xe} \lesssim 7.6$ (where the nuclidic symbols denote abundances by number). Its origin has been largely debated over the years. It may well be the result of the mixing before incorporation into the diamonds of normal-type Xe with a special Xe component with even more extreme isotopic compositions than observed. A recent ion-implantation simulation involving the laboratory irradiation of terrestrial diamonds of similar sizes as the presumed circumstellar nanodiamonds with a mixture of noble gases including Xe [181] lends support to this interpretation. It remains to be seen if the specific Xe-HL composition may result from a special nucleosynthetic process. A parametrized scenario involving a combination of hydrostatic and explosive p-process in massive stars has been constructed by [182]. The fully ad hoc character of this analysis does not provide, however, a convincing answer to the question of the origin of Xe-L.

Table 4 gathers the ^{124}Xe/^{126}Xe and ^{128}Xe/^{126}Xe abundance ratios predicted by several of the models reviewed in the previous sections. In all but the third row, the ranges of values translate nuclear uncertainties. They result from the adoption of the reaction rates obtained from the 14 sets of nuclear inputs of Table 2 (Section 3.4). The data of the third row correspond instead mainly to the

Table 4
The $^{124}Xe/^{126}Xe$ and $^{128}Xe/^{126}Xe$ ratios predicted in different p-process sites

Model	$^{124}Xe/^{126}Xe$	$^{128}Xe/^{126}Xe$
SNII 25 $M_\odot$ PPLs [106]	0.79–1.40	2.89–3.75
SNII 25 $M_\odot$ PPLs + envelope [106]	0.89–1.30	13.0–15.7
SNII 15 $M_\odot$–25 $M_\odot$ [124]	0.34–1.45	4.92–26.9
SNIa W7 with solar seeds [163]	0.94–1.51	1.33–1.69
SNIa W7 with AGB seeds [163]	0.78–1.59	1.80–2.84
CO-SCWD with seeds 100 times solar [175]	0.24–0.50	0.20–0.46

In all but row 3, the ranges of values result from the adoption of the reaction rates obtained from the 14 sets of nuclear inputs of Table 2 (Section 3.4). The data of row 3 correspond instead mainly to the dependence of the abundance ratios on the stellar mass for the series of models of [124]. They also include the impact of uncertainties in the rates of nuclear reactions on light targets (up to Si). The isotopic ratios of the second row are estimated by taking into account a full mixing of the PPLs with the H- and He-rich envelope.

dependence of the abundance ratios on the stellar mass in the $15 \leqslant M \leqslant 25\ M_\odot$ range. They also include the impact of uncertainties affecting the rates of nuclear reactions on light targets (up to Si). A confrontation between the observed abundance ratios and the predictions leads to the following conclusions:

(1) The calculated $^{128}Xe/^{126}Xe$ ratios differ quite significantly from the observations, except possibly in the SNII case, at least when the PPL Xe is allowed to be contaminated with the Xe contained in the overlying envelope (rows 2 and 3 of Table 4). This situation results from the fact that the PPLs are not efficient producers of ^{128}Xe, classically considered as a s-only isotope. More precisely, some ^{128}Xe is synthesized by the p-process in a fraction of the SNII PPLs, but this production is compensated by a partial destruction of the initially present ^{128}Xe seeds of s-process origin;
(2) The predicted $^{124}Xe/^{126}Xe$ ratios are lower than observed in all cases. One way to cure this discrepancy would be to assume an incomplete mixing of the PPLs. Only the PPLs with peak temperatures in the $2.6–2.9 \times 10^9$ K can indeed generate $^{124}Xe/^{126}Xe$ ratios in excess of the observed one (values up to 4 can be reached). On top of the fact that the assumption of a restricted mixing is of doubtful astrophysical plausibility, it would also make impossible to explain the $^{128}Xe/^{126}Xe$, for which an extended mixing with the envelope is required instead, as discussed just above;
(3) The s-only isotope ^{130}Xe cannot be produced in the SNII PPLs. Its initial seed abundance is just lowered by the p-process. Dilution of the PPLs within the much more massive envelope is thus consistent with the absence of ^{130}Xe anomaly (Fig. 53).

In conclusion, none of the p-process scenarios considered to-date is able to account for Xe-HL in a scenario calling for the incorporation into nanodiamonds of a mixture of normal-type and abnormal Xe components.

A scenario of a different nature has been envisioned by [183] to explain the Xe-HL pattern. It calls for a separation of the heavy Xe isotopes from their unstable iodine and tellurium progenitors on timescales of a few hours after termination of an otherwise ‘regular’ r-process. Such a separation

Table 5
^{92}Nb/^{92}Mo and ^{146}Sm/^{144}Sm ratios of abundances in number taken over the entire stars responsible for the p-process in different scenarios

Model	^{92}Nb/^{92}Mo	^{146}Sm/^{144}Sm
SNII 25 $M_\odot$ [106]	6.2×10^{-4}–1.6×10^{-3}	0.15–0.42
SNII 15 $M_\odot$–25 $M_\odot$ [124]	4.6×10^{-4}–4.0×10^{-2}	0.01–0.21
SNIa W7 with solar seeds [163]	1.2×10^{-2}–4.0×10^{-2}	0.35–0.84
SNIa with AGB seeds [163]	1.4×10^{-2}–5.4×10^{-2}	0.30–0.70
SNIa N21 with AGB seeds [23,164]	10^{-2}	0.040
CO-SCWD with seeds 100 times solar [175]	7.4×10^{-4}–3.2×10^{-3}	0.85–2.45

The ranges of values of rows 1, 3, 4 and 6 result from the adoption of the reaction rates obtained from the sets of nuclear inputs of Table 2 (Section 3.4). For Nb, the 14 sets considered there are taken into account, while sets 2,7,10 and 11 are excluded in the Sm case. They indeed do not reproduce the recently measured ^{144}Sm(α,γ)^{148}Gd cross section (Fig. 20). The data of row 2 indicate mainly the dependence of the abundance ratios on the stellar mass for the series of models of [124]. These values, as well as those displayed at row 5 (model N21) are based on different nuclear physics inputs than the other cases.

mechanism of the light Xe isotopes from their unstable Ba progenitors might also help accounting for Xe-L. Possible mechanisms for the requested separation include precondensation, loss from the diamond grains upon β-decay of the precursors, or charge state separation. In this picture, the resulting Xe pattern depends drastically not only on the p-process nuclear flow in the region of relevance, but also upon the timescales on which the separation mechanisms can operate in supernova environments. These timescales being unknown, it is impossible to draw firm conclusions on the real merits of the proposed scenario.

To close this section, let us mention that the Kr-L component which might accompany Xe-L in diamonds (see [181] and references therein; Section 2.2) does not provide real constraints on the p-process models. The calculated yields of ^{78}Kr relative to those of the s-nuclide ^{80}Kr are indeed too uncertain for this purpose at the level of the observed anomalies. In this respect, Xe-L with its two p-nuclides offers a much better opportunity.

9.2. $^{92}Nb^{g}$ in the early solar system

Meteoritic studies now provide evidence for the existence in the early solar system of the p-process radionuclide ^{92}Nb^{g} (electron capture half-life $t_{1/2} = 3.6 \times 10^7$ yr). The exact level of this contamination remains, however, controversial. The analyses of different meteorites lead to abundance ratios $(^{92}Nb^{g}/^{92}Mo)_0$ at the start of condensation in the solar system of the order of 2×10^{-5} [184,185], while the values derived from the study of Ca–Al-rich inclusions are as high as about 2×10^{-3} [186,187].

Table 5 gives a summary of the predicted ^{92}Nb/^{92}Mo production in various p-process sites. Ratios ranging from about 5×10^{-4} to 0.05 are calculated depending on the astrophysics site, or even the model star. The largest values of the order of 0.01 to 0.05 are predicted for the different SNIa models reviewed in Section 8.1. The only exception comes from the 20 $M_\odot$ star of [124]. This model is quite peculiar in many respects, and gives an abundance ratio as high as 0.04, all the other massive star models leading to values smaller than 0.005.

Taken at face value, the levels of ^{92}Nb production reported in Table 5 could at best account for the reported low $(^{92}Nb^{g}/^{92}Mo)_0$ value only. This conclusion has to be taken with some care, however. It should indeed be kept in mind that none of the present models, except the CO-SCWD one with a suitable choice of seed s-process abundances (Section 8.3), is able to account for the solar abundances of the Mo and Ru p-isotopes. In such a situation, one has to acknowledge that the evaluation of the ^{92}Nb/^{92}Mo production ratio is far from being put on safe grounds. The seed s-nuclide abundances and the effect of neutrino interactions are two identified sources of uncertainties. As an illustration, the adoption of the upper limit of the ^{22}Ne$(\alpha,n)^{25}$Mg rate reported by the NACRE compilation [103] (this high rate is excluded by recent experiments, however; see Section 6.1) would bring ^{92}Nb/^{92}Mo up to about 0.1. The consideration of the neutrino-induced transmutations discussed in Section 6.2 would typically increase the ratio by a factor of about two.

Clearly, the controversial early solar system $^{92}Nb^{g}$ abundance combined with the substantial uncertainties of nuclear physics and astrophysics natures which remain in the evaluated ^{92}Nb/^{92}Mo production ratios make by far premature any attempt, like the one of [184], to develop a meaningful ^{92}Nb-based p-process chronometry.

9.3. ^{146}Sm: a short-lived p-process chronometer?

The study of ^{146}Sm (α-decay half-life $t_{1/2} = 1.03 \times 10^8$ yr) as a potential p-process chronometer has been pioneered by [188]. This work has triggered a series of meteoritic, nuclear physics and astrophysics investigations, which have helped clarify many aspects of the question. In particular, the early uncertainties on the amount of ^{146}Sm that has been injected live into the early solar system have been reduced greatly through high quality measurements of the ^{142}Nd excess resulting from the in situ ^{146}Sm α-decay observed in many types of meteorites, and even in planetary bodies (Earth, Mars) [189–192]. More specifically, it is concluded that $(^{146}Sm/^{144}Sm)_0 \approx 0.007$, ^{144}Sm being the stable Sm p-isotope. One can attempt building up a p-process chronometry on this value if the corresponding isotopic production ratio can be estimated reliably enough at the p-process site.

In fact, the production ratio $P \equiv {}^{146}Sm/{}^{144}Sm$ has long remained by far too uncertain to give ^{146}Sm the status of a reliable chronometer (see [50] for some early references). This unfortunate situation relates in part to astrophysical problems, and in part to nuclear physics uncertainties, especially in the ^{148}Gd$(\gamma,\alpha)^{144}$Sm to ^{148}Gd$(\gamma,n)^{147}$Gd branching ratio (e.g. [193,194]). The prediction of this ratio has recently gained increased reliability. As discussed in Section 3.4 (see Fig. 20), this follows from the direct measurement of the ^{144}Sm$(\alpha,\gamma)^{148}$Gd cross section down to energies close to those of direct astrophysical interest, complemented with an improved nuclear reaction model [50]. The resulting ^{144}Sm$(\alpha,\gamma)^{148}$Gd rate is about 5–10 times lower than previous estimates [100,195] in the temperature range of relevance for the production of the Sm p-isotopes. By application of the reciprocity theorem, the rate of the reverse ^{148}Gd$(\gamma,\alpha)^{144}$Sm reaction of direct astrophysical interest is reduced accordingly. This implies a lowering of the ^{144}Sm production, and favors concomitantly the ^{146}Sm synthesis through the main production channel ^{148}Gd$(\gamma,n)^{147}$Gd$(\gamma,n)^{146}$Gd$(\beta^+)^{146}$Sm. The net effect of the revised ^{148}Gd$(\gamma,\alpha)^{144}$Sm rate is thus an increase of the P values.

Other nuclear problems add to the uncertainty in the evaluation of P. As noted above, this concerns in particular the ^{148}Gd$(\gamma,n)^{147}$Gd reaction, for which no experimental information can be foreseen in a very near future in view of the unstable nature of ^{147}Gd ($t_{1/2} \approx 38$ h). A limited analysis of the sensitivity of P to this rate has been conducted by [50], and is extended here by

a coherent treatment of all the uncertainties affecting the theoretical reaction rates, as discussed in Section 3.4.

Table 5 provides the P values for different p-process sites. In all but the second row, the displayed ranges result from the use of reaction rates obtained from the restricted ensemble of nuclear inputs of Table 2 which lead to a satisfactory reproduction of the experimental ^{144}Sm(α,γ)^{148}Gd cross sections (Fig. 20). As a result, sets 2, 7, 10 and 11 are excluded. The data of the second row originate instead mainly from the P-dependence on the stellar mass predicted by [124] in the $15 \leqslant M \leqslant 25$ M$_\odot$ range.

It is seen from Table 5 that both astrophysics and nuclear physics concur significantly to make the predicted P vary in a quite large range of values. On the astrophysics side, SNII models with different initial masses yield values in the quite wide $0.01 \leqslant P \leqslant 0.2$ range. SNIa explosions of the deflagration type (model W7; Section 8.1) lead to higher P ratios than the SNII, values between about 0.3 and 0.8 being reached. This is at complete variance with the delayed detonation predictions based on model N21, for which P is at least 10 times lower than for W7. In contrast, the He-detonating CO-SCWD case (Section 8.3) provides the highest predicted P ratios, values in excess of 1 or 2 being possibly obtained. On top of the diversity of P predictions relating to the variety of astrophysics sites, it has to be kept in mind that all the considered SN models suffer from more or less large uncertainties, among which multi-dimensional effects or departures from spherical symmetry belong to the most intricate.

The range of predicted P values is enlarged further when nuclear uncertainties are taken into account. Table 5 indicates that P may change typically by a factor of about 2–3 in a given site as a result of the nuclear input variations summarized in Table 2. Further nuclear problems conspire to increase the unreliability of the P ratio predictions. This is exemplified by the impact of the uncertainties in the ^{12}C(α,γ)^{16}O rate (Section 5.3). As mentioned by [50], P reaches a value as high as 2.1 when the 25 M$_\odot$ SNII model of [106] is calculated with a ^{12}C(α,γ)^{16}O rate decreased by a factor of about 2.3, all other inputs being kept unchanged.

In view of the diversity of the predictions of P and of the associated uncertainties, it is without doubt highly risky, if not impossible, to construct a meaningful p-process chronometry based on ^{146}Sm. In spite of this, many attempts in this direction can be found in the literature (e.g. [184,50]). We do not want to dwell upon this exercise here.

10. Summary and prospects

This review demonstrates that the relatively small number of papers devoted to the p-process clearly does not do justice to the astrophysics and nuclear physics richness of this mechanism called for synthesizing the stable neutron-deficient isotopes of the elements beyond iron that are observed in the solar system.

The survey of the limited literature on the subject and an ensemble of original results presented here for the first time lead to the conclusion that a large variety of astrophysics sites may be considered as potential active contributors to the solar p-nuclides through thermonuclear transmutations. They include massive stars in their pre-supernova or Type II supernova phases, as well as at their Type Ib/Ic stage if they have lost their hydrogen envelope as the result of strong winds prior to their explosion. Even (still putative non-zero metallicity) very massive stars experiencing a pair-creation supernova explosion might bring their share at a level that is not possible to assess quantitatively

at this time. Chandrasekhar-mass white dwarfs exploding as Type Ia supernovae in binary systems through deflagration or delayed detonation can also synthesize p-nuclides, just as He-detonating sub-Chandrasekhar-mass white dwarfs.

At this point, the reader may note that no reference is made in this review to some thermonuclear models that have been discussed in the literature as possible p-nuclide synthesis agents. This neglect concerns in particular models that, in our views, have not reached a 'mature' enough stage of development and/or have a limited astrophysical plausibility. This is the case for the so-called rp-process developing in the H-rich material accreted at the surface of a neutron star, or even of a black hole. There has been some claim [196] that this type of transmutations could produce a substantial amount of the light p-nuclides, and could in particular explain the solar system content of the p-isotopes of Mo and Ru, the synthesis of which raises a problem (Section 6.1). One of the major difficulties of this scenario lies in the likely negligible quantity of processed material that could be ejected by the considered neutron star and, in addition, contaminate the solar system. This shortcoming has been acknowledged recently by [197]. One has to add to this difficulty that the p-nuclide abundance distribution predicted by [197] is strongly non solar through, in particular, a marked ^{102}Pd overproduction. Finally, one has to stress that all these rp-process predictions are based on simplistic one zone models that certainly do not do justice to the high complexity of the neutron star surface thermonuclear processing. On the other hand, this review was in its final stage of completion when we have been aware of a calculation of the production of the p-nuclides in a supercritical accretion disk around a $1.4\,M_\odot$ compact object [198]. Such a disk is assumed to form from the material that fails to be ejected by a $20–40\,M_\odot$ supernova, and eventually falls back with a supercritical accretion rate onto the forming central object. It is estimated by [198] that the nuclear processing of the disk material could produce p-nuclides with an abundance distribution that is reminiscent of the one emerging from the lower mass SNII considered in Section 5.2. Under some ad hoc assumptions, a substantial ^{92}Mo production is even predicted. The contribution of the processed disk material to the solar system p-nuclides is expected to be significant if several percent of the disk matter are ejected via winds and/or jets. At its present stage, the model is simplified in various respects and involves some fine tuning and several, sometimes quite ad hoc, assumptions. It is worth, however, further exploration.

The calculations conducted in 'realistic' models for the various sites reviewed here indicate, roughly speaking, that they may all provide yields enriched with a suite of p-nuclides at a level that is compatible (within a factor of 3 or so) with the solar values. One has to acknowledge that this conclusion can be reached only through some ad hoc assumptions in some situations, and that the ensemble of satisfactorily produced p-nuclides is somewhat more extended in some cases than in others.

The relative success of the p-process calculations relying on detailed stellar models does not have to hide some puzzling problems raised by specific cases, the most publicized ones concerning ^{92,94}Mo, ^{96,98}Ru and ^{138}La. Section 6.1 discusses the possibility that the underproduction of the p-isotopes of Mo and Ru in SNII explosions is in fact due to some misrepresentation of the production in the He-burning core of massive stars of the s-nuclide seeds for the p-process. The modeling of the s-process in these conditions indeed faces some nuclear physics and astrophysics uncertainties which are not always appreciated at their true value. An increase of the $^{22}\mathrm{Ne}(\alpha,\mathrm{n})^{25}\mathrm{Mg}$ neutron production rate could help solving the underproduction of the Mo and Ru p-isotopes, but the validation of this possibility necessitates further nuclear physics laboratory efforts. Helium-detonating

sub-Chandrasehkar-mass CO white dwarfs could be suitable ^{92,94}Mo and ^{96,98}Ru producers at least if the seed s-nuclides for the p-process are enhanced with respect to typical solar abundances in the material experiencing the detonation (Section 8.3). As far as ^{138}La is concerned, Section 6.2 demonstrates that SNII explosions could well be suitable sites for the production of this rare odd–odd nuclide mainly through ν_e-captures by ^{138}Ba. Exploding sub-Chandrasekhar-mass CO white dwarfs might also be significant ^{138}La producers (Section 8.3). The other rare odd–odd nuclide ^{180}Ta^{m} has been shown years ago to be a natural product of the p-process in SNII explosions, a situation that is too often incorrectly appreciated in the literature. New results presented in Section 6.3 confirm that this is a robust conclusion. Charged current ν_e-captures on pre-existing ^{180}Hf could efficiently complement the thermonuclear ^{180}Ta^{m} production. Some calculations have also suggested that it could be made by the s-process in AGB stars. This possibility remains controversial at this time. Another quite puzzling case which does not attract much attention is ^{113}In. It does not appear to be efficiently produced in the p-process scenarios reviewed here, and no other source has been identified to-date.

A detailed interpretation of the meteoritic isotopic anomalies involving p-nuclides still eludes us to a large extent. This concerns in particular the Xe-HL case. It is also concluded that no reliable p-process chronometry can be built yet on the p-radionuclides ^{92}Nb^{g} or ^{146}Sm in view of the uncertainties still affecting their production in each of the considered p-process sites and of the possible variations of their yields from one site to the other.

At this point, it is of interest to remind of some items the study of which would help putting the p-process modeling on safer grounds. On the astrophysics side, let us cite

(1) a more reliable estimate of the s-nuclide seeds for the p-process in massive stars (including e.g. the effect of rotation) and in the material accreted by white dwarfs with (sub-) Chandrasekhar mass prior to their explosion. This question relates directly to a good knowledge of the rate of the key neutron production reaction ^{22}Ne$(\alpha,n)^{25}$Mg;
(2) some progress in the description of convection in advanced stages of the evolution of massive stars, and in particular in their O–Ne layers. As stressed in Section 4.3, the possibility of survival at the explosion stage of at least a fraction of pre-explosively produced p-nuclides remains an uncertain issue;
(3) the modeling of the p-process in massive stars with a quite broad range of metallicities. Yields from such stars are needed to predict the evolution of the p-nuclide content of galaxies;
(4) the exploration of the impact on the p-process (and on many other questions) of the multi-dimensional modeling of the pre-SNII and core-collapse SNII or SNIb/c phases, as well as of the explosion of (sub-)Chandrasekhar-mass white dwarfs. A study of the p-nuclide production in the pre-SNII 2D model of the O-rich layer of a 20 $M_{\odot}$ star sketched in Section 4.3 has been started recently, but the results are too preliminary to be reported here;
(5) the calculation of p-process yields from a variety of Chandrasekhar mass Type I supernova models of the deflagration or delayed detonation types, as well as of sub-Chandrasekhar He-detonation models.

On the more nuclear physics side, and apart from the already mentioned ^{22}Ne$(\alpha,n)^{25}$Mg reaction, it is of substantial importance to predict reliably the rates of thousands of nucleon or α-particle radiative captures and of the inverse transformations. For a long time to come, almost all these data

will have to be provided by theory, but experiments have to help constraining and improving the models as much as possible. On the laboratory side,

(1) efforts have to be pursued in order to measure directly the cross sections of photoreactions near threshold. Data already exist for some (γ,n) reactions, and in particular for ^{181}Ta(γ,n)^{180}Ta of relevance to the production of ^{180}Ta. An interesting extension of this work would be the measurement of the ^{180}Ta(γ,n)^{179}Ta and ^{139}La(γ,n)^{138}La cross sections, this last reaction being directly involved in the synthesis of ^{138}La;
(2) more experiments should have to be conducted at sub-Coulomb energies on (p,γ) captures by (stable) targets beyond the $Z = 50$ shell closure, and especially on (α,γ) by (stable) targets in a broad range of masses, including nuclei heavier than Sm. The latter experiments would be essential for a better modeling of a global α-nucleus optical potential at low energies.

The build-up of such a potential is certainly of key importance for p-process studies. Much more is required, however, to really enhance the reliability of the statistical model predictions for the very many reactions involved in the p-process, and especially those on unstable neutron-deficient targets. In particular, further progress has to be made in the predictions of a variety of other basic nuclear properties, like nuclear structure, level densities, nucleon-nucleus optical potentials or γ-ray strength functions.

It is hoped that this review will convince astrophysicsts, experimental or theoretical nuclear physicists and cosmochemists hunting for isotopic anomalies that the nuclear astrophysics ‘p-nuts’ are quite appealing after all, and can be enjoyed within a broad interdisciplinary research gathering.

Acknowledgements

We warmly thank D. Arnett and A. Baleisis for having provided unpublished results about their 2D models of the pre-SN O-rich layers referred to in Section 4.3, H. Utsunomiya and S. Harissopulos for sharing with us their knowledge of the experimental techniques of relevance to the p-process (Sections 3.1 and 3.2), and U. Ott for drawing our attention on some recent work on meteoritic isotopic anomalies related to the p-process. We are grateful to V. Demetriou, S. Harrissopulos, M. Rayet and M. Samyn for their help in the preparation of some figures, and to P. Mohr for his comments on Section 3.1. We are also indebted to the (anonymous) referee for his(her) very careful reading of the long manuscript, and for his(her) constructive comments. Finally, we address special thanks to our collaborators N. Prantzos and M. Rayet who have shared over many years our interest for the ‘nuclear astrophysics p-nuts’. This work has been supported in part by the Interuniversity Attraction Pole P5/07.

References

[1] E.M. Burbidge, G.R. Burbidge, W.A. Fowler, F. Hoyle, Rev. Mod. Phys. 29 (1957) 547.
[2] M. Arnould, K. Takahashi, Rep. Prog. Phys. 62 (1999) 395.
[3] B. Meyer, Annu. Rev. Astron. Astrophys. 32 (1994) 153.
[4] M. Busso, R. Gallino, G.J. Wasserburg, Annu. Rev. Astron. Astrophys. 37 (1999) 239.
[5] J. Audouze, Astron. Astrophys. 8 (1970) 436.

[6] K.L. Hainebach, D.N. Schramm, J.B. Blake, Astrophys. J. 205 (1976) 920.
[7] T.G. Harrison, Astrophys. J. Suppl. 36 (1978) 199.
[8] R.A. Chevalier, Science 276 (1997) 1374.
[9] K. Nomoto, K. Iwamoto, N. Kishimoto, Science 276 (1997) 1378.
[10] J. Audouze, J.W. Truran, Astrophys. J. 202 (1975) 204.
[11] M. Arnould, Ph.D. Thesis, Université Libre de Bruxelles, 1971 (unpublished).
[12] M. Arnould, Astron. Astrophys. 46 (1976) 117.
[13] E. Anders, N. Grevesse, Geochim. Cosmochim. Acta 53 (1989) 197.
[14] N. Grevesse, A. Noels, in: N. Prantzos, E. Vangioni-Flam, M. Cassé (Eds.), Origin and Evolution of the Elements, Cambridge University Press, Cambridge, 1993, p. 15.
[15] H. Palme, H. Beer, in: H.H. Vogt (Ed.), Landolt Börnstein, New Series, Group VI, Astronomy and Astrophysics, Subvolume 3a, Springer, Berlin, 1993, p. 196.
[16] S. Goriely, Astron. Astrophys. 342 (1999) 881.
[17] F. Käppeler, H. Beer, K. Wisshak, Rep. Prog. Phys. 52 (1989) 945.
[18] T. Lee, in: J.F. Kerridge, M.S. Matthews (Eds.), Meteorites and the Early Solar System, University of Arizona Press, Tucson, 1988, p. 1063.
[19] Q. Yin, S.B. Jacobsen, K. Yamashita, Nature 415 (2002) 881.
[20] N. Dauphas, B. Marty, L. Reisberg, Astrophys. J. 565 (2002) 640.
[21] T.J. Bernatowicz, E. Zinner (Eds.), Astrophysical Implications of the Laboratory Study of Presolar Materials, AIP Conference Proceedings, Vol. 402, AIP, New York, 1997.
[22] Q. Yin, E. Jagoutz, H. Wänke, Meteoritics 27 (1992) 310.
[23] W.M. Howard, B.S. Meyer, in: F. Käppeler, K. Wisshak (Eds.), Nuclei in the Cosmos II, IOP Pub., Bristol, 1993, p. 575.
[24] M. Rayet, M. Arnould, M. Hashimoto, N. Prantzos, K. Nomoto, Astron. Astrophys. 298 (1995) 517.
[25] M. Arnould, G. Paulus, G. Meynet, Astron. Astrophys. 321 (1997) 452.
[26] G. Audi, A.H. Wapstra, Private communication, 2001.
[27] S. Goriely, F. Tondeur, J.M. Pearson, At. Data Nucl. Data Tables 77 (2001) 311.
[28] Z.Y. Bao, H. Beer, F. Käppeler, et al., At. Data Nucl. Data Tables 76 (2000) 70.
[29] S.S. Dietrich, B.L. Berman, At. Data Nucl. Data Tables 38 (1988) 199.
[30] Photonuclear data for applications; cross sections and spectra 2000, IAEA-Tecdoc-1178.
[31] P. Mohr, Phys. Rev. C 61 (2000) 045802.
[32] J.P. Cox, R.T. Giuli, Principles of Stellar Structure, Gordon and Breach, New York, 1968.
[33] H. Utsunomyia, M.S. Smith, T. Kajino, in: M. Arnould, et al. (Eds.), Tours Symposium on Nuclear Physics IV, AIP Conference Proceedings, Vol. 561, AIP, New York, 2001, p. 159.
[34] H. Utsunomiya, H. Akimune, S. Goko, et al., in: K. Shibata (Ed.), Proceedings of Nuclear data for Science and Technology, J. Nucl. Sci. Technol. (Suppl. 2) 1 (2002) 542.
[35] H. Utsunomiya, H. Akimune, S. Goko, et al., Phys. Rev. C 67 (2003) 015807.
[36] H. Ohgaki, et al., IEEE Trans. Nucl. Sci. 38 (1991) 386.
[37] Gy. Gyurky, Zs. Fülöp, E. Somorjai, et al., Phys. Rev. C 2003, submitted (see also http://www.esf.org/pesc/workshops/02).
[38] S. Harissopulos, Private communication, 2002, (see http://www.esf.org/pesc/workshops/02).
[39] Gy. Gyürky, E. Somorjai, Zs. Fülöp, S. Harissopulos, P. Demetriou, T. Rauscher, Phys. Rev. C 64 (2001) 065803.
[40] S. Galanopoulos, P. Demetriou, M. Kokkoris, et al., Phys. Rev. C 67 (2002) 015801.
[41] C.E. Laird, D. Flynn, L.R. Hershberger, F. Gabbard, Phys. Rev. C 35 (1987) 1265.
[42] F.R. Chloupek, A. Murphy, R.N. Boyd, et al., Nucl. Phys. A 652 (1999) 391.
[43] S. Harissopulos, E. Skreti, P. Tsagari, et al., Phys. Rev. C 64 (2001) 055804.
[44] T. Sauter, F. Käppeler, Phys. Rev. C 55 (1997) 3127.
[45] J. Bork, H. Schatz, F. Käppeler, T. Rauscher, Phys. Rev. C 58 (1998) 524.
[46] N. Özkan, H. Schatz, F. Käppeler, T. Rauscher, Nucl. Phys. A 688 (2001) 459c.
[47] Zs. Fülöp, A.Z. Kiss, E. Somorjai, et al., Z. Phys. A 355 (1996) 203.
[48] W. Rapp, H.J. Brede, M. Heil, Nucl. Phys. A 688 (2001) 427c.
[49] N. Özkan, A.St.J. Murphy, R.N. Boyd, et al., Nucl. Phys. A 710 (2002) 469.

[50] E. Somorjai, Zs. Fülöp, A.Z. Kiss, et al., Astron. Astrophys. 333 (1998) 1112.
[51] P. Demetriou, C. Grama, S. Goriely, Nucl. Phys. A 707 (2002) 142.
[52] E.V. Verdick, J.M. Miller, Phys. Rev. 153 (1967) 1253.
[53] W. Hauser, H. Feshbach, Phys. Rev. 87 (1952) 366.
[54] J.A. Holmes, S.E. Woosley, W.A. Fowler, B.A. Zimmerman, At. Data Nucl. Data Tables 18 (1976) 306.
[55] J.W. Tepel, H.M. Hofmann, H.A. Weidenmüller, Phys. Lett. B 49 (1974) 1.
[56] H.M. Hofmann, T. Mertelmeier, M. Herman, J.W. Tepel, Z. Phys. A 297 (1980) 153.
[57] S. Goriely, in: M. Arnould, et al. (Eds.), Proceedings of Tours Symposium on Nuclear Physics III, AIP Conference Proceedings, Vol. 561, AIP, New York, 2001, p. 53.
[58] S. Goriely, in: K. Shibata (Ed.), Proceedings of Nuclear Data for Science and Technology, J. Nucl. Sci. Technol. (Suppl. 2) 1 (2002) 536.
[59] S. Schwarz, et al., Nucl. Phys. A 693 (2001) 533.
[60] Yu.N. Novikov, et al., Nucl. Phys. A 697 (2002) 92.
[61] G. Audi, A.H. Wapstra, Nucl. Phys. A 595 (1995) 409.
[62] C.F. von Weizsäcker, Z. Phys. 99 (1935) 431.
[63] P. Möller, J.R. Nix, W.D. Myers, W.J. Swiatecki, At. Data Nucl. Data Tables 59 (1995) 185.
[64] Y. Aboussir, J.M. Pearson, A.K. Dutta, F. Tondeur, At. Data Nucl. Data Tables 61 (1995) 127.
[65] S. Goriely, in: Proceedings of the 10th International Symposium on Capture Gamma-ray Spectroscopy and Related Topics, AIP Conference Proceedings, Vol. 529, AIP, New York, 2000, p. 287.
[66] M. Samyn, S. Goriely, P.-H. Heenen, J.M. Pearson, F. Tondeur, Nucl. Phys. A 700 (2002) 142.
[67] S. Goriely, M. Samyn, P.-H. Heenen, J.M. Pearson, F. Tondeur, Phys. Rev. C 66 (2002) 024326.
[68] Reference Input Parameter Library 2003, IAEA-Tecdoc, 2003, in press.
[69] H.A. Bethe, Phys. Rev. 50 (1936) 332.
[70] S. Goriely, Nucl. Phys. A 605 (1996) 28.
[71] P. Demetriou, S. Goriely, Nucl. Phys. A 695 (2001) 95.
[72] J.P. Jeukenne, A. Lejeune, C. Mahaux, Phys. Rev. C 16 (1977) 80.
[73] E. Bauge, J.P. Delaroche, M. Girod, Phys. Rev. C 63 (2001) 024607.
[74] S. Goriely, Nucl. Phys. A 718 (2003) 287c.
[75] A.J. Koning, J.P. Delaroche, Nucl. Phys. A 713 (2003) 231.
[76] L. Mc Fadden, G.R. Satchler, Nucl. Phys. A 84 (1966) 177.
[77] F.M. Mann, Hauser 5. A computer Code to calculate Nuclear Cross Sections, Hanford Engineering HEDL-TME 78-83, 1979.
[78] M. Nolte, et al., Phys. Rev. C 36 (1987) 1312.
[79] V. Avrigeanu, P.E. Hodgson, M. Avrigeanu, Phys. Rev. C 49 (1994) 2136.
[80] C. Grama, S. Goriely, in: N. Prantzos, S. Harissopulos (Eds.), Nuclei in the Cosmos, Editions Frontières, Gif-sur-Yvette, 1998, p. 463.
[81] G.E. Brown, M. Rho, Nucl. Phys. A 372 (1981) 397.
[82] C.M. McCullagh, M.L. Stelts, R.E. Chrien, Phys. Rev. C 23 (1981) 1394.
[83] J. Kopecky, M. Uhl, Phys. Rev. C 41 (1990) 1941.
[84] S. Goriely, Phys. Lett. B 436 (1998) 10.
[85] K. Govaert, et al., Phys. Rev. C 57 (1998) 2229.
[86] A. Zilges, S. Volz, M. Babilon, T. Hartmann, P. Mohr, K. Vogt, Phys. Lett. B 542 (2002) 43.
[87] W.D. Myers, W.J. Swiatecki, et al., Phys. Rev. C 15 (1977) 2032.
[88] S.G. Kadmenskii, V.P. Markushev, V.I. Furman, Sov. J. Nucl. Phys. 37 (1983) 165.
[89] S. Goriely, E. Khan, Nucl. Phys. A 706 (2002) 217.
[90] F. Catara, E.G. Lanza, M.A. Nagarajan, A. Vitturi, Nucl. Phys. A 624 (1997) 449.
[91] S. Goriely, in: N. Prantzos, S. Harissopulos (Eds.), Nuclei in the Cosmos, Editions Frontières, Gif-sur-Yvette, 1998, p. 314.
[92] A. Koning, H. Beijers, J. Benlliure, et al., in: K. Shibata (Ed.), Proceedings of Nuclear Data for Science and Technology, J. Nucl. Sci. Technol. (Suppl. 2) 2 (2002) 1161.
[93] M. Herman, R. Capote-Noy, P. Oblozinsky, A. Trkov, V. Zerkin, in: K. Shibata (Ed.), Proceedings of Nuclear Data for Science and Technology, J. Nucl. Sci. Technol. (Suppl. 2) 1 (2002) 116.

[94] T. Rauscher, F.-K. Thielemann, At. Data Nucl. Data Tables 79 (2001) 47.
[95] J.L. Zyskind, et al., Nucl. Phys. A 331 (1979) 180.
[96] L.W. Mitchell, et al., Nucl. Phys. A 443 (1985) 487.
[97] M.R. Anderson, Nucl. Phys. A 318 (1979) 471.
[98] M. Rios, et al., Astrophys. J. 199 (1975) 173.
[99] R.L. Hahn, Phys. Rev. 137 (1965) 1491.
[100] P. Mohr, T. Rauscher, H. Oberhummer, et al., Phys. Rev. C 55 (1997) 1523.
[101] P. Mohr, T. Rauscher, K. Sonnabend, K. Vogt, A. Zilges, Nucl. Phys. A 718 (2003) 243c.
[102] A. Jorissen, S. Goriely, Nucl. Phys. A 688 (2001) 508c.
[103] C. Angulo, M. Arnould, M. Rayet, et al., Nucl. Phys. A 656 (1999) 3.
[104] W.D. Arnett, Supernovae and Nucleosynthesis, Princeton University Press, Princeton, 1996.
[105] T. Weaver, S.E. Woosley, Phys. Rep. 227 (1993) 65.
[106] M. Hashimoto, Prog. Theor. Phys. 94 (1995) 663.
[107] H. Umeda, K. Nomoto, Astrophys. J. 565 (2002) 385.
[108] A. Heger, S.E. Woosley, Astrophys. J. 567 (2001) 532.
[109] S.E. Woosley, A. Heger, T.A. Weaver, Rev. Mod. Phys. 74 (2002) 1015.
[110] A. Maeder, G. Meynet, Annu. Rev. Astron. Astrophys. 38 (2000) 143.
[111] D. Arnett, G. Bazán, Science 276 (1997) 1359.
[112] G. Bazán, D. Arnett, Astrophys. J. 496 (1998) 316.
[113] C. Chiosi, A. Maeder, Annu. Rev. Astron. Astrophys. 24 (1986) 329.
[114] A.K. Dupree, Annu. Rev. Astron. Astrophys. 24 (1986) 377.
[115] H. Lamers, T. Nugis, J.S. Vink, A. de Koter, in: H. Lamers, A. Sapar (Eds.), ASP Conference Series, Vol. 204, ASP, San Francisco, 2000, p. 395.
[116] K. Nomoto, K. Maeda, H. Umeda, T. Ohkubo, J. Deng, P. Mazzali, in: K.A. van der Hucht, A. Herrero, C. Esteban (Eds.), A Massive Star Odyssey, from Main Sequence to Supernova, IAU Symp. 212, ASP, San Francisco, 2003, p. 395.
[117] M. Hashimoto, K. Nomoto, T. Shigeyama, Astron. Astrophys. 210 (1989) L5.
[118] K. Nomoto, M. Hashimoto, Phys. Rep. 163 (1988) 13.
[119] G.R. Caughlan, W.A. Fowler, At. Data Nucl. Data Tables 40 (1988) 283.
[120] H. Beer, F. Voß, R.R. Winters, Astrophys. J. Suppl. 80 (1992) 403.
[121] M. Rayet, M. Hashimoto, Astron. Astrophys. 354 (2000) 740.
[122] M. Rayet, M. Arnould, 1996, unpublished.
[123] W. Zhang, S.E. Woosley, A.I. MacFadyen, Astrophys. J. 586 (2003) 356.
[124] T. Rauscher, A. Heger, R.D. Hoffman, S.E. Woosley, Astrophys. J. 576 (2002) 323.
[125] S. Asida, W.D. Arnett, Astrophys. J. 545 (2000) 435.
[126] W.D. Arnett, Nucl. Phys. A 688 (2001) 177c.
[127] A. Baleisis, W.D. Arnett, Nucl. Phys. A 688 (2001) 185c.
[128] A. Burrows, T.A. Thompson, in: ESO/MPA/MPE Workshop, Garching, Germany, 2002, p. 53.
[129] S.E. Woosley, W.M. Howard, Astrophys. J. Suppl. 36 (1978) 285.
[130] G.R. Caughlan, W.A. Fowler, M.J. Harris, B.A. Zimmerman, At. Data Nucl. Data Tables 32 (1985) 197.
[131] R. Kunz, M. Fey, M. Jaeger, et al., Astrophys. J. 567 (2002) 643.
[132] M. Rayet, N. Prantzos, M. Arnould, Astron. Astrophys. 227 (1990) 271.
[133] N. Prantzos, M. Hashimoto, M. Rayet, M. Arnould, Astron. Astrophys. 238 (1990) 455.
[134] P. Kroupa, C.A. Tout, G. Gilmore, Mon. Not. R. Astron. Soc. 262 (1993) 545.
[135] T.A. Weaver, S.E. Woosley, Phys. Rev. 227 (1993) 65.
[136] S. Woosley, T. Weaver, Astrophys. J. Suppl. 101 (1995) 181.
[137] H. Schatz, A. Aprahamian, J. Görres, et al., Phys. Rep. 294 (1998) 167.
[138] M. Arnould, M. Rayet, M. Hashimoto, in: M. Arnould, et al. (Eds.), Tours Symposium on Nuclear Physics III, AIP Conference Proceedings, Vol. 425, AIP, New York, 1998, p. 626.
[139] V. Costa, M. Rayet, R.A. Zappalà, M. Arnould, Astron. Astrophys. 358 (2000) L67.
[140] P.A. Mazzali, N.N. Chugai, Astron. Astrophys. 303 (1995) 118.
[141] M. Jaeger, R. Kunz, A. Mayer, et al., Phys. Rev. Lett. 87 (2001) 202501.

[142] P.E. Koehler, Phys. Rev. C 66 (2002) 055805.
[143] S.E. Woosley, D.H. Hartmann, R.D. Hoffman, W.C. Haxton, Astrophys. J. 356 (1990) 272.
[145] S. Goriely, M. Arnould, I. Borzov, M. Rayet, Astron. Astrophys. 375 (2001) L35.
[146] J. Giles, Nature 411 (2001) 877.
[147] G.M. Fuller, B.S. Meyer, Astrophys. J. 453 (1995) 792.
[148] D. Belic, C. Arlandini, J. Besserer, et al., Phys. Rev. Lett. 83 (1999) 5242.
[149] D. Belic, C. Arlandini, J. Besserer, et al., Phys. Rev. C 65 (2002) 035801.
[150] K. Wisshak, F. Voss, C. Arlandi, et al., Phys. Rev. Lett. 87 (2001) 251102.
[151] J.-P. Arcoragi, N. Langer, M. Arnould, Astron. Astrophys. 249 (1991) 134.
[152] R. Gallino, C. Arlandini, M. Busso, Astrophys. J. 497 (1998) 388.
[153] S. Goriely, N. Mowlavi, Astron. Astrophys. 362 (2000) 599.
[154] M.F. El Eid, N. Langer, Astron. Astrophys. 167 (1986) 274.
[155] S.E. Woosley, in: B. Hauck, A. Maeder, G. Meynet (Eds.), Nucleosynthesis and Chemical Evolution, 16th Advance Course Saas-Fee, Geneva Observatory, 1986, p. 1.
[156] W. Glatzel, M.F. El Eid, K.J. Fricke, Astron. Astrophys. 149 (1985) 413.
[157] M. Rayet, N. Prantzos, M. Arnould, in: G.J. Mathews (Ed.), Origin and Distribution of the Elements, World Scientific, Singapore, 1988, p. 625.
[158] M. Rayet, M. El Eid, M. Arnould, in: F. Käppeler, K. Wisshak (Eds.), Nuclei in the Cosmos, Institute of Physics Publishing, Bristol, 1993, p. 613.
[159] E.J. Lentz, E. Baron, P.H. Hauschildt, D. Branch, Astrophys. J. 580 (2002) 374.
[160] W. Hillebrandt, J.C. Niemeyer, Annu. Rev. Astron. Astrophys. 38 (2000) 191.
[161] M. Reinecke, W. Hillebrandt, J.C. Niemeyer, Astron. Astrophys. 391 (2002) 1167.
[162] B. Leibundgut, Annu. Rev. Astron. Astrophys. 39 (2001) 67.
[163] K. Nomoto, F.-K. Thielemann, K. Yokoi, Astrophys. J. 286 (1984) 644.
[164] A.M. Khokhlov, Astron. Astrophys. 245 (1991) 114.
[165] W.M. Howard, B.S. Meyer, S.E. Woosley, Astrophys. J. 373 (1991) L5.
[166] A. Maeder, P.S. Conti, Annu. Rev. Astron. Astrophys. 32 (1994) 227.
[167] S.E. Woosley, N. Langer, T.A. Weaver, Astrophys. J. 411 (1993) 823.
[168] E.P.J. van den Heuvel, in: H. Nussbaumer, A. Orr (Eds.), Interacting Binaries, 22nd Saas-Fee Course, Springer, Berlin, 1994, p. 263.
[169] S.E. Woosley, N. Langer, T.A. Weaver, Astrophys. J. 448 (1995) 315.
[170] S. Cassisi, I. Iben Jr., A. Tornambè, Astrophys. J. 496 (1998) 376.
[171] I. Iben Jr., A.V. Tutukov, Astrophys. J. 370 (1991) 615.
[172] M. Limongi, A. Tornambè, Astrophys. J. 371 (1991) 317.
[173] S.E. Woosley, T.A. Weaver, Astrophys. J. 423 (1994) 371.
[174] S.E. Woosley, R.E. Taam, T.A. Weaver, Astrophys. J. 301 (1986) 601.
[175] S. Goriely, J. José, M. Hernanz, M. Rayet, M. Arnould, Astron. Astrophys. 383 (2002) L27.
[176] M. Hashimoto, K. Nomoto, K. Arai, K. Kaminishi, Astrophys. J. 307 (1986) 687.
[177] L. Piersanti, S. Cassisi, A. Tornambè, Astrophys. J. 558 (2001) 916.
[178] R.K. Wallace, S.E. Woosley, Astrophys. J. Suppl. 45 (1981) 389.
[179] G.R. Huss, R.S. Lewis, Geochim. Cosmochim. Acta 59 (1995) 115.
[180] R.O. Pepin, R.H. Becker, P.E. Rider, Geochim. Cosmochim. Acta 59 (1995) 4997.
[181] A.P. Koscheev, M.D. Gromov, R.K. Mohapatra, U. Ott, Nature 412 (2001) 615.
[182] D. Heymann, M. Dziczkaniec, Meteoritics 15 (1980) 15.
[183] U. Ott, Astrophys. J. 463 (1996) 344.
[184] C.L. Harper Jr., Astrophys. J. 466 (1996) 437.
[185] M. Schönbächler, M. Rehkämper, A.N. Halliday, et al., Science 295 (2002) 1705.
[186] C. Münker, S. Weyer, K. Mezger, et al., Science 289 (2000) 1538.
[187] C. Sanloup, J. Blichert-Toft, P. Télouk, et al., Earth Planet. Sci. Lett. 184 (2000) 75.
[188] J. Audouze, D.N. Schramm, Nature 237 (1972) 447.
[189] A. Prinzhofer, D.A. Papanastassiou, G.J. Wasserburg, Astrophys. J. 344 (1989) L8.
[190] A. Prinzhofer, D.A. Papanastassiou, G.J. Wasserburg, Geochim. Cosmochim. Acta 56 (1992) 797.

[191] G.W. Lugmair, S.J.G. Galer, Geochim. Cosmochim. Acta 56 (1992) 1673.
[192] L.E. Nyquist, B. Bansal, H. Wiesmann, C.-Y. Shih, Meteoritics 29 (1994) 872.
[193] S.E. Woosley, W.M. Howard, Astrophys. J. 354 (1990) L21.
[194] M. Rayet, M. Arnould, in: Th. Delbar (Ed.), Radioactive Nuclear Beams 1991, Adam Hilger, Bristol, 1992, p. 347.
[195] T. Rauscher, F.-K. Thielemann, H. Oberhummer, Astrophys. J. 451 (1995) L37.
[196] H. Schatz, A. Aprahamian, J. Görres, et al., Phys. Rep. 294 (1998) 167.
[197] H. Schatz, A. Aprahamian, V. Barnard, et al., Phys. Rev. Lett. 86 (2001) 3471.
[198] S. Fujimoto, M. Hashimoto, O. Koike, K. Arai, R. Matsuba, Astrophys. J. 585 (2003) 418.